PHD

Design, Build & Test of an HTS Machine A.C. Loss Measurement Platform: Aircraft Applications

Patel, Jay

Award date:
2019

Awarding institution:
University of Bath

Design, Build & Test of an HTS Machine A.C. Loss Measurement Platform: Aircraft Applications

Author:
Mr. Jay Patel

A thesis submitted in fulfilment for the degree of Doctor of Philosophy at the University of Bath

UNIVERSITY OF BATH

Department of Electrical and Electronic Engineering
Applied Superconductivity Group

April 18, 2019

Copyright

Abstract

Superconductors are entering into an exciting period since their discovery in the early 1900s. Electrification is becoming more economically feasible in all modes of applications where harmful gas emitting technologies are used. While it is true that superconductors at their current technology level are unlikely to rival copper based technologies for low and high power applications, in environments where specific weights and power density are a priority they have already been proven to be more efficient and cost effective. Furthermore, since the late 1900s when superconducting machine projects were launched, much progress has been made towards making the technology technically and economically feasible.

The work contained in this thesis focusses on pushing superconductors towards scalable commercialisation by focussing on a crucial limiting factor, namely A.C. losses. In an A.C. operating environment, superconductors produce heat which must be dissipated to maintain superconductivity. On the other hand, virtually zero loss is measured in the D.C. operation. In rotating electrical machines the A.C. environment is unavoidable and we must understand and mitigate this characteristic to lower the cryogenic system cost, improve efficiency and realise the ambition of many in the research field to see widespread adoption of superconductors in transportation.

To this end, the following items of original, new work in this thesis include:

1. Design, build and test of a novel A.C. loss measurement platform integrating a motor environment.
2. Measurement of the A.C. losses produced within a live operating machine.
3. Characterisation of cutting edge A.C. loss reduction techniques using the newly developed measurement rig.
4. Development of a baseline target performance required from superconducting technology for electrical aircraft propulsion feasibility.

Acknowledgements

When I began this Ph.D as a confused, lost but aspiring engineer I was not confident in my ability to complete the program. My supervisors gave me support and put their confidence in me to autonomously deliver a costly program of research and provided a budget that is rare for Ph.D students. I have gained a lot of unique experiences during this project and I am grateful for the opportunity.

Secondly, I have made many great friends during the course of this program and often we have had to rescue our lost ships of research together! There are too many people who have helped to list but a few important contributories to the publishing of this thesis include Dr. Zhenyu Zhang, Dr. Fei Liang, Mr. Hamoud Alafnan & Mr. Sriharsha Venuturumilli. I am hugely indebted to Mr. Michael Linham whose practical knowledge of engineering saved me more times than I care to remember. I must mention Dr. Fred Eastham's generosity to help me develop this project and the many hours he spent on guiding solutions to the research problem and forcing me to think beyond my capabilities.

Finally, my greatest thanks goes to my family; in particular my mother. During my doctorate she was diagnosed with terminal cancer having fought it twice earlier. Putting her own needs aside she pushed me towards completing my studies and remained strong for me to be able to focus on my work.

ભણજે

-Baa

Contents

Nomenclature

α	Pole pitch in radians
ϵ_a	Emissivity of surface a
ϵ_b	Emissivity of surface b
η_p	Propulsive efficiency
Λ	Sweep angle
$\mathfrak{F}$	MMF
μ	Permeability of medium
μ_{rrec}	Magnetic recoil line
Ω	Shaft speed in rad/s
ϕ	Magnetic flux
$\Re$	Magnetic reluctance
ρ	Resistivity
τ	Shear strength
$\tau(r)$	Pole pitch
A	Surface area
a_n, b_n	Fourier coefficients
B	Magnetic Flux Density
B_g	Air-gap Flux Density

B_r	Remnant Flux Density
B_{mg}	Peak magnetic field density
C_D	Drag coefficient
C_k	Calibration Constant
C_L	Lift coefficient
C_p	Specific heat capacity
c_p	Specific fuel consumption
D	Drag
d_s	Filament diameter
d_w	Wire diameter
E	Young's modulus
e	Electron charge mass
e_o	Oswald efficiency
f	Frequency
F_l	Lorentz Force
g	Air gap
H	Magnetic Field
h_M	Magnet Height
I_m	Second moment of area
k_d	Distribution Factor
k_E	Speed constant
k_p	Pitch Factor
k_T	Torque constant
L	Lift

L_t	Twist pitch of filaments
M_{ff}	Mission fuel fraction
N_{ph}	Number of turns per stator phase
r	Radius
r_{in}	Inner Radii
r_{out}	Outer Radii
S_d	Distance travelled
T_a	Temperature of surface a
v	Velocity
v_{ltr}	Loiter speed
W_f	Fuel weight
W_x	Weight of component x
W_{TO}	Take-off weight
2G	2nd generation
AFPM	Axial flux permanent magnet
AR	Aspect ratio
B	Magnetic Flux Density
CC	Coated conductor
COP	Coefficient of performance
DAQ	Compact data acquisition
DPC	Double pancake coil
F	Flowrate
GT	Gas turbine
h	Heat transfer coefficient

HTS	High Temperature Superconductors
I	RMS Current
I_c	Critical current
J	Current Density
LTS	Low Temperature Superconductors
m	Number of phases
MMF	Magnetomotive Force
MTOW	Maximum takeoff weight
NbTi	Niobium Titanium
NdFeB	Neodymium boron iron
OCV	Open circuit voltage
OEI	One engine inoperative
p	Machine Pole Pair Number
PPR	Price performance ratio
q	Heat load
R	Resistance
SLPM	Standard Liters Per Minute
THD	Total harmonic distortion
TRL	Technology Readiness Level
TSFC	Thrust specific fuel consumption
V	Voltage

Chapter 1

Introduction

Cars, trains, ships, trucks and aeroplanes are by a large margin powered using derivatives of crude oil. People have begun to realise, and care about, the harmful effects these modes of transport pose for our health. Large scale international action has begun on the transformation of these "dirty" means of travelling to clean electrical systems; the author sees this as a huge opportunity for superconductivity to capitalise.

Copper, an abundant and cheap element, has become prevalent in electrical engineering applications as a medium to conduct electricity and has been largely unchallenged since the time of its discovery. The monopoly of copper continues to be disrupted ever since Dr. Onnes made a small point in his laboratory the coldest place on earth in 1911 and discovered the abrupt vanishing of resistance in mercury at 4K. The discovery triggered huge global research into the counter-intuitive phenomenon in terms of characterisation, quantum understanding and applications of these fascinating materials.

Thus, in this chapter a brief introduction to superconductivity is given from an engineer's perspective, avoiding quantum physics related mathematical and theoretical complexities; instead the opening chapter focusses on macroscopic characteristics that are important in commercialisation of the technology and presents a brief qualitative explanation of the important underlying physics including the following:

1. Evolution of superconductors from LTS to HTS and types
2. A.C. loss significance and measurement techniques
3. Progress of superconducting machine technology and a review of historical demonstrators

4. A look towards the future and vision the superconductivity community have for machine applications

Finally, context of the thesis research is given and its importance in furthering the field is explained.

1.1 Background

Since 1911 the discoveries of materials exhibiting superconductivity have been numerous with a promising upwards trend in the critical temperature, from mercury at 4K in 1911 to hydrogen sulphide at 203K in 2015. Generally, LTS refer to materials that demonstrate superconductivity below 20 or 30K although "high temperature" in this research field is now generally considered to be 77K or above i.e. the boiling point of liquid nitrogen. Initially thought to be only a "perfect" conductor, it was later found that "perfect" diamagnetism is a key feature of superconductivity that cannot be fully explained with existing theories. Superconductors are only superconducting when operated within the bounds of their temperature, magnetic field and current limits.

Of the two types of superconductors, creatively named type-I, and type-II, the latter are most relevant to the research in this thesis due to their higher critical magnetic field, which is essential within machine applications. Type-I superconductors have a critical field of less than 0.1T and do not find any power engineering applications. Historically type-II, hard LTS have found the most commercial application within MRI scanners and electromagnets because of their cheap, malleable and easy to form manufacturing process along with their unique ability to create fields above 30T where copper cannot be used. In arenas where copper based power systems can compete, the uptake in superconductivity has been slow i.e. power grid devices, electrical rotating machines and energy storage. Whilst safety, costs and low TRL feed into the reason for low adoption, a key issue is the cooling power required to maintain superconductivity.

As opposed to a virtually zero resistance in D.C. operation, superconductors exhibit inefficiencies with the A.C. regime. Whilst the economics of what will make superconductors feasible are complicated, essentially lifecyle costs of using them should be less than copper alternatives and/or the added revenue should overcome the increase in costs. Two sources of significant contribution towards the intial capital cost of any HTS system are the material itself and the associated refrigeration costs. A PPR of

\$50/kA·m is needed to rival copper and since 2000 considerable progress has been made towards this [89]. Whilst it is true the A.C. losses produced by superconductors are much lower than copper losses in a like for like comparison, the heat from a superconductor must be removed from a low temperature environment and generally requires several times the cooling power as input to remove the heat energy [75]. Indeed the ideal Carnot cycle still only allows a maximum 35.6% COP when removing heat from a 77K environment to room temperature. The challenge is further exacerbated as current 2G HTS technology are designed for commercial application at temperatures of less than 77K where the COP is worse and the cost of cryogens are higher i.e. liquid nitrogen can be purchased for pence per litre whilst liquid helium costs pounds per litre. The lower operating temperature boosts the critical current by an amount known as the "lift factor". Therefore, being able to understand, measure and reduce the A.C. loss characteristic is one important strand in the research field tapestry and is the focus of this thesis.

1.2 Type-II Superconductivity

Understanding type-II superconductivity serves as a good platform to understand the cause of A.C. losses and their significance in power engineering applications. Superconductors are only "super" within a small operating region bound by constraints on their external field, operating temperature and current. Type-I superconductors may exhibit some A.C. loss but due to their low critical field and near perfect diamagnetic property it has not been focussed on within past research [116]. Type-II superconductors on the other hand have a mixed state, exhibiting diamagnetism below a lower critical field but allowing flux to penetrate in packets above this field and below a second upper critical field, which can be as high as 100T for rare-earth based superconductors [61]. Whilst the penetration of flux into the superconductor is what enables it to sustain a high critical current, the external magnetic field is a double edged sword since it is also gives rise to A.C. loss.

Figure 1.1 shows the different response between type I and II superconductors to a magnetic field. Without considering the demagnetisation factor due to geometry variations between samples the type-I superconductor allows flux to penetrate widely through the material where as in a type-II superconductor the flux is quantised into discrete packets and penetrate through the material within a confined coherence length usually denoted

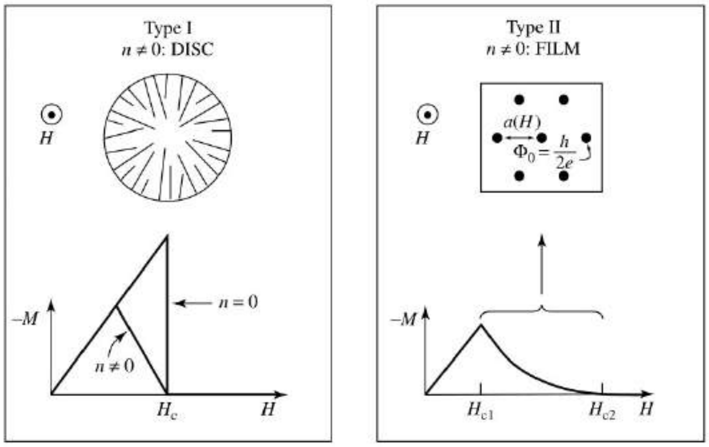

Figure 1.1: Flux penetration differences between Type-I and II superconductors. Left picture shows Type-I flux meandering through the superconductor in laminar planes whilst patterned, quantised flux penetrate Type-II on the right. [31]. Reproduced under Section 29(1) of the Copyright, Designs and Patents Act 1988.

ξ and of quantity equal to $\frac{h}{2e}$, where h is Planck's constant [25]. The ratio between λ, the London penetration depth, and ξ determine the type of the superconductor, a low ratio indicates better diamagnetism and more suceptibility to flux flow i.e. a type-I superconductor while the opposite is true for a type-II. The fluxoids are naturally hexagonally packed across the superconductor at equilibrium due to repulsion forces between them. Outside the characteristic length the material remains superconducting and will allow a transport current to pass [79]. Flux pinning caused by defects in the lattice like material force the flux to remain stationary, which ultimately permits a higher transport current within a magnetic field. As the transport current passes between the fluxoids the Lorentz force, $F_l = J \times B$ acts to unpin them, eventually; when F_l becomes more than the pinning force the movement of fluxoids generates an opposing electric field, $E = v \times B$, and associated heating which determines the critical transport current. The "hardness" of a superconductor therefore refers to the amount of pinning force available and thus its ability to sustain a high transport current. The mode of A.C. loss described here is only one aspect, known as the transport A.C. loss. Further modes exists and are explained in the next section.

1.3 A.C. Loss

In the D.C. operation the superconductor will carry up to its critical current until either the critical magnetic field or temperature are breached with virtually zero loss. The same is not true when the applied field or transport current is alternating. A.C. operation causes significant loss issues for superconductors, principally through hysteresis (1), which is a direct result of superconductivity but also other common losses such as eddy currents (2), joule heating (2,3) and magnetisation losses (4) in the metal stabilisers layered with the YBCO which help improve its mechanical and electrical stability as shown in figure 1.2. The hysteresis loss within the superconducting material itself can be calculated the same as any other ferromagnetic material i.e. by integrating along its $B - H$ curve. The magnetisation is a result of vortices and flux pinning which are set-up during a positive cycle but must be overcome by work via the applied magnetic field and presents itself as heat generation within the material.

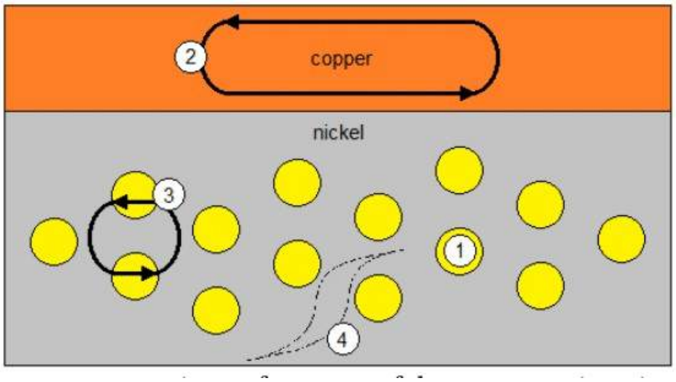

Figure 1.2: Mechanisms of A.C. losses arise from superconductivity related physics and normal ohmic losses. Reproduced under Section 29(1) of the Copyright, Designs and Patents Act 1988 [88]

Comparing like for like, the losses produced by copper assuming a $2\,{}^{A}/_{mm^{2}}$ current density would be approximately $15\,{}^{mW}/_{Am}$, when taking the cooling penalties into account a superconducting equivalent would need a loss of $1\,{}^{mW}/_{Am}$. Current applications produce a few multiples over this benchmark [75].

1.3.1 Bean Model

In 1962 Bean proprosed a model which went on to become famous in the field of superconductivity and proved fairly accurate for simple cases of a superconductor in an externally applied field [12]. The model proposed several variables that the A.C. losses are dependant on which furthered ideas on how to lower them but also provided useful relationships to be wary of in their applications. The bean model assumes either a zero current level or full J_c depending on whether a sector of the superconductor has experienced the external field or not. Figure 1.3 displays how the bean model creates a magnetisation curve using these assumptions. For a given magnitude of external field the flux penetrates a characteristic distance into the superconductor, for this depth full J_c is assumed whilst the remaining areas remain in a virgin state. A penetration depth is estimated using Ampere's law for one dimension and is used to find the full penetration field as $H \geq {}^{\pi J_c D}/_{5} = H^*$.

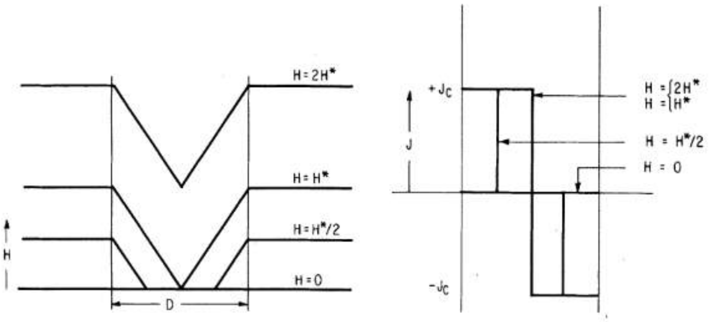

Figure 1.3: Bean model current distribution for given applied magnetic field assumption. A magnetisation loop is derived which can be used to estimate the magnetisation loss. Reproduced under Section 29(1) of the Copyright, Designs and Patents Act 1988 [12]

A magnetisation loop is calculated according to the calculation of B from H as shown in equation 1.1 and 1.2.

$$B = \frac{\int H dv}{\int dv} \tag{1.1}$$

$$4\pi M = B - H \tag{1.2}$$

where, for fields lower than the penetration field according to the geometry shown in figure 1.3, the relationship would be as shown in equation 1.3.

$$B = \frac{H^2}{H^*} \tag{1.3}$$

Several models have evolved over time from the Bean critical state model to the Norris model [12] [74] & to several variations of these; more modern advances towards refined FEA modelling of superconductors also exist but are focussed on fast 2D geometries [82]. The following is a brief list of some of the most important revelations to have come from these models:

1. Perpendicular magnetic fields increase A.C. losses more than any other field orientation.
2. The loss varies according to a square law to the superconducting filament width.
3. The loss varies according to a power law to the transport current.
4. The loss is generally independent of frequency as it is hysteretic in nature.
5. Flux flow losses dominate in transport current losses as opposed to the self field.
6. Aside from other economical factors such as the unique ability to provide power dense performance, the A.C. loss is too great to be competitive with copper within appreciable frequency ranges and operating temperatures.

1.3.2 *H*-Formulation

Along with analytical models several computer simulation models have been formulated to model more complicated geometries and simulate several modes of loss. The most established and commonly used technique is the *H*-Formulation shown below, it seeks to primarily solve for the magnetic field subject to the boundary conditions and derive the current and voltage characteristics [122]. The $E - J$ power law, shown by equation 1.4, defines observed experimental results and along with Faraday and Ampere's law, shown in equations 1.5 and 1.4, combine to find equation 1.6. Equation 1.6 can be solved using FEM software such as Comsol. Many codes are freely available online for this purpose. The H-Formulation simulation method is used to prove the results and conclusions of this thesis and thus verify and validate the work presented.

$$E_z = E_0 \left(\frac{J}{J_c} \right)^n \tag{1.4}$$

$$J_z = \frac{\partial H_y}{\partial x} - \frac{\partial H_x}{\partial y} \tag{1.5}$$

$$\begin{bmatrix} \frac{\partial E_z}{\partial y} \\ \frac{\partial E_z}{\partial x} \end{bmatrix} = -\mu_0 \mu_r \begin{bmatrix} \frac{\partial H_x}{\partial t} \\ \frac{\partial H_y}{\partial t} \end{bmatrix} \tag{1.6}$$

where H is the magnetic field, μ is the permeability of the medium and ρ is the material resistivity.

A predominant issue for H-formulation is the extermely non-linear behaviour of the equations due to the $E - J$ power law which often causes large computation times for anything more than simple 2D axi-symmetric coil simulations.

1.3.3 Measurement Techniques

Many techniques have been developed and continue to be developed to measure the A.C. losses of superconductors. The importance of measuring A.C. loss relies on being able to test the outputs of theoretical models to lower the cooling costs. Some techniques to lower the loss resulting from simulation include the use of flux diverters, striation, transposed geometries and wire twisting [4]. As the topic of this thesis is the development of an A.C. loss measurement platform integrated inside a machine, a brief introduction to each major measurement technique is given to better understand the design process presented later.

Electrical Method

The electric method is a common, fast and sensitive A.C. loss measurement platform. It is simple to measure the transport current loss using the circuit schematic shown in figure 1.4. The transport current loss is dominated by the flux flow loss mentioned in section 1.2 and is measured by cancelling the inductive component of voltage until the purely resistive part, the A.C. loss, is measured. The electric method is simple in cases where the electromagnetic environment is known and stable but requires further steps to measure the loss in the case of synchronised applied external fields and even more calibration steps for out of phase magnetic fields [7]. Pick-up coils are used to measure the magnetisation loss separately and are normally calibrated with a known electromagnetic sample such as a copper strip to identify the magnetisation of the superconducting sample. The measurement becomes more difficult for larger coils due to the increased risk of noise. The set up shown below was used to estimate the A.C. transport losses and aid in the design process described in chapter 2.

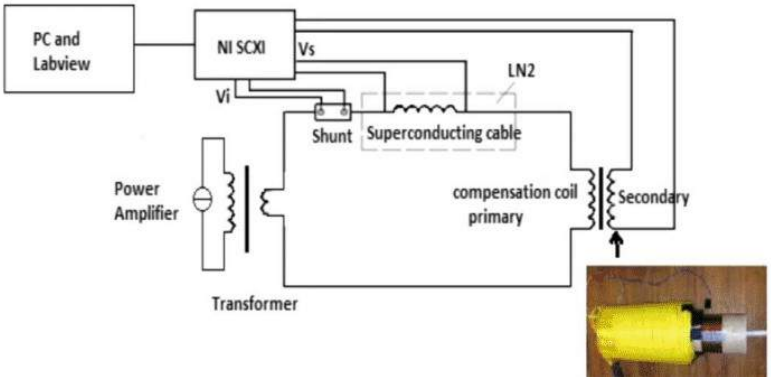

Figure 1.4: Schematic of the electrical method to measure A.C. losses [127]. Reproduced under Section 29(1) of the Copyright, Designs and Patents Act 1988.

The transport current loss is measured using an NI DAQ setup for the in-phase voltages while the power is modulated with an amplifier before being pass to a step down transformer. The inductive voltage is cancelled by the use of a compensation coil which is wound with many turns of fine copper wire. A shunt is used to measure the line current.

Calorimetric Method

The heat dissipation that occurs during the A.C. loss process gives rise to a temperature gradient along the superconducting sample and subsequently the cryogen used to carry the heat away. Measuring either the disturbance in the cryogen or the temperature of the superconductor, the total supplied power being turned into heat can be estimated. Whilst these methods are free from sensitivity issues due to the electromagnetic environment and can be used to measure the total losses in complicated, time varying and phase shifted magnetic fields, they do suffer from a lower sensitivity. Usually these set ups are well suited for larger samples as the increased loss makes the measurement more accurate. Common errors associated with the measurement technique include zero offset, drift, minimum resolution and noise.

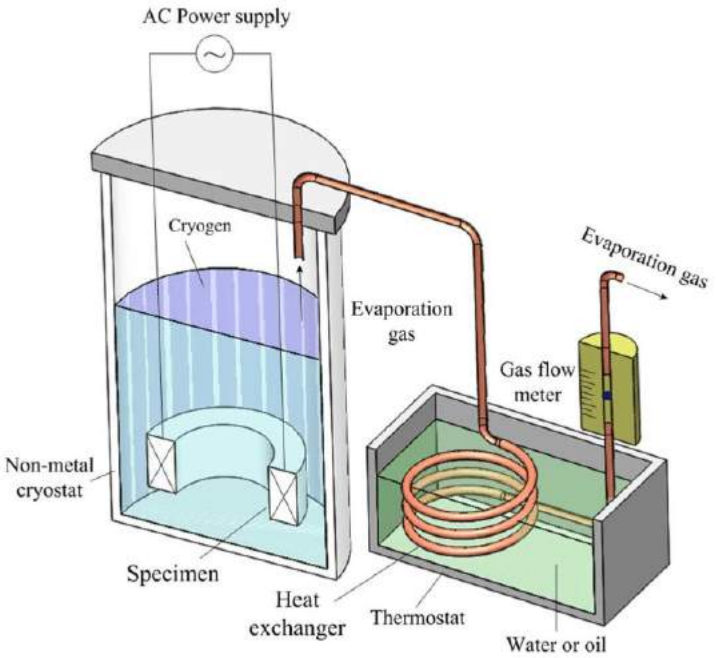

Figure 1.5: Schematic of the calorimetric method to measure A.C. losses. Reproduced under Section 29(1) of the Copyright, Designs and Patents Act 1988 [113]

Figure 1.5 details the essential elements of every calorimetric system. A superconducting sample is placed inside an adiabatic container with any heat source such as field generators placed outside such that the cryogen boil off is due to the background flow and superconductor only. The chamber must be of non-metallic construction to avoid eddy currents affecting the measurements. The evaporated gas is piped away towards a mass flow meter calibrated for the specific cryogen. Normally the mass flow meters are calibrated for gas at room temperature. Therefore, the piping passes through a heat exchanger before entering the flow meter. The latent heat of vaporisation of liquid nitrogen is approximately 199 kJ/kg [27], which translates to an evaporation of 0.000378 litres of liquid nitrogen per minute for every Watt of power. The gas equivalent becomes 0.257 litres per minute per Watt of power. Thus the A.C. loss can be calculated according to equation 1.7.

$$Q_{ac} = \frac{F \times C_k}{f} \tag{1.7}$$

where F is the flowrate, C_k is the calibration constant and f is the electrical frequency.

1.4 Superconducting Machines

Mostly, the focus of research has been on partially superconducting machines as the A.C. loss within fully superconducting machines, particularly the stator, are considered too problematic at the moment [28]. The benefit of a field winding is an enhanced magnetic loading, compact size and lower losses due to an A.C. magnetisation ripple field. Although these are gained at the expense of a more complicated cooling mechanism as the rotor is dynamic whilst the cooling components remain static. The first machines appeared in the late 1900s with development prompted by military applications and demonstrated several issues with the technology including reliability, manufacturing issues, cost and lack of adequate superconductor supply. This section will demonstrate the most important machine demonstrations to have been produced over the past 30 years and identifies the niche that remains to be explored and is thus the focus of study in this thesis.

1.4.1 Historical Machine Demonstrations

Before beginning the design of an A.C. loss measurement platform integrated into a machine it was important to thoroughly grasp the previous work in this particular field. A comprehensive list of high impact and breakthrough machines were compiled and the author approximates up to 300 superconducting machines have been built and tested. Some of the most important demonstrations from these are listed below in table 1.1, it can be seen that with time, the focus has changes towards ceramic HTS for their simpler and more cost effective cooling compared to LTS based machines, which presented more significant sealing issues. Some NbTi machines took more than 60 hours to cool down and warm up as opposed to a few hours with HTS machines [117]. Additionally, the air gap for LTS machines were made larger to accommodate for the need of a vacuum to minimise internal heat transfer, thereby reducing the performance.

Table 1.1: List of notable past superconducting machine demonstrations

Machine Description	**Test Year**	**HTS Material**	**Operating Temp**	**Power Rating**
Fully S.C. [106]	1991	<25K	NbTi	18kVA
Fully S.C. [110]	1993	<10K	NbTi	30kVA
HTS Rotor, D.C. [112]	1995	<28K	BSCCO	125kW
Synchronous LTS Rotor [95],	1995	<10K	NbTi	10MVA
LTS Rotor, 4T Field Winding [117]	1997	<10K	NbTi	70MW
Synchronous PM Rotor, LTS Stator. [107],	1999	<10K	NbTi	150kW
Reluctance Machine, Bulk YBCO [58],	2000	<65K	YBCO	18.5kW
HTS Racetrack Rotor, Air cooled stator [72],	2002	30K	Bi-2223	380kW
Air-core, Synchronous HTS Field winding [119],	2002	<30K	BSCCO	1000HP
Induction Motor, HTS at End Ring and Bars [93],	2003	77K	BSCCO	1.2kW

Continued on next page

Table 1.1 – continued from previous page

Machine Description	**Test Year**	**Conducting Material**	**Operating Temp**	**Power Rating**
Superconducting field Coil Synchronous Motor [96],	2004	<77K	Bi 2223	100HP
Bulk Rotor, Reluctance Motor [77],	2004	<77K	YBCO	200kW
Bulk Rotor, Axial Flux Motor [69],	2002	<30K	GdBaCuO	60kW
Ship propulsion motor [35],	2007	<30K	BSCCO	36.5MW
Novel bulk rotor [71],	2007	<10K	NbTi & YBCO	1000HP
Axial Flux, PM Stator Motor [98],	2007	77K	YBCO	400kW
LH Circulation Induction Pump [70],	2011	<20K	MgB2	7.5kW
Series-wound DC Field SC, Automobile Drive [69],	2012	77K	Type H	30kW
DC Homopolar, HTS Rotor [62],	2013	77K	MgB2	5kW
DC Homopolar with liquid metal joints [33],	2016	<30K	BSCCO	200kW

Continued on next page

Table 1.1 – continued from previous page

Machine Description	Test Year	Conducting Material	Operating Temp	Power Rating
HTS Rotor with flux pump [22],	2016	77K	YBCO	10kW

It is evident from literature that the main focus has been on partially superconducting machines especially as the field windings due to their preferred operating environment in terms of A.C. losses. Machines making use of superconducting bulks have been demonstrated but currently suffer from demagnetisation issues as well as the requirement for magnetisation coils. A few axial flux machines have been demonstrated but have not been focussed on despite their high torque density, particularly suitable for low speed or wheel hub propulsion. Some niche aspects covered in the literature include the investigation of contact-less current terminals to remove heat load and advanced contact less bearings.

A niche gap that exists within the research field is the development of an axial flux motor integrating an A.C. loss measurement platform that can be used to quickly performance test emerging superconducting technologies. Normally, the windings have been manufactured as a one off use and fixed operation. No such machine exists from the extensive literature review and would provide a new research output concerning A.C. losses inside machines, which are a limiting factor [97] [68].

1.5 Roadmap of Superconductivity

It is fitting to mention the future roadmap of superconducting technologies to conclude the literature review and provide context to demonstrate the importance of the work presented in this thesis to the research field.

NASA and EADS have launched several prototype designs of future aircraft including Voltair, X-3 and the subsequent SUGAR proposal by Boeing to hybridise aircraft. While all-electric aircraft have been gaining traction particularly for short-haul flights, energy storage technologies have not reached the level needed to allow commercial long haul flights. It is expected that battery technology alone will not be able to solve this challenge as maximum theoretical limits of specific energies while close to kerosene are unlikely to be practical in the long term. Thus a hybrid solution for long haul aviation looks the most likely in the current landscape.

Within hybridised aircraft it has been widely accepted by NASA, Boeing and many other industry stakeholders that superconducting motors are a key enabler for propulsion as shown in figure 1.6. The power densities of 40+ kW/KG required are not anticipated to be provided by incremental improvements in topology or materials for copper based drives and cryogenics may be essential. Carbon nano-tubes are seen as a high risk, high investment alternative but still have current densities a fraction of that offered by superconductivity. Recently Siemens built a prototype halbach array PM motor that achieved 5kW/KG by optimising and pushing every component to its limit and is considered state of the art for conventional power density [16].

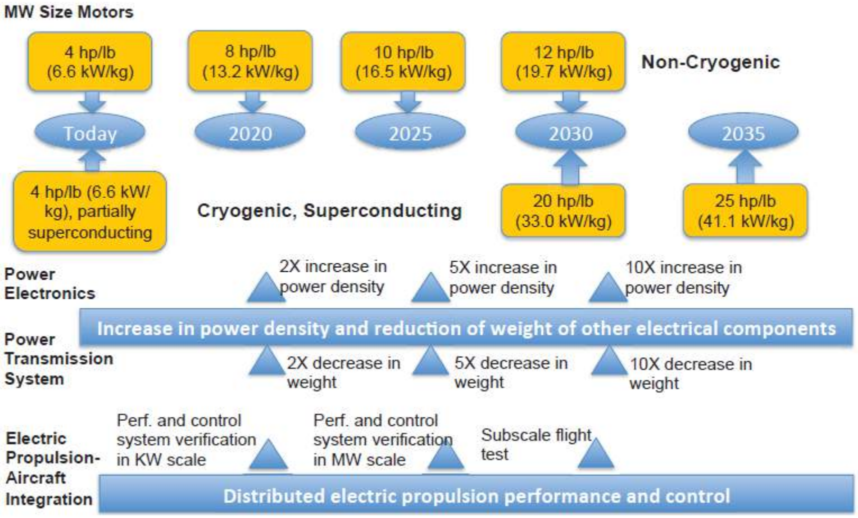

Figure 1.6: Superconducting motors have been identified as a enabler of commercial aviation in several NASA studies [67] [26]. Reproduced under Section 29(1) of the Copyright, Designs and Patents Act 1988.

Within superconductivity, several challenges need to be negotiated before it becomes viable as a reliable, cheap and effective solution. A topical review in 2017 summarised the key inhibitors below [44]:

1. Lack of reliability and field operation data.
2. Reduction of AC loss, particularly through conductor design.
3. Magnetisation and demagmetisation of bulk superconductors.

4. Cost of superconductors.
5. Focussed specification for cryogenic system development.

The remainder of this thesis will present the design, manufacture and testing of a superconducting motor that has been aimed at helping to further the cause of item number 1 & 2 by providing a novel A.C. loss testing platform for superconductors integrated into a motor environment. It is important the loss measurement platform is adjustable and can be used to quickly test a variety of superconducting windings. New data is provided to the scientific community as a result of this thesis.

Chapter 2

A.C. Loss Measurement Platform Design & Manufacture

Finding A.C. losses until now has been confined to numerical simulation of relatively simple cases and experimental measurement of magnetisation loss and/or transport current loss [42] [41] [120]. Several people have attempted to understand the A.C. losses of 2G HTS coils within a machine environment by simulating a rotor field external to the measurement system or placing windings within an iron core [124] [34] [5] [102]. Whilst these can provide qualitative results and signal important parameters of HTS coil design within machines, it is necessary to assess the performance of these coils within an actual rotating electrical machine for three reasons. First, the complex stator and rotor fields are not simulated verbatim and thus do not actually mimic a machine environment. Second, A.C. losses can be measured in terms of machine parameters such as torque angle, generated voltage or flux density and finally, by building such a platform there is a springboard for further accelerated research into machine development such as quench investigation and fully HTS machines. Thus the content of this chapter includes:

1. Evaluations of several design concepts to allow the simultaneous measurement of A.C. loss within a live machine environment whilst being adaptable for further adjacent research.
2. Detailed design of the selected concept from the preliminary stage.

3. Verification of the chosen design and optimisation of key design variables.
4. Information about manufacturing steps which are particularly pertinent to HTS machine manufacture.

2.1 Design Objectives

Design, build and test of a superconducting machine is a costly affair. From the beginning of the project, which began in late 2015, the primary constraint was cost. The laboratory facilities were another constraint, cooling could only be achieved with liquid nitrogen limiting the design to wet cooling as opposed to a conduction design. Finally, the machine design should be future-proofed to allow easy modification to lower the operating temperature, switch between fully and partially superconducting coils, replace rotor assemblies and test a variety of coils quickly to maximise research output. Thus the primary design objectives were:

1. A Manufacturing cost of less than £100,000.
2. Liquid nitrogen used as the cryogen.
3. Thermally decoupled rotating shaft to prevent external freezing.
4. Integrate a calorimetric loss measurement system inside a rotating electric machine.
5. Adiabatic environment for loss measurement.
6. Easily adaptable rotor and stator.
7. Minimum loss measurement time of 10 hours.

Generally, during the process of machine design, one could start with an analytical design to flesh out the approximate values of important parameters such as current & magnetic loading, volume or power rating before refining the design with FEA programs such as Comsol or JMAG. The additional part of the design process for this machine was the integration of the cryostat, which changes many important aspects of the design process such as bearings, seals and materials. In the course of the design and build new components were used that have not been trialled in a superconducting motor and are discussed further in this chapter.

2.2 Analytical Machine Design

The design process in this section is an analytical one to help scope the important machine parameters to reach the desired objectives listed in section 2.1. The key aspect of building the machine is to measure the A.C. loss and therefore the machine should be capable of driving the HTS to its full I_c which can be approximated as 25% of the straight sample I_c. Due to the complicated electromagnetic environment within a machine the calorimetric measurement method mentioned in section 1.3.3 is more suitable. An axial flux machine would lend well to modification to integrate a loss measurement platform as a single stator coil can be isolated relatively easily and allow nitrogen bubbles to flow unimpeded. A double sided axial flux machine was chosen for this reason.

The first aspect to determine was the physical size of the machine. The cost of manufacture, particularly the expensive permanent magnets, scale exponentially with an increase in the outer diameter of the disc. To keep the design as cheap and simple as possible a non-overlap concentrated winding provides the best configuration, especially for the mechanically sensitive ceramic HTS which does not lend well to bending. Qualitatively, a 4 pole, 12 slot layout provides a good combination of winding MMF quality and simplicity of construction. Of the several topologies available for the axial flux machine a double sided, coreless stator is the most ideal as it virtually removes core losses, which would need to be calibrated out of the measurement of the A.C. loss and minimises the amount of liquid nitrogen required to keep the machine cold during testing. The double rotor prevents axial loading of the shaft bearings, which maximises their lifetime use. The coreless design; however, means a higher volume of magnet material would be required. Furthermore, an extra mechanical air-gap would be introduced vs. conventional machines to allow the isolation of one superconducting coil to form the adiabatic chamber shown by figure 1.5.

Gieras proposed an elemental approach to analytically calculate the power of a disc machine using the Lorentz force and a "current smearing" model shown below [36]. For each annulus of the disc a current is assumed to be radially flowing according to equation 2.1, the model is depicted in figure 2.1.

$$A(r) = \frac{A_{in} r_{in}}{r} \tag{2.1}$$

where

$$A_{in} = \frac{mN_{ph}I}{p\tau(r)} = \frac{mN_{ph}I}{\pi r_{in}} \tag{2.2}$$

Smearing the current in this manner, the elemental torque production is calculated according to equation 2.3.

$$dT_d = rdF_x = r(A_r B_{avg})dS \tag{2.3}$$

where $dS = 2\pi r dr$ (elemental annulus area) so the torque production is:

$$dT_d = r2\pi r A(r) B_{avg} dr \tag{2.4}$$
$$dT_d = 2\pi r_{in} A_{in} B_{avg} r dr \tag{2.5}$$

Performing the integration between r_{in} and r_{out} the developed torque of the machine assuming a constant axial magnetic field density and conductors is

$$T_{em} = 2\pi B_{avg} A_{in} r_{out}^3 k_D (1 - k_D^2) k_p k_d \tag{2.6}$$

where k_D is the ratio between the inner radii and outer radii. Two constants, k_p and k_d are introduced to the equation as pitch and distribution factors to account for winding configurations which impact the optimum torque production.

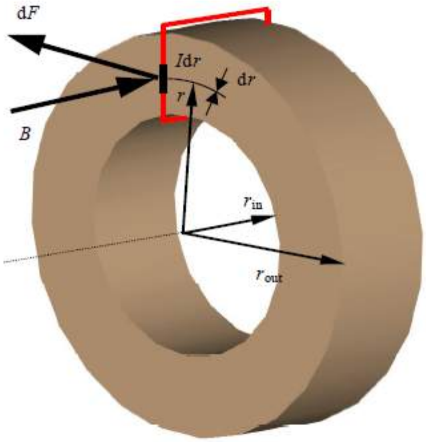

Figure 2.1: Analytical model of an axial flux disc motor [78]. Reproduced under Section 29(1) of the Copyright, Designs and Patents Act 1988.

From equation 2.6 it is apparent there is an optimum ratio between the inner and outer radii which provides the greatest torque. Figure 2.2 shows a plot of the ratio against the electromagnetic torque normalised by the peak value. The optimum is around 0.6 but industrial experience has shown this to vary when the assumptions of the model are not valid due to non ideal flux distribution and end windings. The power can be calculated, for a synchronous machine by multiplying the electromagnetic torque with the corresponding speed i.e. $T_{em} \times \Omega$ where Ω is the shaft speed determined by the supply frequency and pole number as shown in equation 2.7.

$$\Omega = \frac{2\pi f}{p} rad/s \tag{2.7}$$

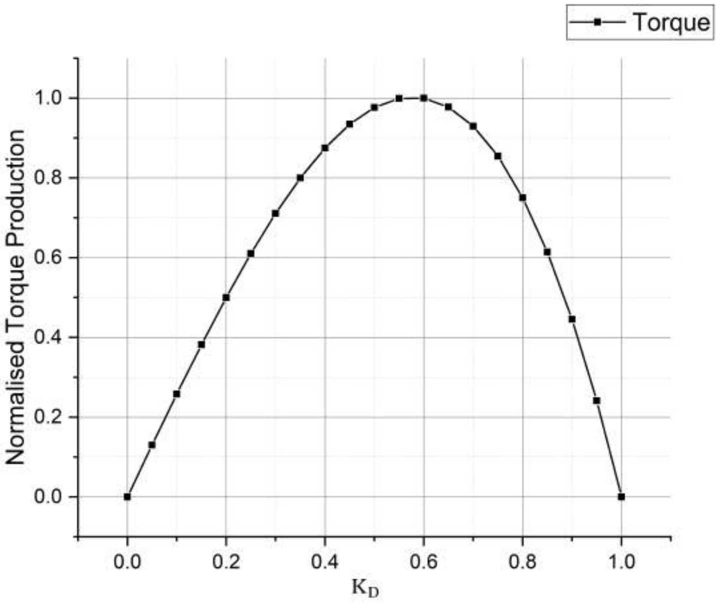

Figure 2.2: For a fixed current/magnetic loading and outer radii there is an optimum ratio between the inner radii and outer radii for disc machines of approximately 0.6.

B_{avg} in equation 2.6 can be estimated using an assumption for the air gap magnetic rotor field. A square, triangular or sinusoidal waveform can be assumed based on a qualitative analysis of the initial rotor layout. For a sinusoidal rotor air gap field, constant across the radii, the average magnetic flux can be found by integration as shown below.

$$B_{avg} = \frac{1}{\pi/p}\int_0^{\pi/p} B_{mg}\sin(p\alpha)d\alpha \tag{2.8}$$

$$= -\frac{p}{\pi}B_{mg}\left[\frac{1}{p}\cos(p\alpha)\right]_0^{\pi/p} \tag{2.9}$$

$$= \frac{2}{\pi}B_{mg} \tag{2.10}$$

As the average flux density can be calculated from equation 2.8, the flux under each pole, Φ_f, can be found using the elemental surface area adjusted to represent one pole pitch i.e.

$$\Phi_f = \int_{r_{in}}^{r_{out}} B_{avg}\frac{2\pi}{2p}rdr \tag{2.11}$$

$$= B_{avg}\frac{\pi}{2p}[r_{out}^2 - r_{in}^2] \tag{2.12}$$

To estimate the average magnetic flux before a more detailed design is completed, a circuital model is used to represent the initial configuration as shown in figure 2.3a. The magnetic parameters of reluctance and MMF translate to resistance and a voltage source shown in equation 2.13 and 2.14. The total air gap is the distance between the bottom of both magnets connecting the crossing flux. The magnetic material, NdFeB, has a different permeability to air (1.05 vs. 1). The "voltage" produced by the magnet is variable according to the grade and type of magnet although for a nominal off the shelf magnet a magnetisation, H, of 875,500$^{A}/_{m}$ was assumed.

$$\Phi = \frac{\mathfrak{F}}{\Re} \qquad\qquad I = \frac{V}{R} \tag{2.13}$$

$$\Re = \frac{l}{\mu A} \qquad\qquad R = \frac{\rho l}{A} \tag{2.14}$$

Figure 2.3a illustrates the baseline configuration of the proposed machine. The steel backing discs are considered to be shorting the magnets due to their relatively high permeance, meanwhile, the airgap and magnets have different reluctances which can be taken into account using Kirchhoff's voltage law to find equation 2.15.

$$\frac{B_r}{\mu_0 \mu_{rrec}} h_M = \frac{B_g}{\mu_0 \mu_{rrec}} h_M + \frac{B_g}{\mu_0} g \tag{2.15}$$

While the recoil line gradient is generally different to the demagnetisation curve it may be approximated using the remnant magnetic field density and coercivity shown in equation 2.16.

$$\mu_{rrec} = \frac{1}{\mu_0} \frac{\Delta B}{\Delta H} = \frac{1}{0.4\pi \times 10^-6} \frac{1.4 - 0}{875500} \approx 1.27 \tag{2.16}$$

Thus, the magnetic volt drop equation can be re-arranged to find the peak air gap flux density as a function of the magnet height, remnant flux density and mechanical air gap as shown in equation 2.17

$$B_g \approx \frac{B_r}{1 + \frac{\mu_{rrec} g}{h_M}} \tag{2.17}$$

The resulting operating magnetic field density options available are depicted in figure 2.4 for varying magnet heights and airgaps.

The main limitation to achieving the smallest air gap is the need for an isolation vessel to create an adiabatic environment and seal off one superconducting coil. A double pancake coil would be used to avoid eddy current losses near the rotor field resulting in a minimum coil thickness of 9mm using 4mm width tapes with a 1mm gap. Additionally, a coil support would be required and some extra space to allow easy flow for the nitrogen bubbles. A 60mm airgap spacing was therefore considered a minimum air gap operating point and a 30mm magnet height was chosen to provide a peak field of 0.4T which translated to an average field of 0.255T using equation 2.8. Finding the air gap field density assumed a steel backing plate of infinite size was used to sufficiently short the magnets. The thickness required of the electrical steel needs to be estimated to avoid saturation and also minimise the total rotor weight. An analytical means to achieve this is to consider the amount of flux that must be accommodated under each pole piece by the steel. Equating the total flux with the steel circumferential cross sectional area, the thickness was estimated using equation 2.19.

$$B_c l y = \frac{1}{2} B_g \frac{\pi d}{2p} l \tag{2.18}$$

$$y = \frac{1}{B_c} B_g \frac{\pi d}{2p} \tag{2.19}$$

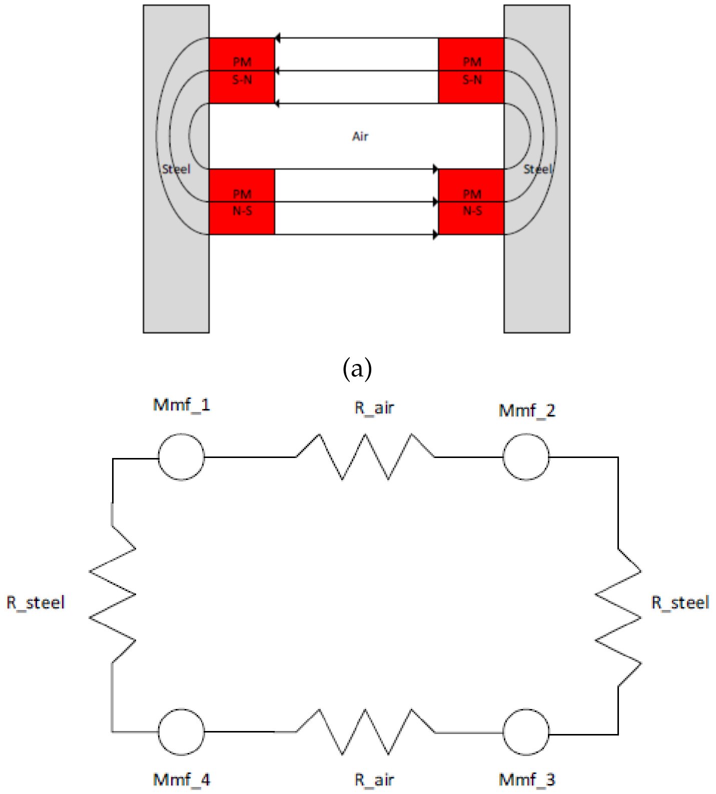

(a)

(b)

Figure 2.3: (a) Path the flux travels across the air gap from the magnets and through the steel backing discs. (b) The magnetic circuit is transformed into an equivalent electrical circuit to estimate the magnetic field distribution within the air gap.

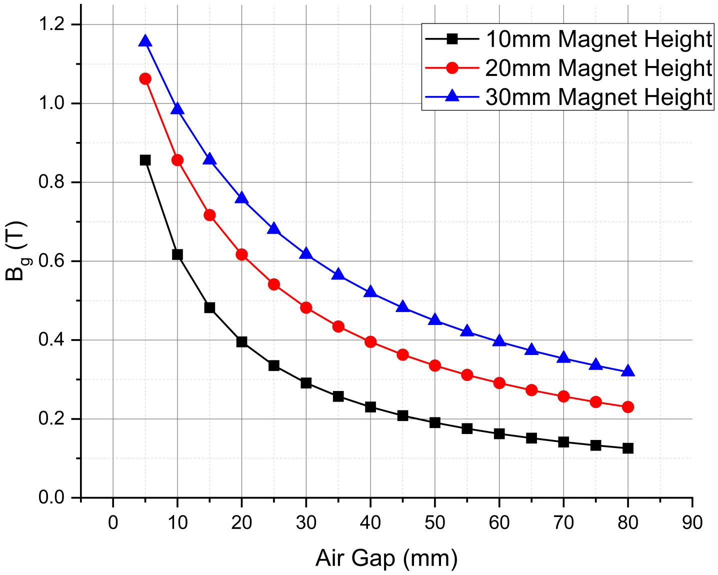

Figure 2.4: Airgap flux density derived analytically to estimate the magnet height and air gap variation effect on the motor operation.

where y is the steel thickness in mm, B_c is the peak core flux (1.4T from experience) and d is the average diameter. The resulting estimated thickness required is 38.57mm.

Estimating the current density achievable within the slots is more difficult than for traditional copper windings as the maximum current is a function of the superconductor stress, strain and its external operating magnetic field environment. To get a best estimate and build experience a double pancake coil was manufactured in a similar technique as described in chapter 4, its corresponding 72A critical current curve after winding is shown in figure 2.5. The critical current depreciated by 50A compared with a straight sample, there would be a further degradation when placed within the active magnetic field of the machine. It has been shown that the current density J_c varies approximately with the external field as $J_c \propto B^{-\alpha}$ and for Superpower tapes has been shown to depreciate the current by approximately one half [90]. Therefore, from figure 2.5 the maximum current that can be supplied to the coil is 35A.

Before the calculation can be completed the inner and outer radii of the disc needs to be determined. The cost of manufacture was the biggest influencer in this decision, it can be seen from figure 2.6 that the permanent magnet cost increases exponentially with increasing radii and an up-

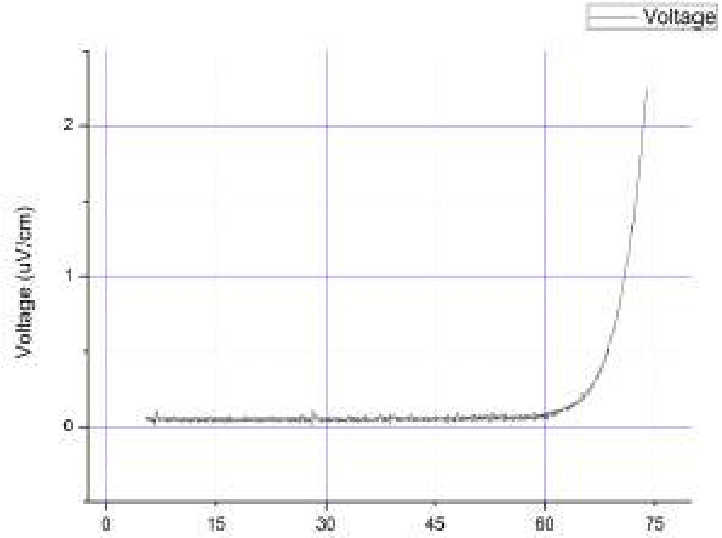

Figure 2.5: A 20m, 60 turn 2G HTS coil was manufactured with heat shrink insulation and then resin wound to estimate the expected linear current density within the machine but also to gain experience in working with superconductors. The accepted criterion of $1\mu V/cm$ was used to determine a critical current of 72A.

per limit of £5,000 for the rotor manufacture was set resulting in an outer radii of 187.5mm. Therefore, the current loading on the inner circumference becomes 16,806$^{A}/_{m}$ derived using equation 2.20.

$$A_{in} = \frac{mN_{ph}I}{\pi r_{in}} = \frac{3 \times 80 \times {}^{65}/\sqrt{2}}{\pi \times {}^{112.5}/{}_{1000}} = 16806A/m \tag{2.20}$$

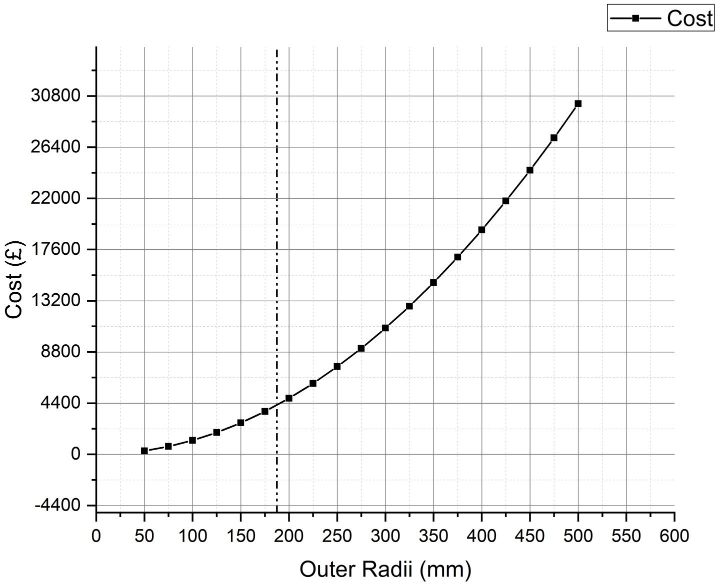

Figure 2.6: The cost of the rotor disc increases exponentially. Budgetary requirements set the maximum rotor diameter to 375mm at a cost of ≈ £5,000.

The pitch winding factor accounts for fractional slot windings which do not allow for an arithmetic summation of the induced EMF and instead require a vector addition. The vector summation of regularly spaced slots will result in a pitch factor shown in equation 2.21. The distribution factor accounts for windings which overlap and are not concentrated, as all of the windings of a single coil fall in the same slot for a concentrated winding, k_d is approximately equal to 1. With an outer diameter of 375mm and an isolation vessel needing to be incorporated within the active region (see figure 2.9) a maximum coil diameter of 100mm leads to a pitch factor of 0.93.

$$k_p = \cos\frac{\alpha}{2} \tag{2.21}$$

where α is the electrical angle of the slot and pole arrangement.

Finally, the initial estimate based on the machine parameters discussed above result in a torque of 11.02 Nm and a power of 6.08 kW at rated speed as shown below, using a formulation based on diameters rather than radii.

$$\frac{3}{4}(0.255)(\frac{35}{\sqrt{2}})80(0.93)(0.375^2)(1-(\frac{87.5}{187.5})^2)\times\frac{1500}{9.5488}=6.08kW$$

6.08 kW power rating assumes the conductors are all lying radially from the center point of the shaft, which would normally be the case for a machine of this type. However, as superconductors are difficult materials to work with due to their ceramic nature normally racetrack or pancake coils are used, additionally these types of coils lend better to simulation modelling as they can be represented by a 2-D problem formulation; thus the actual power is expected to be lower.

The torque constant is an important design values which can be found using the methodology above to relate the developed torque to the applied current. Additionally, the EMF constant relates the voltage required to the operating speed, it may be found by differentiating the rotor field and multiplying by N_1, the number of turns, and the appropriate winding factor. The torque and speed constants are shown respectively in equations 2.22 and 2.23.

$$T_d=\frac{m_1}{\sqrt{2}}pN_1k_p\phi_fI_a=k_TI_a=2.05I_a \tag{2.22}$$

$$E_f=\pi\sqrt{2}pN_1k_p\phi_f=k_E\Omega=0.0716\Omega \tag{2.23}$$

The torque and speed constants are physically that same quantity since they both translate the ability of the motor to convert energy i.e. current to torque or speed to voltage. The co-coefficients shown above are different due to the use of Ω in radians per second and the consideration of only the voltage developed in one phase i.e. $0.0716\times3\times9.54 = 2.05$. Thus, these constants are the same.

2.3 Initial & Final Designs

After the motor design the integration of it into a cryostat was the next stage of the design. Firstly, the configuration of the cryostat was to be decided.

Several ideas were brainstormed to achieve the aims stated in section 2.1. The initial design output three options shown in figures 2.7, 2.8 and 2.9.

Figure 2.7 was the first design pass explored with manufacturers. The benefits of this design was the interception of heat leak via the copper terminals with the use of an extra liquid nitrogen tank at the top. 6 copper feed-throughs can be seen which would feed the 5 coils in the outer chamber and the remaining two terminals for the HTS coil are fed from the top into the adiabatic loss measurement chamber. Additionally, the tubular design would save on machining costs and simplify the shaft feed-through via the flange mounts. A major drawback of the design was the multi-axis assembly that would be needed to operate the machine. Additionally, the rotor would need to be removed horizontally in conjunction with the stator disc which would complicate the experiments. As the stator disc is sandwiched between the two rotor discs it would also be particularly difficult to wire it without making the cryostat larger. This would also require more liquid nitrogen and therefore was not an option due to limited capacity. Due to the stacked nature of the measurement chamber and liquid nitrogen intercept tank, the height may have resulted in operational difficulties too.

The second design shown in figure 2.8 built on the first design by removing the horizontal assembly. The bottom part is rectangular to maintain the ease of manufacturing for feeding the shaft through the wall. A vacuum insulation was also introduced for the measurement chamber alone to reduce the cost and at the expense of removing the copper terminal heat leak with an additional liquid nitrogen tank. The vacuum insulation added more rugged requirements for the feed-throughs which were modified to KF flanges. The drawback of this design was the size, with a vacuum insulation and separate chamber for the measurement the total height was 1.15m which would not be accessible with a floor stand hydraulic crane. Finally, the removable flanges for access to the HTS coil introduce a significant risk when drawing a vacuum. Removable vacuum seals do exist but are costly and if not installed correctly can cause a lot of down time which was the primary reason behind the design's infeasibility. Additionally, to produce a rectangular bottom section there could be an incredible waste of material as it could not be rolled from sheet metal and welded but rather would either need machining or introducing 8 weld points, it was decided the number of welds should be minimal to avoid past issues of vacuum and leak failures.

The final, and selected, design is shown in figure 2.9. It is the most compact of all three options. This was achieved by burying the measurement chamber within the outer liquid nitrogen tank which would remove the need for a vacuum around it. Instead, keeping the cost the same, the vacuum was moved to cover the outer chamber and prevent surface freezing. The move to cover the outside meant the vacuum could be drawn once and isolated with a valve, this avoids the sealing issues. The benefit of the heat intercept liquid nitrogen tank was brought into this design by allowing the feed-through exit compartment to be simultaneously filled with liquid nitrogen resulting in a loss measurement chamber that is covered with liquid nitrogen along all of its boundaries and thus achieving a closely adiabatic environment. The benefit of a single axis of assembly from the second design was incorporated and allowed the vertical movement of the rotor assembly and stator. The rotor was rigidly coupled within the main chamber to the outer shaft to facilitate this. A potential issue identified early on was that the entire motor would be resting on the top flange for support. Due to the thin wall thickness and length of the nitrogen can there were potential for issues with vibration and shaft misalignment which was solved by installing three G10 support blocks inside the vacuum space. A charcoal bag was placed in the vacuum space to absorb moisture and avoid degassing issues over time. As the vacuum jacket had now been moved to cover the outer chamber in its entirety a reliable method of allowing the shaft to exit the cryostat into ambient through the vacuum was needed. Whilst non-contact couplings do exists, they're applications are meant for instances where a small separation gap is possible. In this design the thickness of the cans and the vacuum meant a contact method was needed. A flanged bellows tube is introduced with welds onto the sides of the inner can and the outer wall which allow flex to relieve the welds of stress. The relative movement of the inner can vs. the outer can due to cool down is also taken care of using the bellows construction. The outer bellows tube accommodates the components required to seal the liquid nitrogen including a thermal decouple to prevent the shaft freezing externally, G10 is a commonly used material for this purpose. A fitting port is included to be able to pressurise the compartment and discourage the leak of liquid nitrogen. The compartment may be pressurised by recycling the evaporated nitrogen gas from the main chamber or using an external pressurised gas cylinder. Several design concepts were explored to include a feature to adjust the airgap length including a threading on the shaft and inner radii of the rotors with leverage points on the outer surface to be able to easily move them apart. However, even with the use of a locking screw it was determined due to the large size of the shaft and rotors they could not be machined with sufficient tolerance that would prevent vibration and excess movement resulting in fatigue damage of the shaft. Thus, in order to vary the magnetic flux density it was decided to manufacture two rotor shaft assemblies if it became necessary to adjust the field. A more descriptive diagram and parts list is provided in figure 2.10 and table 2.1.

Figure 2.7: Design option 1. Multi-axis assembly and operational difficulties made it infeasible.

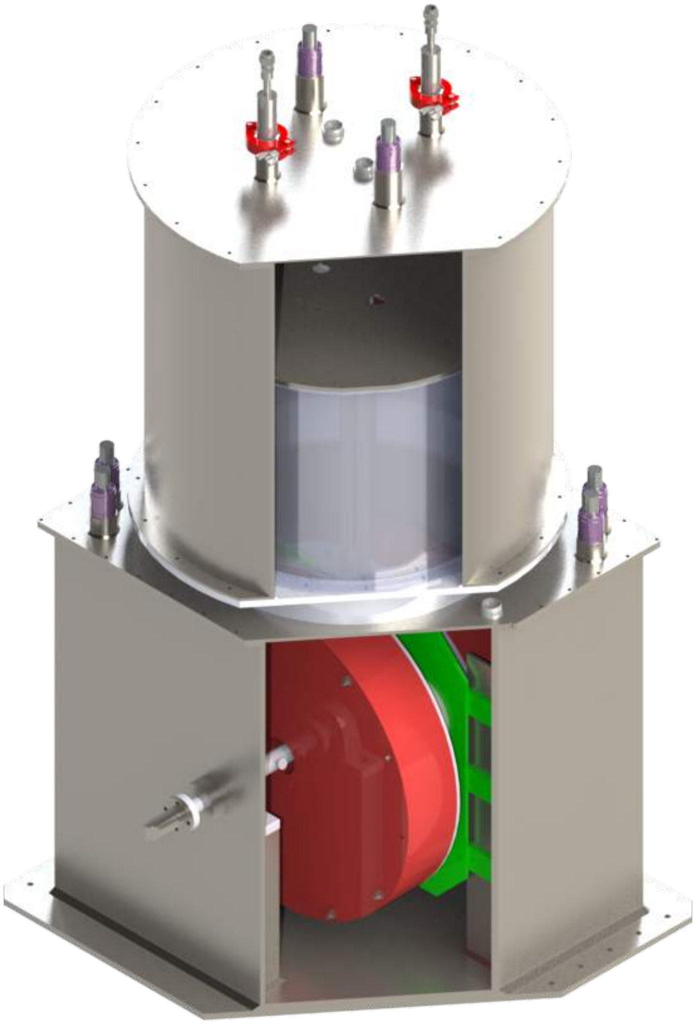

Figure 2.8: Design option 2. Improved operational design with 1 axis of assembly. Vacuum insulation introduced to minimise heat leak. The need for removable vacuum seals made this option infeasible.

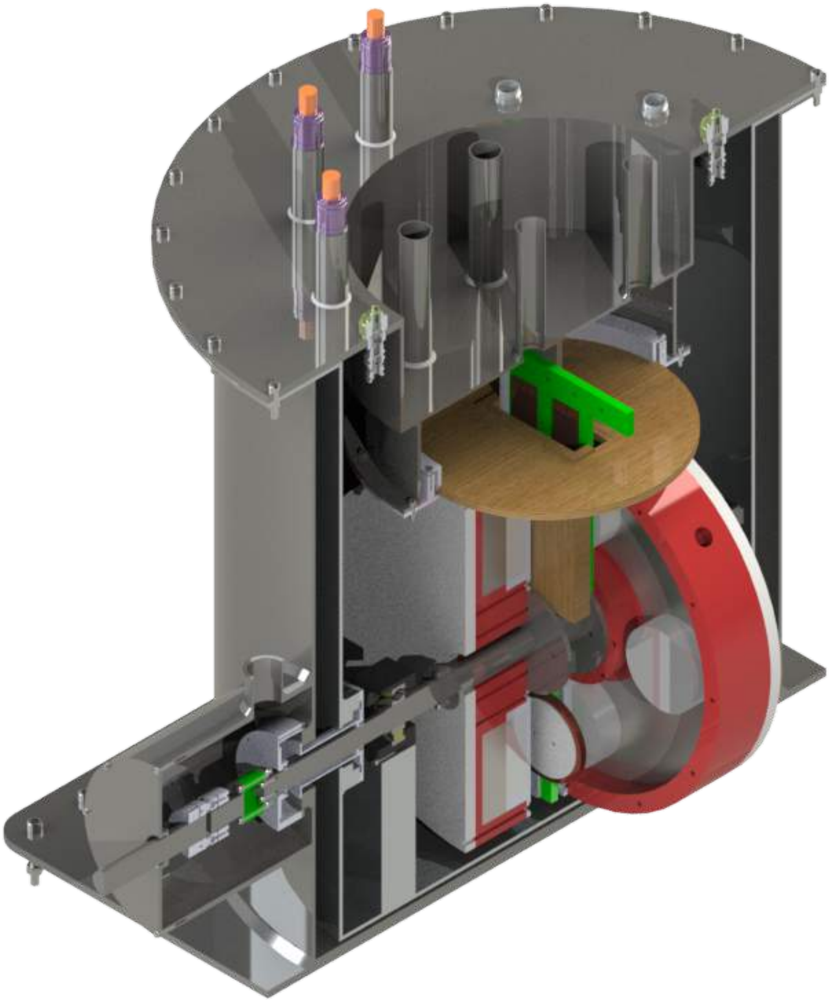

Figure 2.9: CAD model of the final design A.C. loss measurement platform with a cutaway view to expose the isolation chamber, rotor discs and magnets, isolation vessel and sealing methodology.

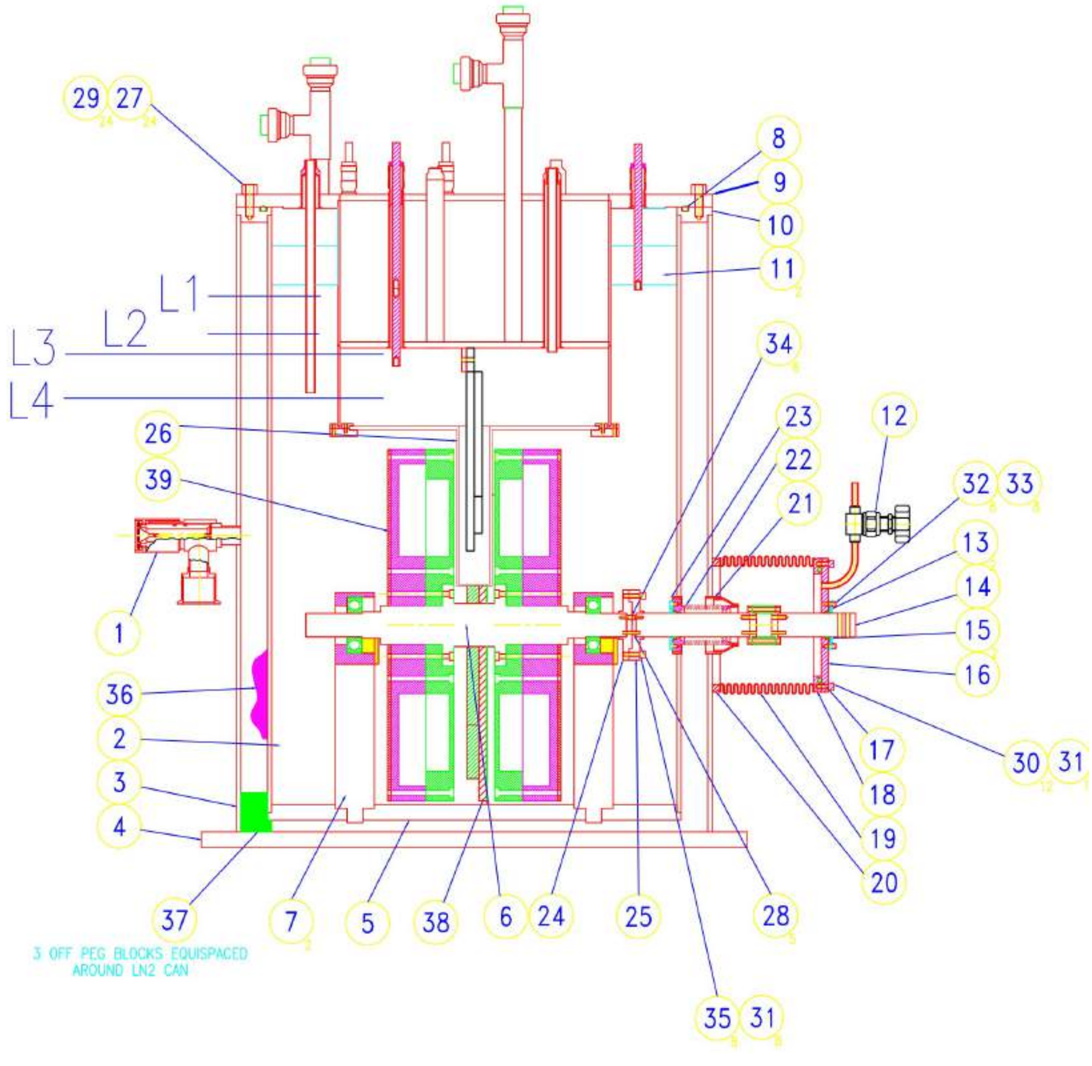

Figure 2.10: GA drawing of the final cryostat design. L1, L2, L3 and L4 refer to the locations of the LN_2 level sensors. L3 and L4 are located inside the loss measurement chamber.

Table 2.1: Major parts & description list of final design.

Part Number	Description	Function
1	Vacuum valve	Pump down and hold a vacuum
2	Inner can	Store liquid nitrogen and house the rotor & 5 stator coils
3	Outer can	Provide vacuum integrity
6	Main rotor shaft	Separate rotor discs
7	Bearing Stand	Support bearings & rotors
8	O-ring	Leaktight storage of LN_2
9	Flange	House power and nitrogen feedthroughs
10	Vacuum Weld	Leaktight endstop for inner and outer can
11	Foam Insulation	Prevent nitrogen ingress to prevent external freezing
12	Swagelok Valve	Pressurise sealing compartment
13	Flexiseal Clamp	Secure seal in place
14	Parker Seal	PTFE impregnated with graphite to seal liquid nitrogen
19	Bellows Ring 1	Allow flex of shaft without stress concentration
22	Bellows Ring 2	Allow vacuum sealing with shaft feedthrough
24,25	Male,Female Shaft End	Rigid Coupling to allow removal of rotor assembly

Continued on next page

Table 2.1 – continued from previous page

Part Number	Description	Function
26	Tufnol Vessel	Isolate liquid and gaseous nitrogen between the outer chamber and loss measurement chamber
36	Charcoal Bag	Prevent vacuum collapse
37	G10 Peg Blocks	Support and prevent vibration of inner can
38	Stator Disc	House the 5 copper stator coils
39	Rotor Disc Assembly	House the magnets and prevent corrosion

2.4 Rotor Design

The two pole pair design was selected from the analytical machine design presented in section 2.2. The magnet geometry is important in determining the harmonic quality of the generated voltage but also the cost. In the U.K. it is cost prohibitive or not possible to purchase non-stock, custom shaped magnets and even magnets above 50mm diameter without a bore [2] [1].

The best torque production of the motor is produced for windings with a strictly radial placement within the active motor area. For computational modelling purposes and ease of winding it was decided to use a double pancake winding [46]. The inner and outer diameter set from the initial sizing laid out in the previous section requires a 100mm diameter magnet. The isolation chamber thickness needed to separate one superconducting coil creates a large air gap of 60mm, to overcome the increased reluctance and achieve a 11.02Nm torque the 30mm thick magnet was selected from figure 2.4. Before purchasing the materials and manufacturing, a 3D model was used to verify the analytical results shown in figure 2.4. The 3D rotor field simulation, displayed by figure 2.11, shows a variation in the peak flux density due to the circular magnet profile along the outer radii, the average flux density was found by finding the flux underneath the pole with a surface integration and dividing by the magnet area:

$$\frac{\Phi_f}{A} = \frac{0.0028141}{\pi(^{50}/_{1000})^2} = 0.36T$$

which is within 10% of the analytical design.

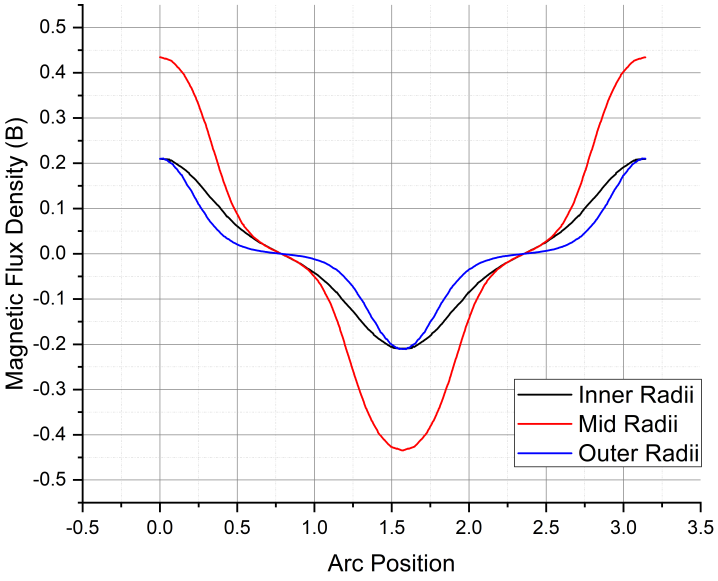

Figure 2.11: Flux distribution along different radii along the mid point air-gap between the two rotor discs.

An issue the analytical design does not account for is the 3D rotor field variation. Figure 2.11 reveals a waveform with harmonic content. Several shapes of magnets were studied to determine the best THD determined by equation 2.24.

$$THD = \frac{\sqrt{\sum_{\infty}^{n=2} B_{n_{rms}}^2}}{B_{fund_{rms}}} \tag{2.24}$$

where n relates to the harmonic mode and $B_{fund_{rms}}$ is the amplitude of the fundamental component.

The rotor configurations simulated are shown in figures 2.12a to 2.12d and were developed by considering easy to purchase stock magnet shapes.

The benefit of reducing the harmonic content is to reduce off-design performance in the form of HTS loss, torque reduction and efficiency. Normally a periodic function, $f(t)$, is represented as an amalgamation of sines and cosines to determine the harmonic content as shown below

$$f(t) = a_0 + \sum_{n=1}^{\infty} a_n \sin(2\pi nt) + b_n \cos(2\pi nt)$$

but the data obtained from Comsol is not periodic, a discrete fourier analysis is used and the integrals are found using the trapezoidal rule in Matlab. The best solution in terms of THD was C1, however; due to disagreements with the best way to manufacture the rotor in a safe way it was decided C3 would provide the best balance. The results of the analysis are presented in the form of a power spectrum in figure 2.13 and the individual waveforms are shown by figure 2.12.

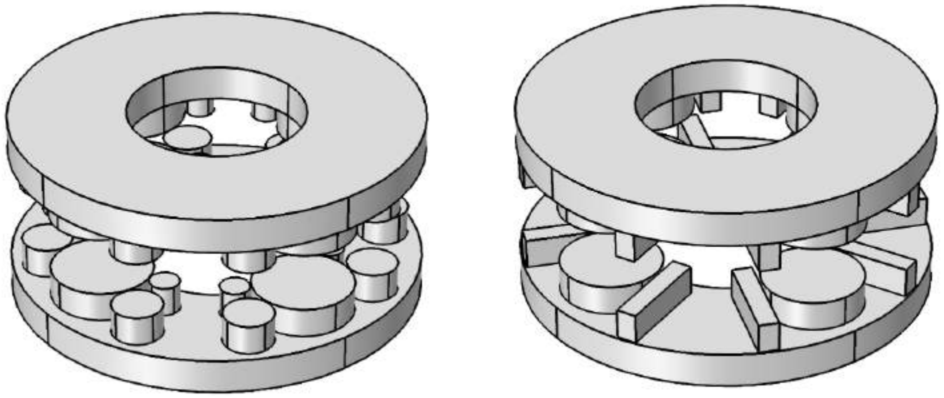

(a) Design C1 (b) Design C2

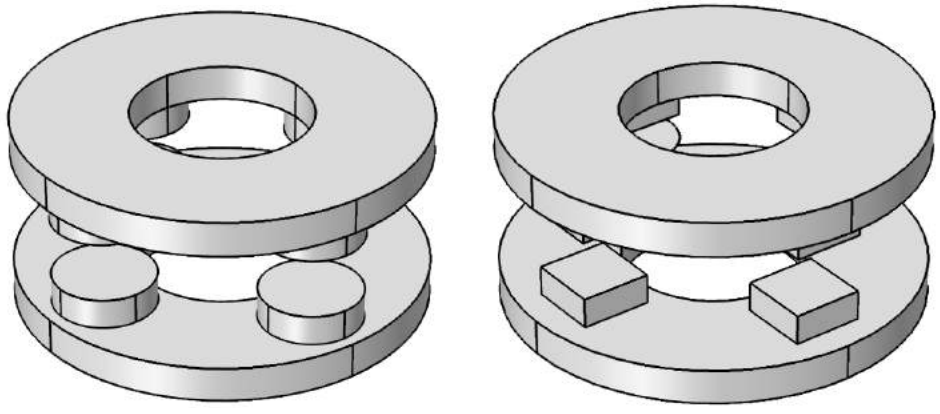

(c) Design C3 (d) Design C4

Figure 2.12: Various rotor configurations derived from stock permanent magnet shapes to reduce harmonics and increase flux density.

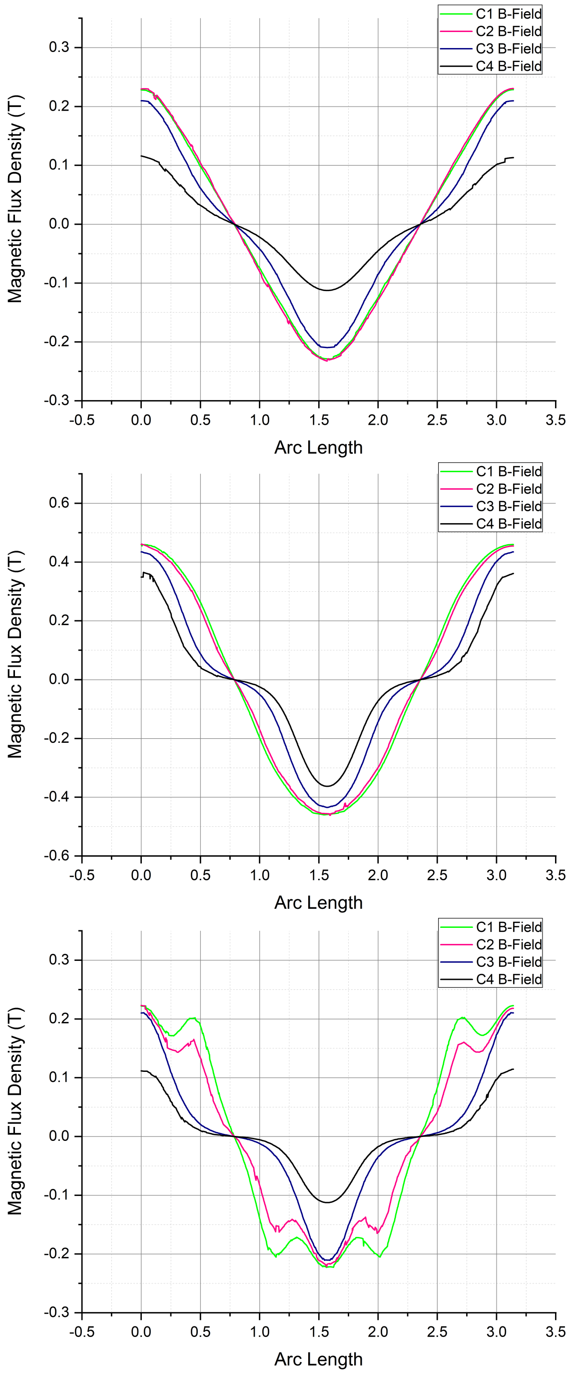

Figure 2.13: Field distributions of various rotor configurations revealing the better design options. (Top graph reflects the inner radii, middle graph is for the mid radii and the bottom graph is for the outer radii).

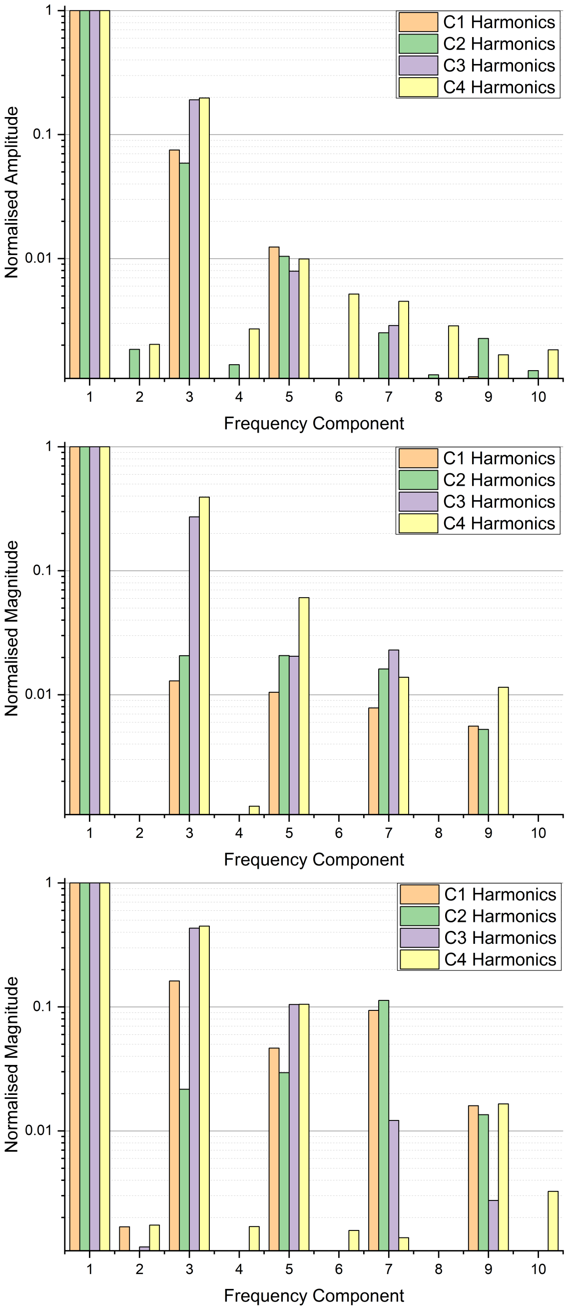

Figure 2.14: Spectrum analysis of rotor fields across the rotor radii. Amplitude figures are normalised by the fundamental frequency amplitude. (Top graph reflects the inner radii, middle graph is for the mid radii and the bottom graph is for the outer radii).

The steel backing disc needs to be correctly sized to avoid saturation and maximise the airgap flux density. In section 2.2 the steel thickness required was estimated to be approximately 38mm. A Comsol simulation of the magnets on the steel disc results in a flux distribution shown by figure 2.15 indicating the minimum sizing is actually 25mm. After speaking with manufacturers, due to a small order LOSIL-400-50A was only available at a 35mm strip width, which adds more weight to the rotor but was unavoidable.

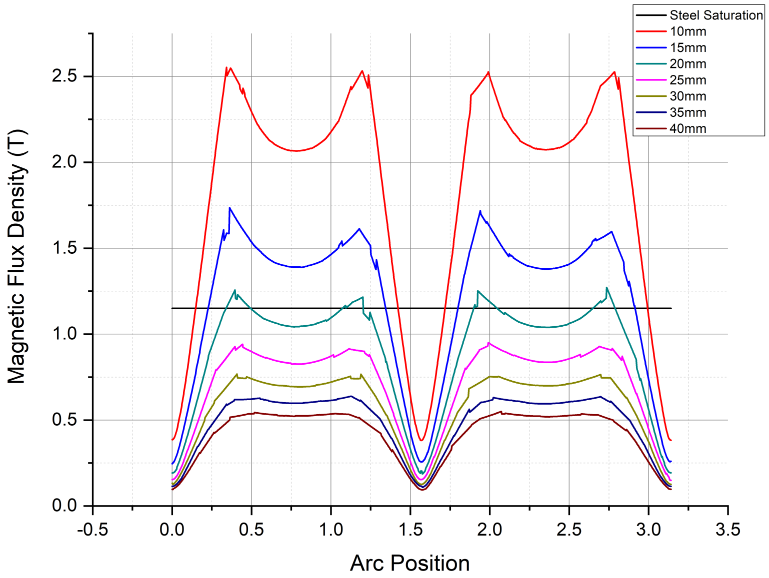

Figure 2.15: Flux density along the underside of the steel backing disc for various thickness's. The horizontal line represents the saturation level of non-grain orientated electrical steel.

In addition to adding weight, the bigger the width, the larger the potential to increase eddy losses; although minimising the backing steel loss was not a design priority an estimate of the loss was sought to ensure LN_2 would not evaporate in the outer chamber prematurely. The Steinmetz equation (2.25) developed empirically has been shown to be accurate for purely sinusoidal waveforms and can be expanded to take into account higher frequency harmonics [85]. It was used to confirm the losses would not be troublesome in terms of liquid nitrogen consumption. α, k_h and k are coefficients dependant on the material and normally provided by the manufacturer derived B-H curve.

$$P_h = k_h f^{\alpha} B_m^k \tag{2.25}$$

Following the design of the rotor electromagnetically, it was important to estimate the attractive force that would be generated between the two rotor discs to plan for a safe manufacturing process. N52 grade magnets are among the strongest available and due to the large air gap in the design, particularly thick magnets have been chosen. Figure 2.17 compares the force generation expected using a standard formulae ($F = {}^{B^2A}/_{2\mu_0}$) and the solution found by integrating the Maxwell stress tensor resulting from the 3D field distribution calculated in Comsol. At minute air gaps the pull force for one magnet can reach up to 230kgf as defined by figure 2.16. Due to the large forces it was decided to use a G10 body to bury the magnets inside of to create a high strength, cryogenic friendly rotor case. As the magnets have a postive feedback loop between force and G10 displacement i.e. a deflection in the G10 will result in higher magnetic force and thus more deflection, a mechanical simulation was carried out to determine the steady state total displacement of the casing. Figure 2.18 shows a maximum movement of 0.06mm in the rotor casing which provided guidance in determining the minimum clearance required between the isolation vessel and rotors. The manufacturing process was designed on the basis of these calculations and is explained further in section 2.7.

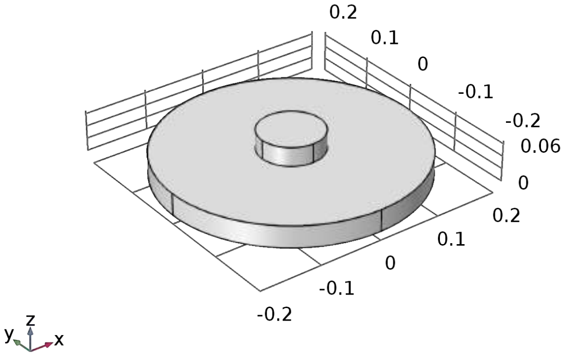

Figure 2.16: Pull force simulation was setup according to the manner defined by industry standards. A piece of sufficiently thick steel was placed below the magnet until no flux leakage occurred on the underside. The maxwell stress tensor integration was used to find the force on the permanent magnet.

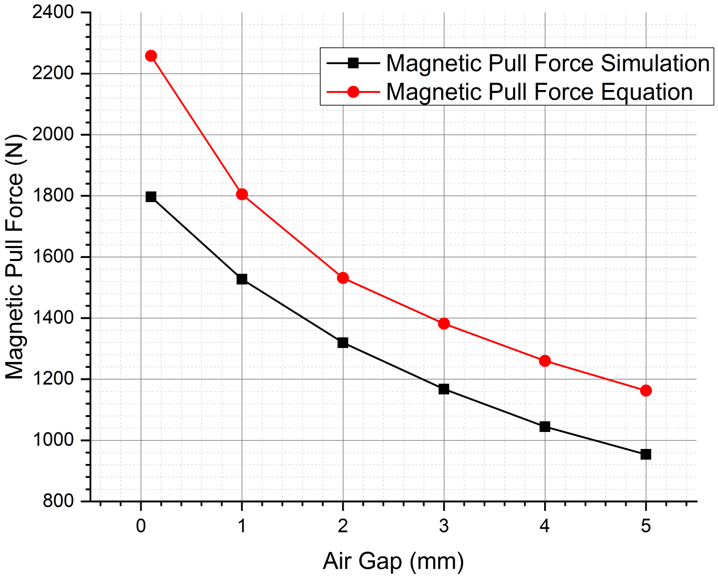

Figure 2.17: Simulation of the pull force of the 100mm diameter NdFeB magnets compared with standard formulae.

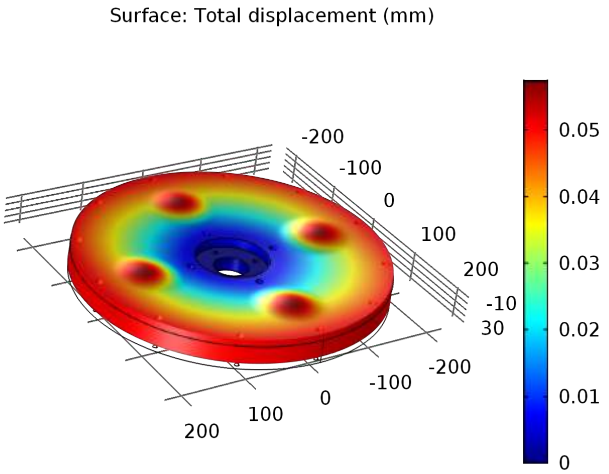

Figure 2.18: Total displacement of rotor disc cover made from G10-FR4 composite.

2.5 Stator Design

The stator design has two aspects to it, the electromagnetic and thermal design. It was decided, to reduce the risk of damaging the costly HTS material, to use one superconducting coil within the measurement chamber and 5 copper coils in the outer chamber. The difficulty in achieving this electromagnetically was the requirement to balance the superconducting line with copper lines so that the motor may be driven with a 3-phase inverter, which generally require an imbalance of no more than 5%. The stator field also needed to be designed to replicate an all HTS stator as closely as possible. Additionally, due to the proximity of the two copper coils either side of the measurement chamber (see figure 2.19), any heat generated could impinge on the isolation chamber and affect the measurements. To create the maximum gap between the coils and isolation chamber the outer diameter of the HTS coil needed to be minimised. The optimum sizing of the coil is determined by the rotor field which is shown in figure 2.11 for a complete revolution. As the magnet has a 100mm diameter the winding inner turn should ideally start at a 100mm diameter. The HTS tape purchased from Superpower was 25m in length and on a double pancake coil this equated to 60 turns on each layer. The thickness of the coil is therefore 4mm leading to a maximum diameter of 104mm to fit within the isolation vessel. The HTS coil has an amp turn of 1800 in a space of 4mm by 8mm. $32mm^2$ can be filled with 21 AWG round wire assuming a 100% packing factor. The limitation for fitting the copper wire in the space is the heat generated. As the copper is enamelled and generally has a melting point of 200 degrees, the maximum temperature should be kept below 150 degrees, this also helps reduce the boil off in the outer chamber. Several AWG coils were simulated in Comsol to find the temperature influence on the isolation chamber as shown in figure 2.20. An 18 AWG wire creates 10K of excess heat on the isolation chamber and there is a non proportional increase in temperature with increasing AWG. Thus the same packing factor achievable with a HTS coil was not possible and a smaller AWG number was needed. To mediate the two requirements of the thermal and electrical designs, the magnetic field created by the stator coils was simulated in the vicinity of the HTS coil to determine which wire gauge and coil size would match closest (see figure 2.21 for setup of stator model) to a full HTS stator. Figure 2.22 displays the field variation for a variety of copper coil aspect ratios (higher ratios would promote the thermal design). A total of 60 turns were required, aspect ratios of 2:30, 3:20, 4:15, 5:12 and 6:10 in terms of axial:radial layout were tested. The 5:12 aspect ratio was chosen as the final copper coil geometry as it provides the best solution balancing the thermal and electromagnetic requirements.

Finally, the use of a HTS coil amongst five copper coils can potentially imbalance the stator and cause the inverter drive to not function. It was important to quantify the amount of imbalance to determine a method of achieving balance. A multi-physics simulation was set-up in Comsol to simulate the coils using FEM whilst the mutual inductances are transferred to an electric circuit model. First, the generated e.m.f. needed to be estimated to enter a realistic value as the voltage sources. Using the rotor fields simulated from figure 2.11 a surface integration across the area of the stator coil was carried out to find a flux of

$$\Phi = \oiint B \cdot dS = 0.0024038Wb \tag{2.26}$$

while the e.m.f. is calculated according to Lenz's law. In a 90° mechanical rotation of the rotor the change in flux is multiplied by two so the total flux linking a single coil is 0.00481Wb. At a nominal 300RPM shaft speed a

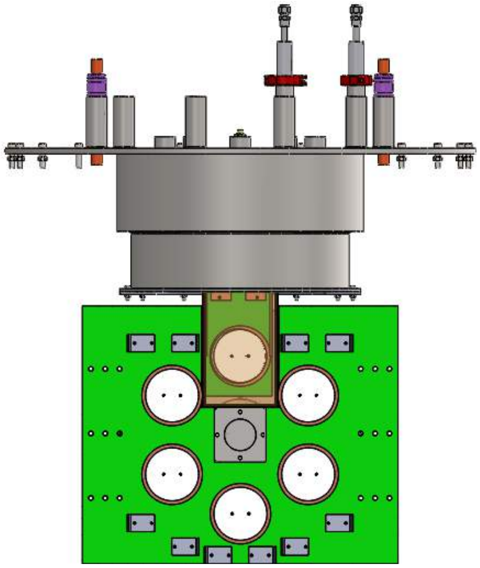

Figure 2.19: Section view of stator coils on a G10 support. The two coils either side of of the isolation vessel have a clearance of less than 4mm. The isolation vessel is transparent to reveal the isolated superconducting coil in the measurement chamber.

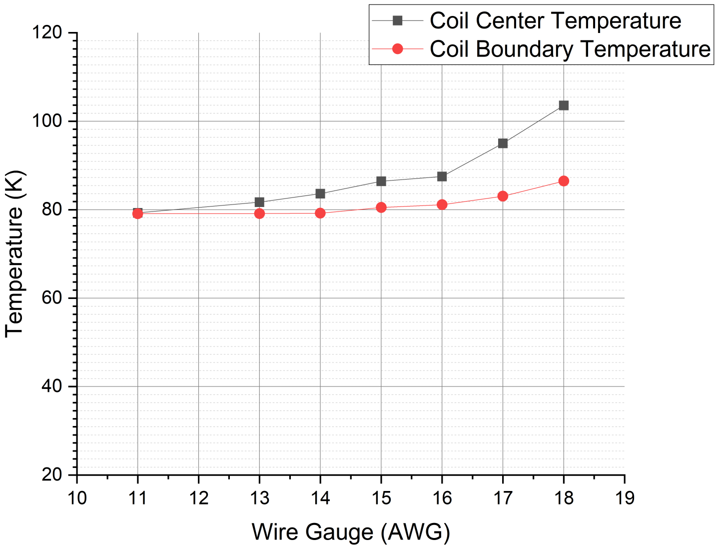

Figure 2.20: Temperature data from the simulations showing the data at the center of the copper coil and at the boundary of the isolation vessel. A value as close to 77K would be ideal thermally.

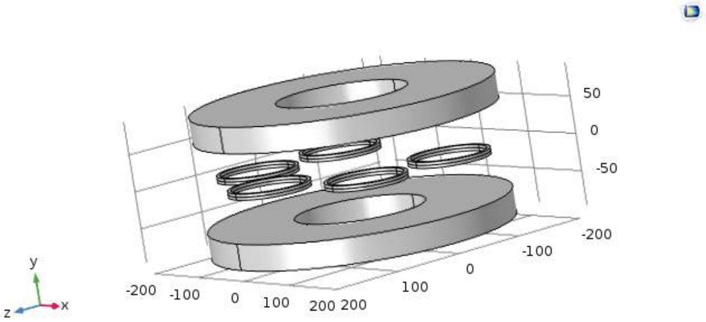

Figure 2.21: A Comsol - Solidworks interface was created to create a sweep of various aspect ratios of the copper coils to determine the option closest to replicating a full HTS stator.

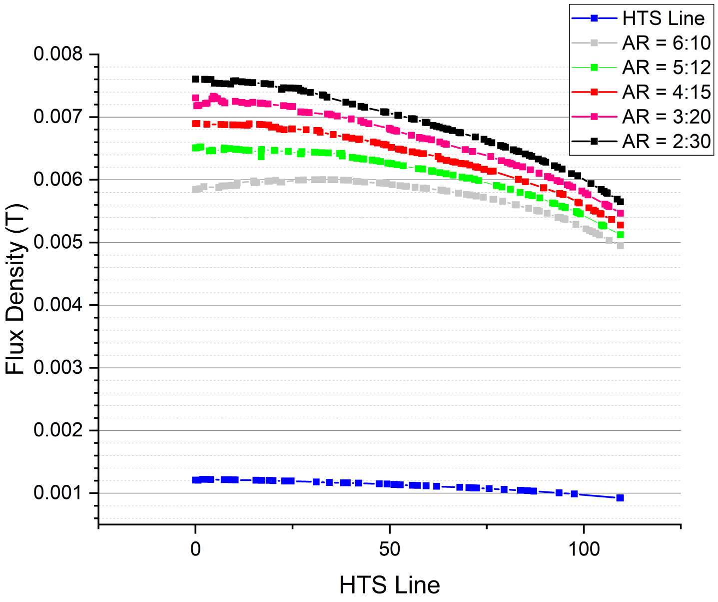

Figure 2.22: Stator field variation in the vicinity of the HTS coil. Despite choosing the optimum aspect ratio for the copper coil the field could not satisfy the simulation of a full HTS stator.

quarter rotation is achieved in 0.05s leading to a voltage generation of

$$\varepsilon = -N\frac{d\Phi \cos\theta}{dt} \tag{2.27}$$

$$\epsilon = 60 \times \frac{0.0048076}{0.05} = 5.77V \tag{2.28}$$

per coil line. Thus each line will generate approximately 11.54V pk-pk. At 300 RPM the generator frequency is 10Hz.

The resistance of the copper coil at a 77K operating temperature needs to be calculated to estimate the impedance of the coil. The resistivity of copper at room temperature is $1.72{\times}10^{-8}\Omega \cdot m$ with a temperature coefficient of 0.004041 per degree at room temperature. In liquid nitrogen the resistivity of copper reduces to about an eighth of that at room temperature ($2.15{\times}10^{-9}\Omega \cdot m$). Using the average diameter, the total length of wire used per coil is

$$(98.95)(60)(\pi) = 18651.64mm \tag{2.29}$$

or 18.651 meters for which a 16AWG wire has a resistance of 0.246 ohms at room temperature and 0.03075 ohms at liquid nitrogen temperature. The resistive impedance of the coil due to the AC operation is estimated to be a quarter of the inductive impedance. The total line impedance expected is 0.12 ohms. To be able to draw 30A RMS from the line at the rated voltage an external impedance 0.15 ohm needs to be employed. As this figure is based on several assumptions some adjustability in the load bank impedance is required to be able to tune the load to the generator. A load bank which is capable of being electronically controlled through LabVIEW and has a load between 0.1 ohms to 0.2 ohms is ideal which accounts for a 66% difference in generated voltage.

Protecting against the risk of damaging expensive HTS wire was a design priority and therefore it was decided to minimise the total length of superconductor used in the initial experiments to just one superconducting coil in the measurement chamber. As mentioned before the remaining coils were made using copper wire and thus have a different electrical and physical characteristic, the impact of the latter was described above. The electrical characteristic is equally important. Driving the 3-phase motor using an ABB ACS310 power inverter requires a balanced load within 3%. To investigate the impact of the use of different coil specifications a multiphysics 3D FEM model was setup in Comsol to simulate the circuit of figure 2.23.

The resulting phasor diagrams are shown in figure 2.24a and 2.24b. The difference caused by the HTS line results in an increased imaginary com-

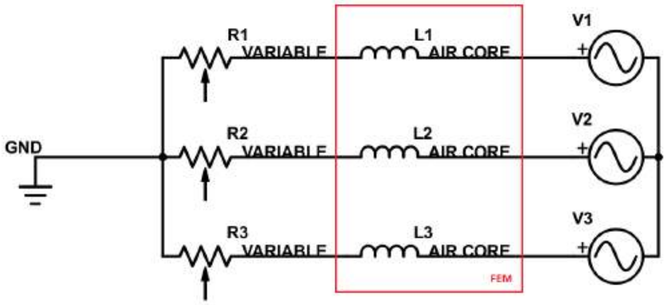

Figure 2.23: Model of the HTS machine simulated with Comsol. The coils were simulated as a 3D coil with different parameters whilst the remaining components are based on electrical circuit analysis.

ponent and reduced real component due to the virtually zero voltage drop. Due to the lack of an iron core and limited turns the current lags the voltage by around 20°. V_1 is the HTS voltage source whilst I_1 corresponds to the HTS line current. The remaining phasors are for the two copper lines. In order to avoid the issue of the inverter the machine may be ran as a generator or in motor operation the load on the HTS line should be increased. Figure 2.25 shows the effect of the imbalance is an issue.

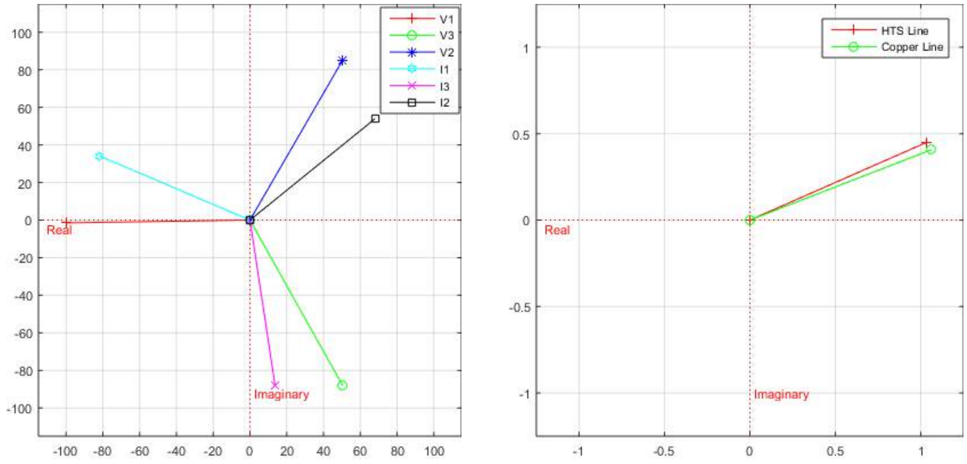

(a) Phasors of the source voltages and line currents

(b) Difference in the impedances of the HTS and copper lines

Figure 2.24: Phasor diagrams showing both the V-I phasors and the loads.

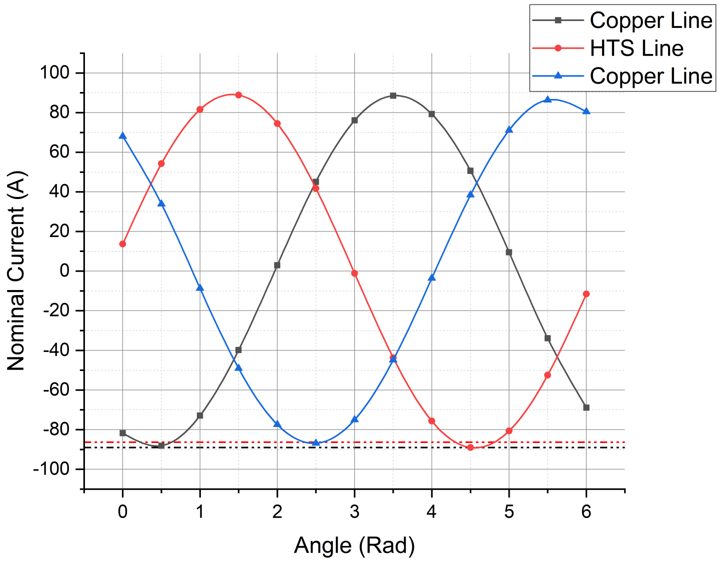

Figure 2.25: Angular plot of all three phases with a clear imbalance caused by the HTS line. The imbalance is around 3% and would be on the edge of the inverter specification.

2.6 Cryostat Design

2.6.1 Vacuum Vessel Design

There are three methods of heat dissipation within the cryostat through radiation, convection and conduction. Thermal radiation due to photons, normally in the infra-red range, create a continuous source of heat. Calculating the thermal radiation for a black body, which assumes the worst possible radiative heat consumption, and assuming an infinitely long surface the heat load can be estimated using equation 2.30.

$$q = \epsilon_a \sigma T_a^4 - \epsilon_b \sigma T_b^4 \tag{2.30}$$

where σ is the Stefan–Boltzmann constant. The conduction loss through the stainless steel can is likely to be the biggest heat load into the chamber. Also, from the point of view of operation the external freezing that would be caused without a vacuum would create a flood in the laboratory which is hazardous and would require a holding tank. The decision to incorporate a vacuum jacket similar to a thermos bottle was a trade-off between cost, necessity and easy of operation. In figure 2.26, which shows the thermal conductivity of air, there are three regimes of interest, above 10^2 torr is the hydrodynamic regime whereby the thermal conductivity is relatively independant of pressure. Below this level and above 10^{-2} is the transitional regime where the thermal conductivity is propartional to the pressure while below 10^{-2} there is a negligible relationship between pressure and conductivity. During the design of the vacuum vessel it was important to determine the correct distance between the inner and outer wall. At ambient pressures the gas heat conduction can be estimated using equation 2.31

$$q = \bar{\lambda} A \frac{\Delta T}{d} \tag{2.31}$$

where A is the surface area, d is the seperation distance, ΔT is the temperature difference and $\bar{\lambda}$ is the mean average of the heat conduction coefficient if the medium is temperature senstitve. Normally a factor of cooling is used for instances of forced cooling. At the low pressures that vacuums are drawn to the fluid dynamics becomes more complicated, to avoid time costly simulation there are tools engineers can use to estimate factors at these extremes. The Knudsen flow number is used to relate the mean free path of gas molecules to the characteristic length i.e. for a cylinder the diameter may be used. In the hydrodynamic region λ is proportional to lN while l, the separation distance, is proportional to $\frac{1}{p}$ and N, the number of molecules, to p. Thus as mentioned before the conductivity is not related strongly to pressure. Below the transition regime i.e. the ultra high vacuum zone the fluid dynamics is a quantum phenomenon and degassing with further vacuum drawing happens by chance. In 1950, Knudsen showed the seperation distance is irrelevant to the gas conduction with equation 2.32 [56]

$$\dot{q} = K a_0 P A_i \Delta T \tag{2.32}$$

where K is a constant depending on the gas, A represents the surface area, and a_0 is the accommodation coefficient. This is a difficult number to estimate and is usually approximated in lookup tables. It represents the collision mechanics of molecules at low pressures with the walls such as energy transfer and surface quality. Equation 2.32 means the question of separation distance is one of pump out speed, total volume and manufacturing practicality.

Foam insulation versus a vacuum insulation costed approximately £5,000 less but was not considered practical as the thickness of the foam required

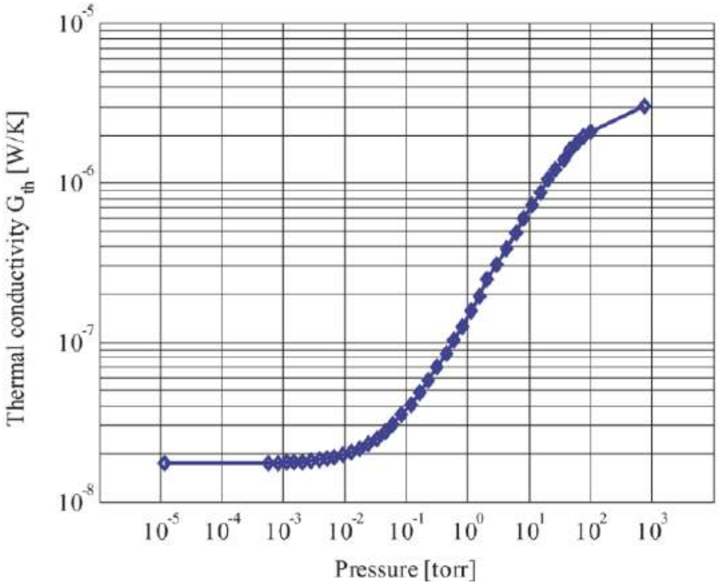

Figure 2.26: Variation of thermal conductivity with pressure of air [94]. Reproduced under Section 29(1) of the Copyright, Designs and Patents Act 1988.

to prevent external freezing was more than 60cm according to the simulation shown in figure 2.27. Within the simulation, the heat transfer coefficient which describes the effectiveness of heat transfer between two mediums is approximately 80. The introduction of the vacuum jacket led to a further design issue. The movement of the inner can with respect to the outer can, due to the vast temperature, result in high stress development between components linking between the cryostat and ambient environment i.e. the shaft, bearings and couplings. Using a thermal contact simulation the estimated height change was approximately 1.5mm as shown in figure 2.28. The subsequent stress developed by this movement was relieved with an Oldham coupling within the sealing compartment and the use of a bellows ring which was welded into the inner and outer can to allow relative movement while drawing a vacuum.

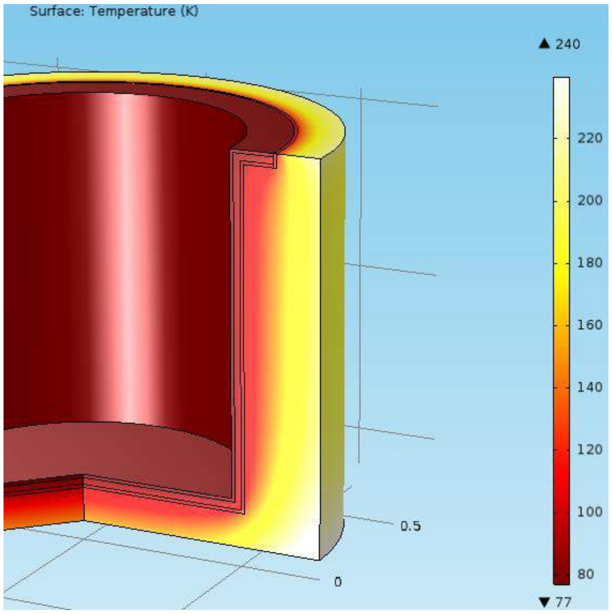

Figure 2.27: Simulation of thermal leak with a foam insulation. Approximately 40cm thickness would be required to prevent freezing temperatures externally.

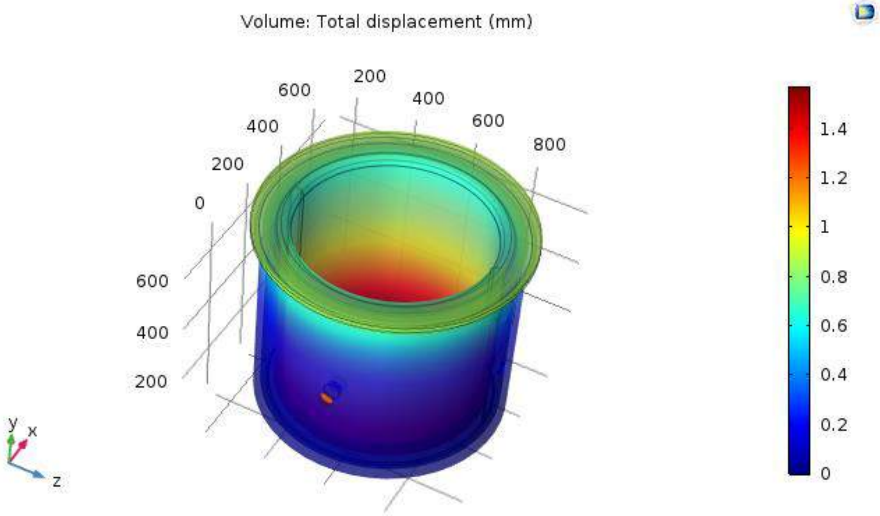

Figure 2.28: Simulation of the relative movements of the cans due to cool down shows a misalignment of 1.6mm

2.6.2 Cryogen Sealing

The liquid nitrogen needs to be effectively contained within the outer can chamber despite the shaft exiting through the inner and outer wall. The difficulty of sealing liquid nitrogen is the extremely cold temperatures rendering traditional means of O-rings or pressurised fluid from working due to their brittling. Some means of achieving the sealing include:

1. Ferro-fluid seals [52] [101]
2. Non-contact couplings [59]
3. Labyrinth seals [80]
4. PTFE Seals [104]

Ferrofluid seals use a magnetic fluid in conjunction with magnets placed on the shaft and static outer casing to suspend a fluid which creates a hermetic seal. This method of sealing is used for vacuums and has been successfully tests with fluids such as water but not liquid nitrogen, many suppliers are not able to guarantee operation under these temperatures so this option was discounted. Non-contact couplings were not feasible as the vacuum jacket increased the air gap above 10mm resulting in large expensive magnets needing to be used. Labyrinth seals have been used to seal liquid and work on the principle of centrifugal forces, it is another contact-less means of sealing which depend on tiny meanders creating a thin gap for the coolant to flow. The rotation of the shaft causes the coolant to become static and prevent outwards flow i.e. the seal would only work whilst the motor is running and therefore would not be effective when experiments have stopped. Finally, PTFE seals are commonly used where metal seals have been avoided due to weight and wear issues. Whilst the material is widely used in cryogenics and the seals have an operating temperature to below -150°C their wear and tear at temperatures significantly below room temperature have not been investigated [99]. As it was the cheapest option, this sealing method was tested in a mock setup of the nitrogen chamber as shown in figure 2.30a and 2.30b to test its suitability. The seal was also tested at room temperature but the fittings were designed for cryogenic temperatures, the larger shaft therefore created increased friction and burnt the seal shown in figure 2.29. Initial motor commissioning was to be achieved at room temperature with copper coils to reduce the risk of damaging the superconductor but for the preservation of the seals, that cannot be done.

Figure 2.29: Overheating of the seal by running at room temperature causes early failure.

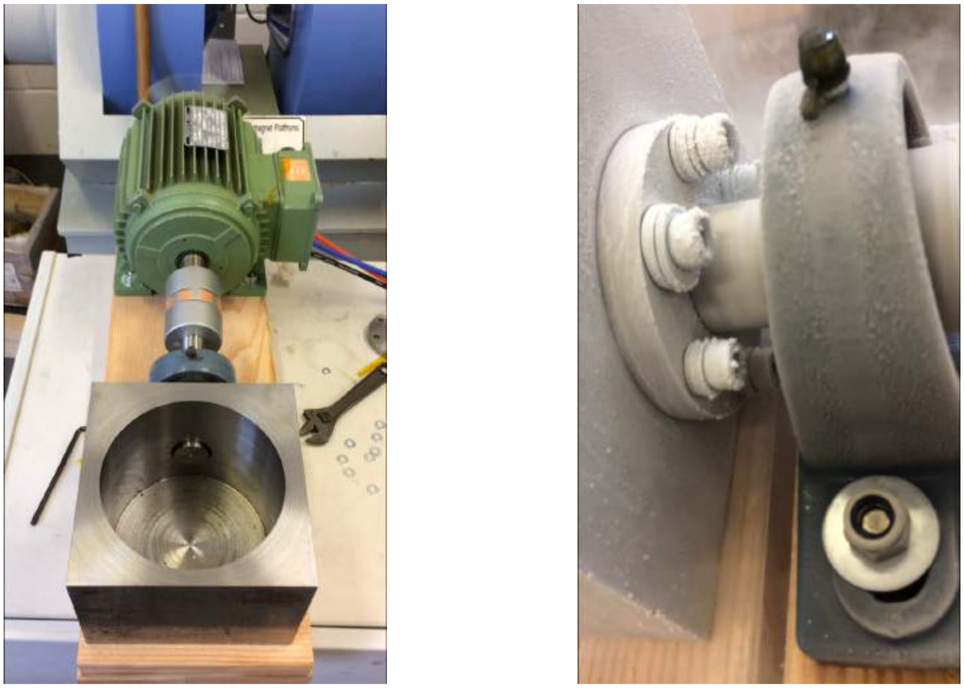

(a) Test rig for PTFE Seal.

(b) No leakage after fill of LN_2.

Figure 2.30: Left: A test rig was setup to trial the PTFE seal and determine performance, which was not available in the literature. A Drive motor is connected to a shaft which enters a LN_2 bath through contact with the seal. Right: After running the motor at 750RPM for 2 hours there was no leakage via the shaft feedthrough.

2.6.3 Bearing Selection

Oil-based or traditional plain sleeve bearings cannot operate at cryogenic temperatures and will seize as the thermal contraction exceeds the design limits or the lubricant freezes. Many research papers focus on contactless bearing solutions for the cryogenic environment using superconductors but these are not commercially available and also would be cost prohibitive [115]. The primary issue for the bearing selection in this design is the thermal contraction mismatch between the stainless steel 304L shaft and the bearing material. Normally, at cryogenic temperatures, ceramic bearings provide good performance due to their hardness and low friction such as zirconium dioxide or silicon carbide. Normally ceramic bearings are coupled with a ceramic or other low thermal expansion shaft material to avoid stress issues but the cost of machining would have been too great. The aim was to have the bearings fit transitionally at cold temperatures without cracking during warm-up with the steel. The thermal expansion of silicon nitride is 3.3×10^{-6} compared with 16×10^{-6} of stainless steel. The bearing shown in figure 2.31a has a 30mm bore and a load rating of 9740 N. For bearings using less than 30% of its rated load the required minimum interference according to the manufacturer is

$$\Delta_{dF} = 0.08\sqrt{\frac{d_{bore} \times F_r}{B}} = 3.179\mu m \tag{2.33}$$

where d_{bore} is the bore diameter, F_r is the vertical loading and B is the inner ring width. The maximum recommended interference is 1/1000 the outer diameter i.e. $30\mu m$. For a nominal shaft diameter of 30mm, an immersion in liquid nitrogen would cause a reduction to 29.896mm, using the biggest clearance for the cold Si3N bearing the inner diameter should be 29.89603 leading to a warm inner diameter of 29.92mm. The result is a large $80\mu m$ interference upon warm up. The bearing was trialled before installation to prove the selection but failed due to the thermal and mechanical shock as shown in 2.31b.

To overcome the issue of mismatched thermal gradients, it was decided to use plain bearings, as opposed to hydrostatic plain bearings, a graphite impregnated metal element was used to provide lubrication to the shaft whilst rotating. Due to the metal matrix the thermal contraction is matched with the steel shaft whilst the graphite makes it malleable enough to form fit the shaft and relax the dimensional tolerance requirements. Additionally the bearing is self lubricating due to the graphite impregnation which is shown in figure 2.32.

(a) CCSI 6306 silicon nitride bearing from SMB Bearings.

(b) Thermally cycling the bearing cause catastrophic failure.

Figure 2.31: Silicon nitride bearings were unsuccessfully trialled with a stainless steel shaft. A sufficiently transitional fit at low temperatures without cracking the bearing at room temperature could not be achieved.

Figure 2.32: Graphite impregnated metal sleeve bearing. The lubrication of the shaft via the graphite is shown as the surface wears away.

2.6.4 Shaft Design

Completing the rotor design leads to information on the loads that are expected to be applied on the shaft. The shaft is used to transmit torque from the rotor discs to the outside of the machine. The torque creates torsion on the shaft, which can cause shearing and angular twisting. Additionally, the rotor discs cause deflection of the beam which are supported by bearings. The importance of designing the shaft to minimise deflection is down to the longevity of the shaft components. Bearing lifetime operation can be reduced to a third of design life if the mating point is a few degrees out of alignment. Shaft design is generally started by understanding the loads and supports on the shaft and an analytical design to attain an approximate ballpark of the diameter required to keep the stresses below a given level. Following this, simulations are carried out to verify the design using FEA.

Figure 2.33 shows the configuration of the shaft and its associated components. Firstly, the weight of the rotor discs must be found in order to determine the force loading on the shaft. The weight of a single rotor disc may be estimated from the design in section 2.4. NdFeB has a mass density of 7,500 $^{kg}/_{m^3}$ whilst the LOSIL steel backing disc has a density of 7,650 $^{kg}/_{m^3}$. The thickness of the steel disc has been set to 35mm while the shaft hole in the disc is 80mm. The total weight of the main components to be installed on the shaft is approximately 100kg i.e. 50kg per rotor disc.

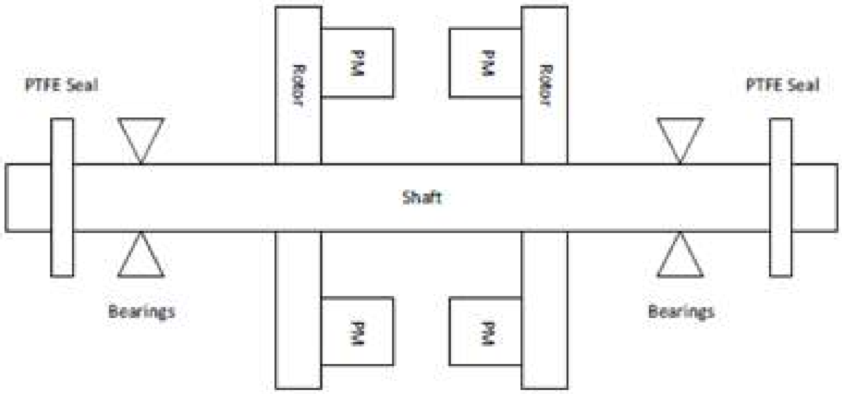

Figure 2.33: Sketch of shaft configuration showing the main weights and support mechanism

The three modes of stress to consider for the shaft to determine the sizing are torsion, bending moment and the deflection. Each of thse modes will constrain the minimum shaft sizing required. Assuming elastic beam theory whereby the shaft weight is negligible and small angle approximations are valid the torsional constraint can be found using equation 2.34 [13].

$$r_{min} = \sqrt[3]{\frac{2T}{\tau\pi}} \tag{2.34}$$

The analytical motor sizing found a torque of circa $11Nm$, upon which a safety factor of 4 is applied to obtain an approximate theoretical torque of 40Nm, resulting in a torsionally constrained radii of 5.899mm. The shear force diagram in figure 2.34 indicates a maximum shear force of approximately 500N. The shear strength of stainless steel can be related to its shear strength by a divisible factor of $\sqrt[2]{3}$ i.e. a shear strength of $^{215\times10^6}/_{\sqrt[2]{3}} = 124MPa$. Thus the minimum sizing dictated by the shear mode is:

$$r_{min} = \sqrt[3]{\frac{80}{124\times10^6\pi}} = 5.899mm \tag{2.35}$$

where T is the torque and τ is the shear strength. The shear force and bending moment figures are calculated using the force variation along the shaft which is related to equation 2.37.

Finally, the deflection mode of failure remains to determine the minimum sizing of the shaft. The vertical deflection of each point along the shaft can be found by integrating the bending moment function shown in equation 2.36 and 2.37 where x is the position along the shaft and F_1, R_1 and R_2 refer to the forces on the shaft, v is the vertical deflection and I_m the moment of inertia. M is the bending moment.

$$\frac{d^2v}{dx^2} = -\frac{M}{EI_m} \tag{2.36}$$

$$M = F_1(x) - R_1(x-51.55) - R_2(x-212.55) \tag{2.37}$$

The double integral of the moment function is shown in equation 2.38. The constants of integration, C & D, are found by setting the two points at the bearings to zero and solving for the unknowns. E for stainless steel 304 is 190GPa while the second moment of area varies according to the radii as $I = \frac{\pi}{4}r^4$.

$$\iint M = \frac{1}{6}F_1(x)^3 - \frac{1}{6}F_2(x-51.55)^3 - \frac{1}{6}R_2(x-212.55)^3 + Cx + D \tag{2.38}$$

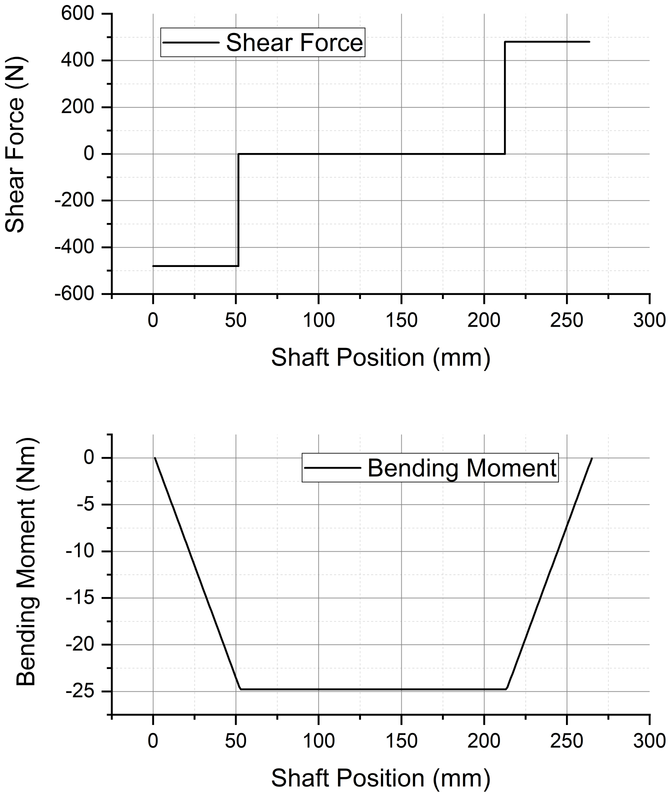

Figure 2.34: Top: Shear force distribution along the shaft. Bottom: Bending moment along the shaft.

The resulting shaft deflections are shown in figure 2.35, from these curves it can be seen that the minimum shaft sizing is determined by deflection rather than the torsional or shear force acting on the shaft.

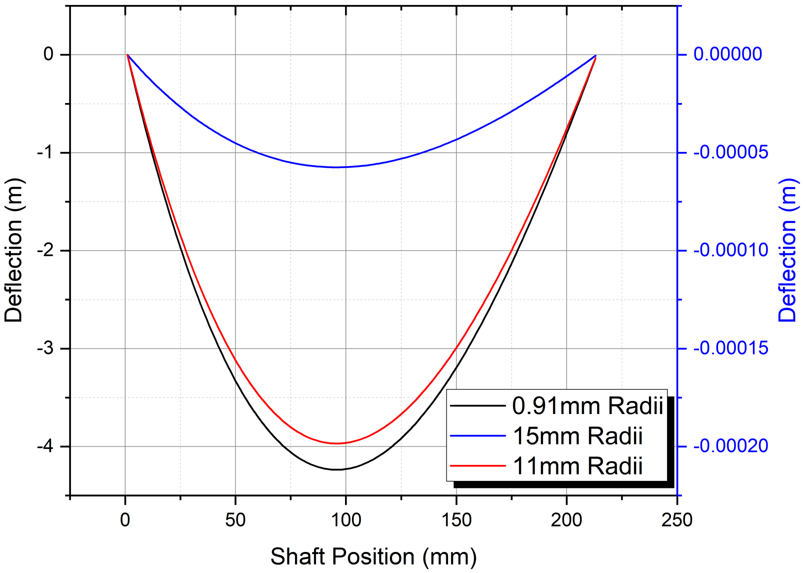

Figure 2.35: Deflection of shaft along the varying positions. The black curve is a radii of 0.91mm (linked to left Y axis). The red and blue curve are linked to the right Y axis.

Using the result of figure 2.35 and differentiating the double integral the shaft angle in relation to the bearing can be found. For the sake of bearing longevity it is ideal to keep the angle to less than 0.1 degrees. Figure 2.36 displays the various angles that would be attained for various shaft radii. To achieve an angle of less than 0.1 degrees a minimum shaft radii of 15mm is required.

A final aspect to consider in the design of the shaft is the high axial force placed upon it by the attracting rotor discs found in figure 2.4. Grooved shoulders will be used to separate the rotors and allow a bigger isolated measurement chamber. The shoulders need to be appropriately sized to ensure contraction of the shaft due to thermal & magnet forces are less than the bearing play. The radial play available in the ceramic bearings was between 5 and 20 microns. The thermal expansion coefficient of stainless steel 304 is $16{\times}10^{-6}$ resulting in a contraction of 0.8mm while the contraction due to the axial force is an additional 0.0025mm as shown in figure 2.37a.

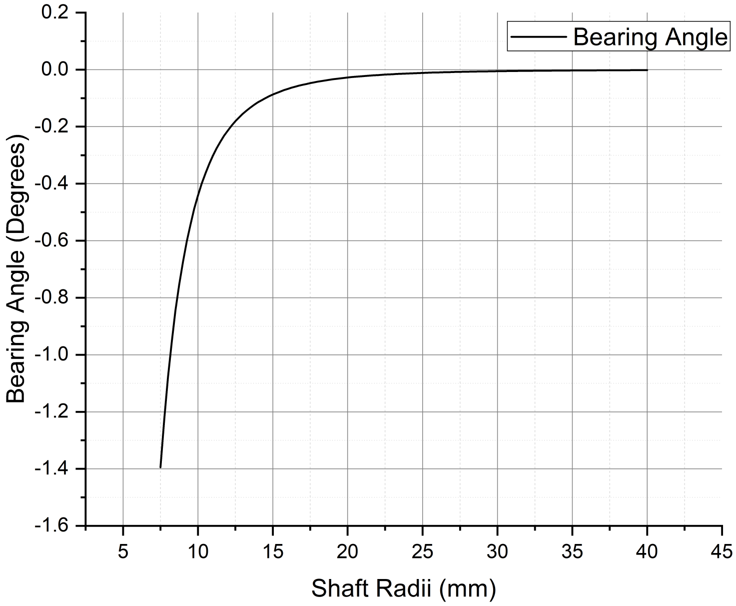

Figure 2.36: Variation of the shaft angle at the bearing points vs. the radii of the shaft. For longevity of the bearings the angle is kept to less than 0.1 degrees.

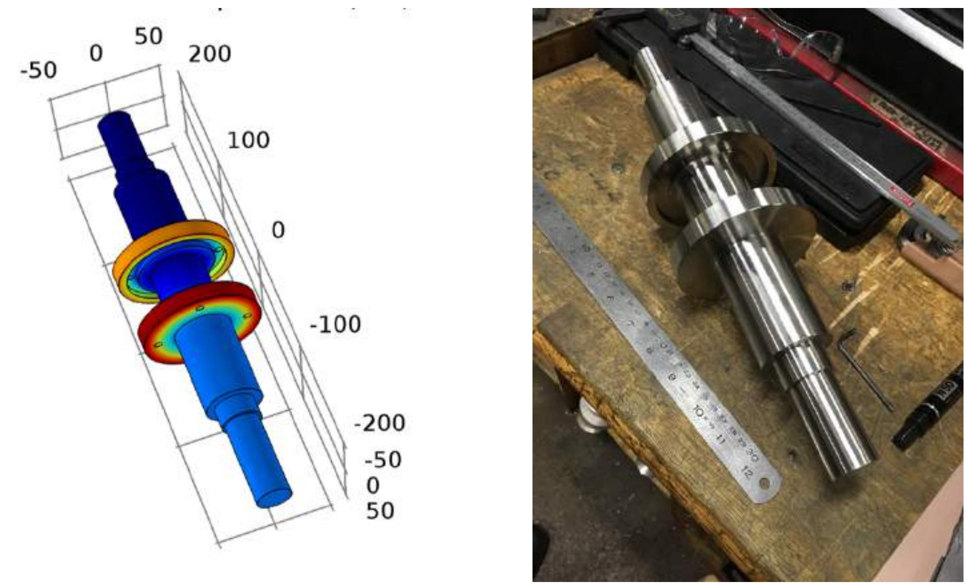

(a) Axial force results in 0.0025mm shrinkage.

(b) Manufactured shaft according to design.

Figure 2.37: The simulated shaft design on the left with the final manufactured version on the right. The contraction was an important factor in determining the correct bearings. Additionally the final manufactured shoulder width was determined to be a minimum of 5mm to prevent failure.

2.6.5 Thermal Heat Leak

In the most ideal scenario the loss measurement chamber would be adiabatic ensuring a stable zero background gas flow. In practice this is not possible to achieve but the thermal heat leak to the chamber can be minimised to make measurements as effective as possible. The two main aspects of heat load into the measurement chamber are from the copper power terminals and the metal skin which creates a contact path to the ambient environment, both serve as great conductors of heat. The copper terminals are an optimisation problem in terms of minimising the heat leak. A smaller cross sectional area may result in a lower thermal heat load due to a smaller contact area with ambient conditions, however, the electrical resistance will simultaneously increase resulting in a higher nitrogen boil off when current is applied. Fourier's law of heat flux is combined with the heat equation to find the heat transfer relationship between ambient and the cryogenic area as shown in equations 2.39 and 2.40.

$$q = -k\frac{dT}{dx} \tag{2.39}$$

$$-\frac{dq_x}{dx} + g = \rho C_p \frac{dT}{dt} \tag{2.40}$$

which is equal to

$$k\nabla^2 T + g = \rho C_p \frac{dT}{dt}$$

where g is the heat generated, ρ is the mass density, T is the temperature and k is the thermal conductivity of the medium, which is 385$^{W}/_{mK}$ for copper. The equation is solved for optimisation in Comsol by setting g to equal I^2R, the Joule loss, and the time derivative is omitted as the steady state is of interest only, thus equation 2.42 is solved for T.

$$k\nabla^2 T = -g \tag{2.41}$$

$$k\nabla^2 T = -I^2 R \tag{2.42}$$

The copper terminal is modelled as a 2D geometry as shown below in figure 2.38. B, C and D boundaries are given Neumann conditions to represent the heat flux due to liquid nitrogen immersion. The heat transfer coefficient of static liquid nitrogen is between 80 and 130$\frac{W}{mK}$ but can vary greatly depending on the temperature difference between the surface and

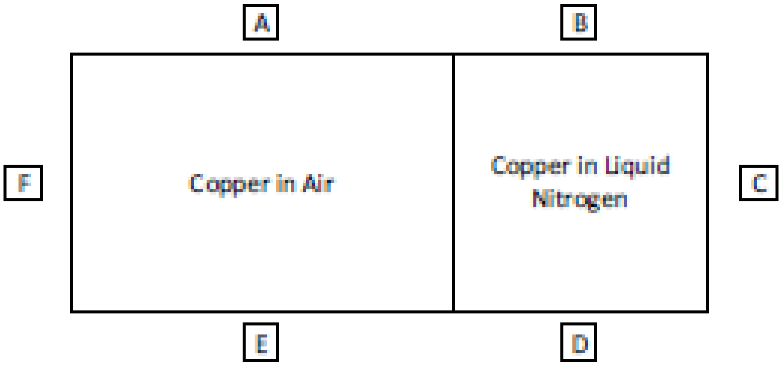

Figure 2.38: Simulation set-up of copper terminal optimisation problem. The copper bar is split into two regions, one exposed to LN_2 and the other to room temperature.

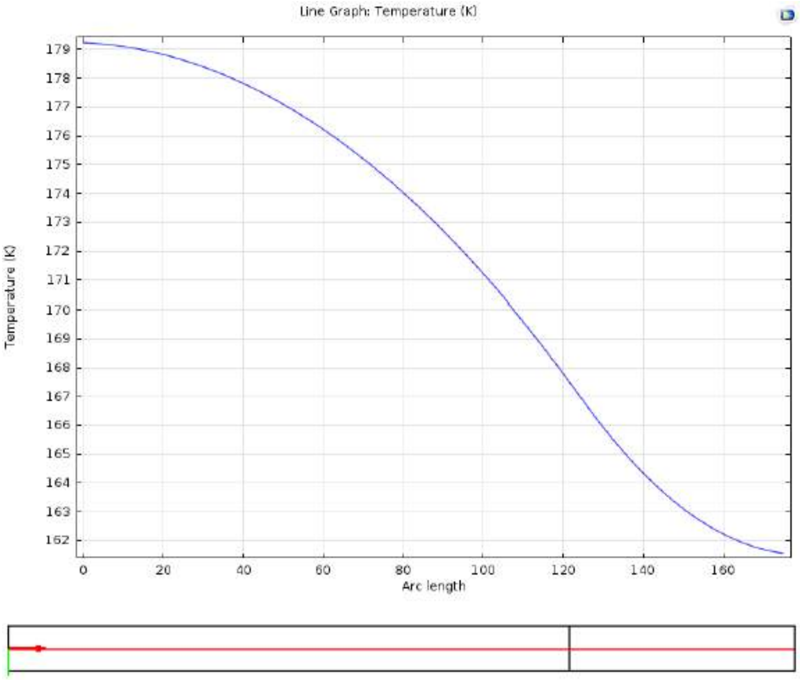

Figure 2.39: Temperature change along a copper bar simulation set up according to the conditions of figure 2.38.

coolant, the static air room temperature coefficient is 20 $^W/_{mK}$ [10] [53]. Figure 2.39 displays the temperature variation along the middle of the copper terminal, there is clearly some freezing expected externally.

With the surface temperature distribution found the heat flux is calculated according to equation 2.43 where x is the path along the surface of the terminal, L_1 and L_2 are the surface limits, T_{ext} is the surface temperature and T_{int} is 77K. Liquid nitrogen has a latent heat of vaporisation,h_{latent}, equalling approximately 199$^{kJ}/_{KG}$. The volume density of liquid nitrogen is 0.806 $^L/_{KG}$, therefore the total volume may be calculated once the heat load is known according to equation 2.44. The minimum total heat load occurs at a radii of approximately 3mm and a heat load of 0.2W according to the optimisation results shown by figure 2.40. At this rate of heat load the liquid nitrogen boil-off would be approximately 0.0514 SLPM, which is less than 2% of the Omega FMA 2710 flowmeter range.

$$Q = \frac{1}{h_{LN_2}} \int_{L1}^{L2} (T_{ext} - T_{int}) dx \tag{2.43}$$

$$m = \frac{Q}{698} \tag{2.44}$$

where m is the litre flow and 698 represents the mass to gas volumetric conversion for nitrogen. The large variation in h_{LN_2}, the heat transfer coefficient, can be judged by equation 2.45 and affects the optimisation problem [53]. A piecewise function is used in Comsol to model the variation.

$$h_{LN_2} = \begin{cases} 125 + 0.069\Delta T & 52 \leq \Delta T \leq 214 \\ 13087.8 - 723.04\Delta T + 13.48\Delta T^2 - 0.084\Delta T^3 & 19.6 \leq \Delta T \leq 52 \\ 21.945\Delta T & 0 \leq \Delta T \leq 4 \end{cases} \tag{2.45}$$

Another key source of heat leak into the measurement chamber is from the stainless steel flange, which compared to copper has a much lower thermal conductivity of 16.8$^W/_{mK}$ but has a large surface area and exposure to the ambient environment [100]. The final design configuration from figures 2.9 and 2.10 provide the outline dimensions of the components that affect the heat leak, primarily from items 9, 10, 27 and 29. The isolation chamber, item 26, is also a heat load but its thermal conductivity is comparatively much lower. Additionally the surrounding of the chamber is liquid nitrogen and therefore it is well insulated and not considered a large source of heat load. Figure 2.41 shows the temperature variation as the flange is externally filled with liquid nitrogen to intercept this heat load at various fill levels. A 100% fill clearly shows there will be external freezing which needs to be taken into account when running experiments but is needed since figure 2.42 shows that a 0% fill would result in a 100W+ heat load on the measurement chamber, far in excess of the Omega FMA 2710 flow meter range but is severely reduced for even a 50% fill level.

Combining the heat loads from figure 2.40 and 2.41 an estimate of the maximum and minimum background flow resulting from the heat load can be derived and therefore an estimated operating time for experiments, which needs to be at least 10 hours to allow for data gathering and flow settling. Due to cost considerations a 10mm diameter copper power terminal was used, assuming a 50% full flange the total heat load is approximately 4.06W. Thus, using the latent heat of vaporisation and volumetric density, the operating time is

$$(10)(0.81)\frac{199000}{4.04} \div 3600 = 109 hours$$

which is more than sufficient. The nitrogen consumption resulting from the heat load will be transferred to outside the measurement chamber and the flange LN_2 tank will need to be continuously topped up. Without the provision of the liquid nitrogen tank the heat load would result in an operating time of 2.75 hours and a background flow of 42 SLPM.

Minimising external freezing is a priority in the design for two reasons. First, there are safety issues involved with water shorting power leads or creating puddles on the laboratory floor. Second, external freezing essentially increases the head load to the coolant. Whilst the C&I feedthroughs, power leads and measurement chamber have been optimised the outer liquid nitrogen tank, which is vacuum insulated and houses the rotor, has an additional heat leak via the shaft. There are several techniques used to minimise the heat load due to a shaft connecting the cryogenic environment with ambient components. A ceramic or epoxy glass fibre material may be used to reduce the thermal conductivity although this is expensive from a machining point of view. Secondly, a magnetic coupling may be used which would remove the need for a hole through the vacuum walls and reduce the shaft head load to zero [76]. However, due to the curved design of the cryostat outer wall and the vacuum gap, the air gap would be too large for cost effective permanent magnet couplings. Instead, many demonstration machines listed in table 1.1 have used a G10 thermal break along the shaft to introduce a heat conduction break [81]. Essentially a ring of low thermal conductivity material is rigidly connected to the shafts as shown

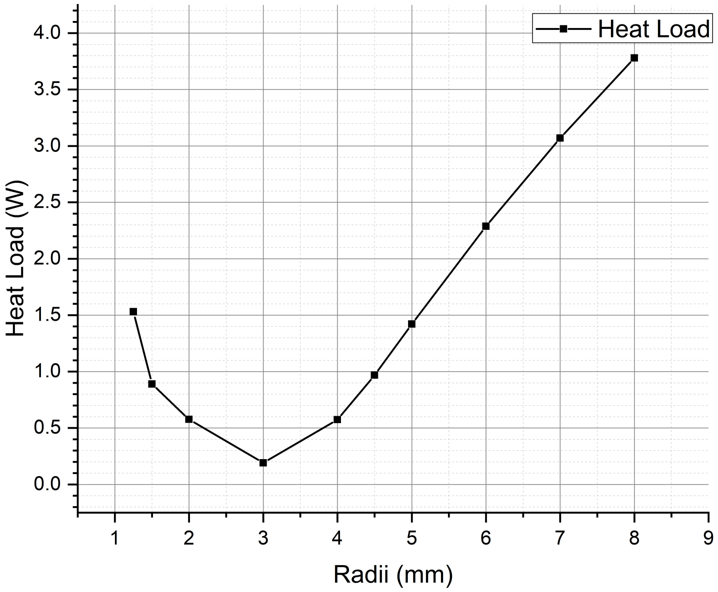

Figure 2.40: Variation of heat leak with different copper terminal radii. The optimum radii is approximately 3mm.

in figure 2.43. The outer nitrogen tank is not as important in terms of liquid nitrogen conservation as it can be continuously topped up with a permanent connection to the LN_2 fill point. What is important is to avoid freezing on the outside. Using G10 with a thermal conductivity of $0.3^{W}/_{mK}$, a hollow tube was used instead of a block or pegs to increase the strength while reducing the contact area. Figure 2.44 shows the correct sizing required of the G10 break with a 50mm outer diameter and 30mm inner diameter tube of 30mm length. Whilst the thermal constraint is satisfied the tube needs to be able to mechanically deal with the torque as there is a trade-off between the shell thickness, i.e. the strength, and its resistance to thermal conduction. Keeping below 30% of the yield strength of G10, which is approximately 60MPa, requires a shell thickness of above 3mm as shown in figure 2.45.

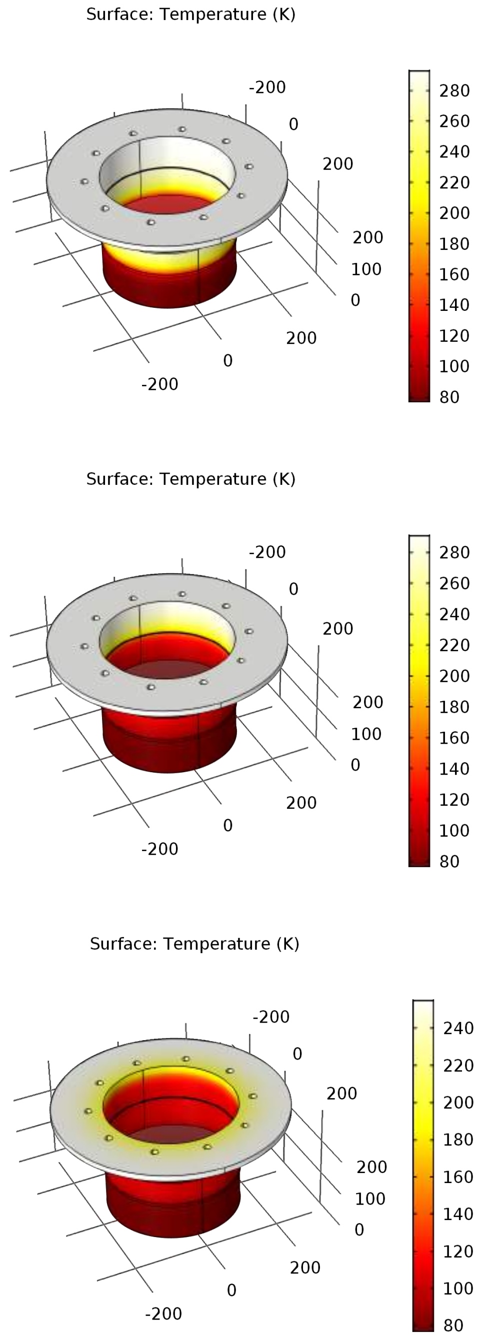

Figure 2.41: Top: 0% LN_2 fill, Middle: 50% LN_2 fill and Bottom 100% fill.

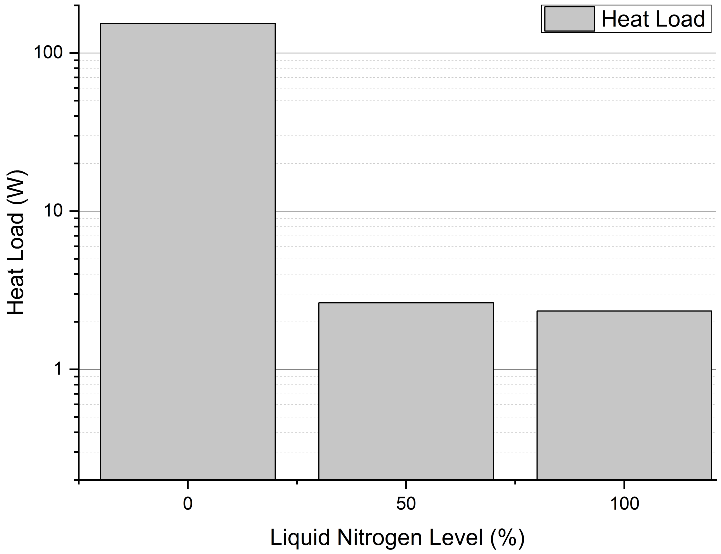

Figure 2.42: The total heat load due to liquid nitrogen filling in the flange. Without the flange recess and liquid nitrogen there would be excessive heat load that would require an expensive flow meter with a big range and lower accuracy.

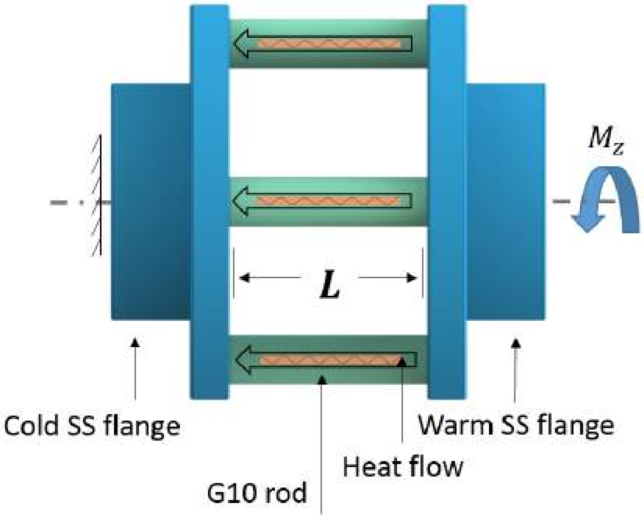

Figure 2.43: G10 thermal break concept. G10 pegs are used to minimise thermal contact between the two metal shafts [81]. Reproduced under Section 29(1) of the Copyright, Designs and Patents Act 1988.

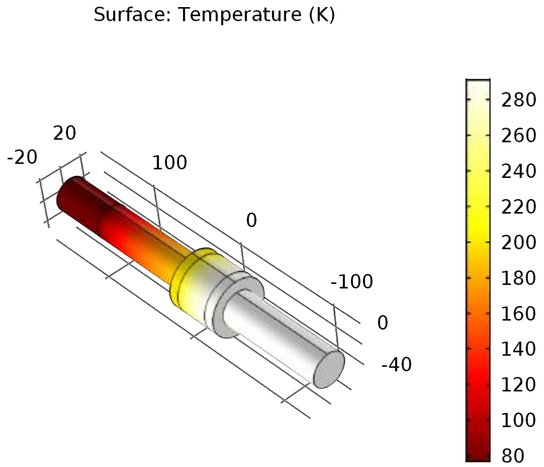

Figure 2.44: The hollow G10 tube acts as a thermal break between the ambient and cryogenic environment shafts. The outer shaft temperature is 292K.

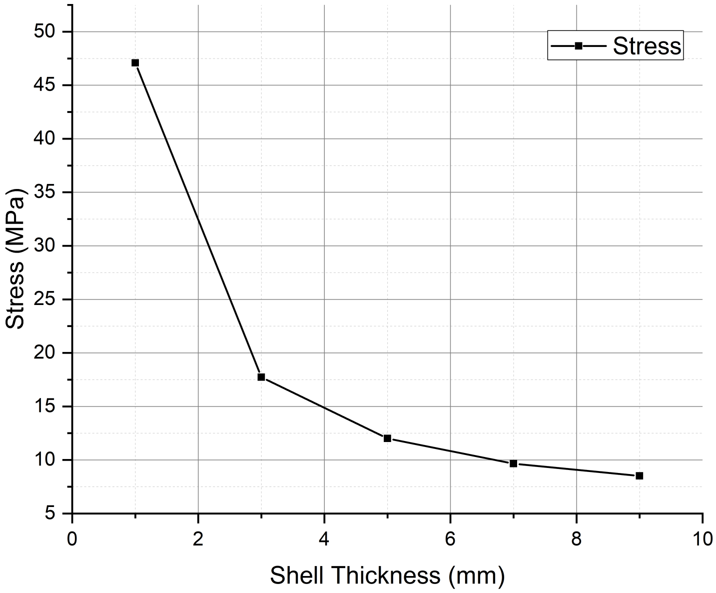

Figure 2.45: A shell thickness of minimum 3mm was chosen to limit the stresses on the critical thermal break component.

2.6.6 Isolated Measurement Chamber

As previously mentioned in section 1.3.3 it is important to maintain as close to an adiabatic environment as possible to maximise accuracy and resolution of the A.C. loss measurement. Three design points have the potential to affect the background flow, namely; these are the heat leak from the room temperature environment into the chamber through conduction, radiation and convection, potential eddy current losses in the isolation barrier and leakage between the measurement chamber and outer chamber. The eddy current aspect can be mitigated by using a material for the barrier that is non-conductive. Whilst this seemed like a trivial decision, in actuality, the unique shape of the isolation vessel and operating temperature made it more challenging. The cryogenic temperature limits the use of materials to those such as metals, reinforced plastics, resins or specially treated glass. Ideally the vessel would be made from one piece to prevent the leakage issue but due to the depth of the hole required it would be difficult to mill, also glass-blowing was not an option as the rectangular shape and precision required were too stringent. In order to test the effectiveness of the sealing between the measurement chamber and the isolation vessel a small scale mock-up of the technique was manufactured as shown in figure 2.46 and the test set up is shown in figure 2.47.

A heater was placed underneath the glass vessel to produce more bubbles and replicate the operating environment. Two sets of experiments were conducted to determine the effectiveness of the sealing technique. Once with the glass vessel in place and once without. Figure 2.48 shows the results of both of these tests. It shows that when the glass plate was absent the nitrogen was free to flow through the meter, the negative flow rate was due to opposite connection of the terminals. At 0 seconds when the liquid nitrogen was first poured in a large flow rate occurs, the slow decrease in the flow marked by 'A' is due to the lower thermal gradient between the metal chamber and the liquid nitrogen reducing the overall boil-off. 'C' shows the point where the flow-meter was briefly manually blocked off. 'B' shows the various points where the heater was turned on with varying powers and duration. It is clear that nitrogen gas flows through the meter as expected. On the other hand the black curve shows the equivalent flow rate but with the sealing technique in place. The same procedure was followed and the heater was used to generate more bubbles but no leak can be detected by the flow-meter.

The success of the sealing technique meant it would not be necessary to use a physically bonded method which would make modifying the cryostat

Figure 2.46: Small scale version of sealing technique used for the loss measurement platform. A compression is applied to the glass face which sits on a metal lip greased with apiezon N. An indium seal is used on the external flange to prevent liquid nitrogen or gas ingress.

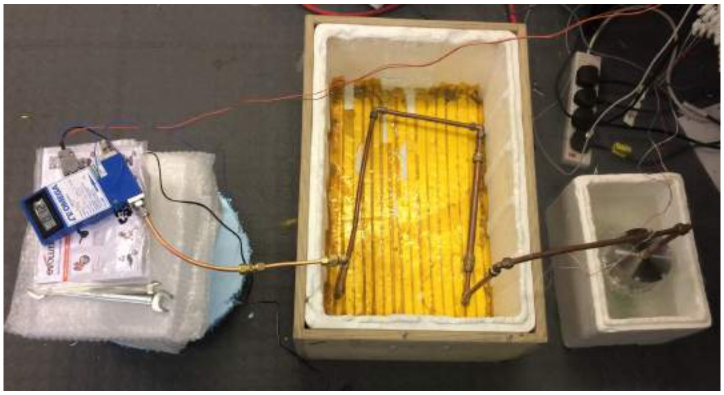

Figure 2.47: The test of the sealing integrity of the selected method. A heater was placed underneath the glass to produce more nitrogen bubbles. The liquid nitrogen level was taken above the flange to ensure the leak-tightness of the indium seal. Before entering the flow-meter the piping was taken through a heat exchanger to bring the gas to room temperature.

difficult. The repeatability of the sealing was key to achieve the objectives of the measurement platform. The material selection of the isolation vessel was the next aspect to consider. According to Weisend and based on several case studies, generally the following materials are suitable at cryogenic temperatures [114]:

- Austenitic stainless steels
- Aluminium Alloys
- Copper
- Brass
- Fibre reinforces plastics (G-10, G-11)
- Invar
- Indium
- Kapton/Mylar
- Quarts

Of the materials above Quartz and fibre reinforced plastics are the only options that do not lend to eddy current losses. The primary objective of making the item from one piece was not possible with quartz as it would need to be blown into the shape shown in figure 2.49b, instead; a trial was undertaken to bond the glass with adhesive which cracked due to the thermal gradient. Machining the piece from G10 was also not possible as it is an extremely abrasive material and the dust produced during machining is hazardous, this was a particular problem as the milling depth required was above 150mm. Also, sourcing the appropriate block of G10 is not easy as it is usually woven into fixed standard dimensions of rods or tubes. Instead, it was decided to trial an assembly of tufnol, a cotton reinforced fibre plastic, with similar properties to G-10 but higher moisture absorption and thermal expansion. The vessel would need to undergo fitness for purpose testing in the final machine. Previously, two G10 blocks bonded together with resin had shown to cause liquid nitrogen leaking through the crack of the resin. The new vessel was designed to minimise the number of joints to two as shown in figure 2.49a and had dovetail joints to maximise resin surface area. Two coatings were applied across the joints.

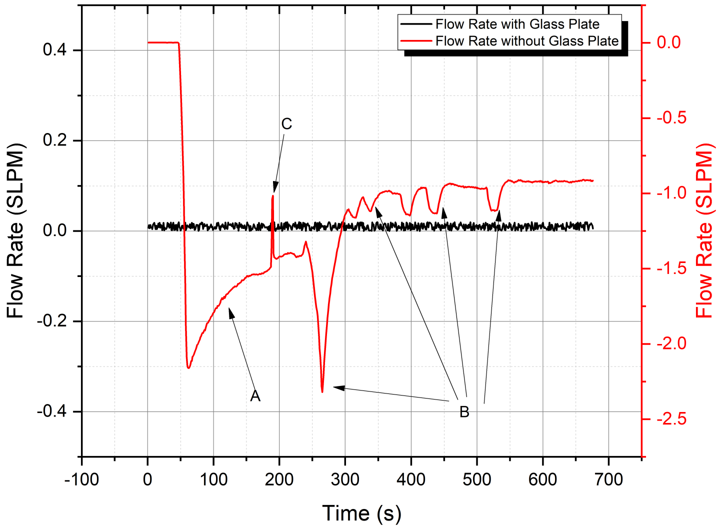

Figure 2.48: Comparison of flow rates between the glass sealing method and no seal proving the effectiveness of the new method to create a hermetic glass to metal seal for calorimetric measurements.

(a) Exploded view of the isolation vessel

(b) The assembly was completed with resin and two joints

Figure 2.49: CAD model of the isolation chamber made using tufnol. The part is item number 26 in table 2.1.

2.7 Manufacturing Process

The final design described in section 2.3 had several manufacturing challenges. The most challenging was the manufacture of the rotor assembly. The simulation of the rotor field from section 2.4, figure 2.17, shows each magnet has a pull force of up to 230kg. A significant challenge was safely bringing the four 100mm NdFeB magnets towards the steel backing disc. Several approaches used in industry and literature are the use of casings or bores to be able to get a grip on the magnet, however; the shape of our magnets would not allow these techniques and would also reduce or disturb the rotor field waveform [32] [23]. Instead, a method was investigated using resin to bury the magnets into a suitably roughened hole. A smaller 50mm magnet was first tested with a pull force of 70 kg using a wooden housing shown in figure 2.50a and 2.50b.

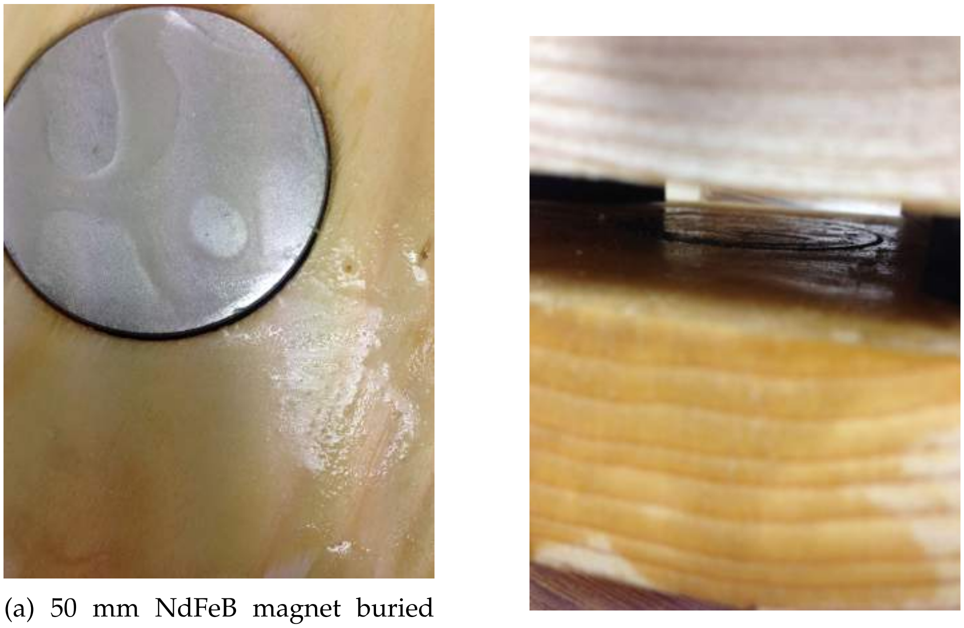

(a) 50 mm NdFeB magnet buried with resin in a 30mm deep wooden bore

(b) N-S 50mm magnet were placed together in a controlled manner

Figure 2.50: Test procedure to verify the manufacturing technique to assemble iron backing plate onto the rotor disc

Boring out a piece wood naturally creates a rough surface and is a good bonding surface, however; wood cannot be used in liquid nitrogen due to thermal contraction issues but also its weakness and warping due to moisture absorption. G10-FR4 on the other hand has a tensile strength comparable to metals and virtually zero moisture absorption. The equivalent G10-FR4 machined bores are smooth and required roughing up to create an ideal bonding surface shown in figure 2.51a and figure 2.51b.

(a) Four 101mm bores in the G10 housing for the magnets.

(b) Thin walls were machined to maintain a tight airgap.

Figure 2.51: The magnets were buried into G10-FR4 using the same resin technique shown in figure 2.50a.

After each magnet was resined into the bore a wooden cover was bolted on to prevent the magnet from lifting out. The counter-bore in figure 2.51b is to allow the minimisation of the airgap by letting the surface of the rotor disc sit flush with the shoulders on the shaft.

Once the magnets were bedded into the G10 and the resin had set it was possible to assemble the steel backing disc to sit flush with the surface of the magnet and concentrate the flux. The difficulty in this task was the necessity for central alignment and preventing the magnets from flying out in case the resin failed. An overhead crane was used to help lower the steel disc onto the rotor whilst it was held down on a 500kg table with clamps. The iron backing disc was supported with a cross made by sandwiching aluminium between two sheets of copper as shown in figure 2.52a and 2.52b. Copper has a low coefficient of friction and so would be more inclined to be pulled out once the steel disc was in place. The cross was greased with WD-40 and oil. Aluminium was used to provide the structural integrity of the cross and prevent deformation during lowering. Four locating pieces were clamped around the perimeter of the rotor disc to aid with the accurate locating of the steel disc and a further layer of resin was used to hold the disc in place, this also helped ensure a non-corrosive environment for the magnets. In the interest of minimising the air gap the bore on the G10 housing needed to be as thin as possible. Figure 2.53b shows the installation of the completed rotor discs onto the shaft. To keep costs down the G10 was used only for the structurally important part whilst nylon (white part) was used to finish the housing. Figure 2.53a shows several washers located around the periphery of the nylon housing which were used to balance the rotor to a G-3 specification.

(a)

(b)

Figure 2.52: (a) The iron backing disc supported with aluminium bars sandwiched with copper sheets was slowly lowered onto the magnets with the use of an overhead crane. (b) The iron disc placed on the surface of the magnets to concentrate the flux. A small layer of resin was used to ensure the iron disc would not move during rotation. The peripheral space available on the G10 was used to locate the iron.

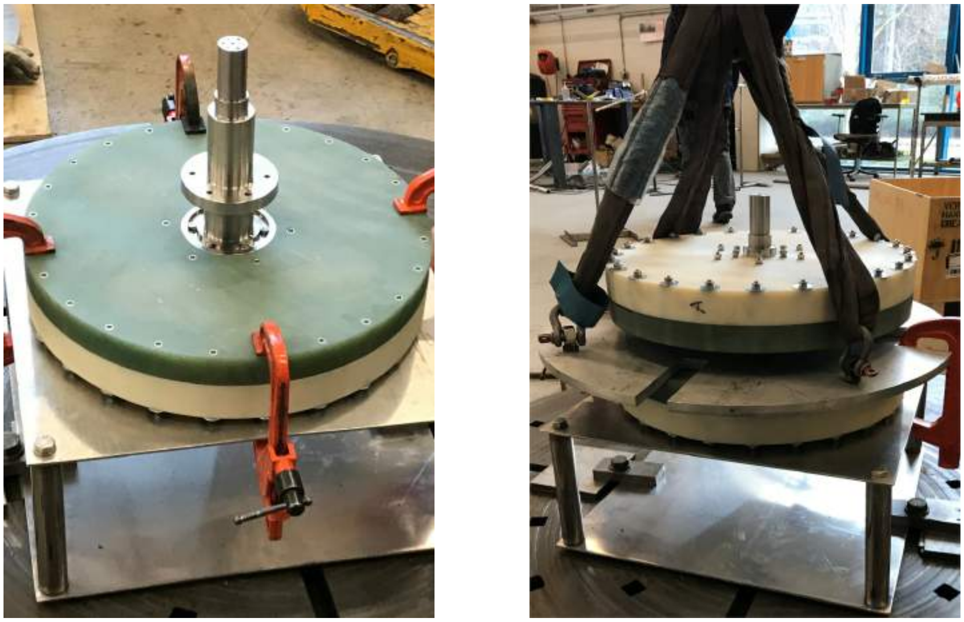

(a) The first rotor was placed and bolted onto one of the shaft shoulders. A large steel plate was used to hold the shaft down before moving the second rotor disc into position with the overhead crane.

(b) Assembly of the second rotor disc in a controlled manner. The washers on the periphery were used to balance to G-3 spec.

Figure 2.53: Two stages of completing the high risk rotor assemblies onto the shaft.

2.8 Motor Test Rig Setup

Figure 2.54 shows the laboratory set-up of the superconducting machine along with the system components.

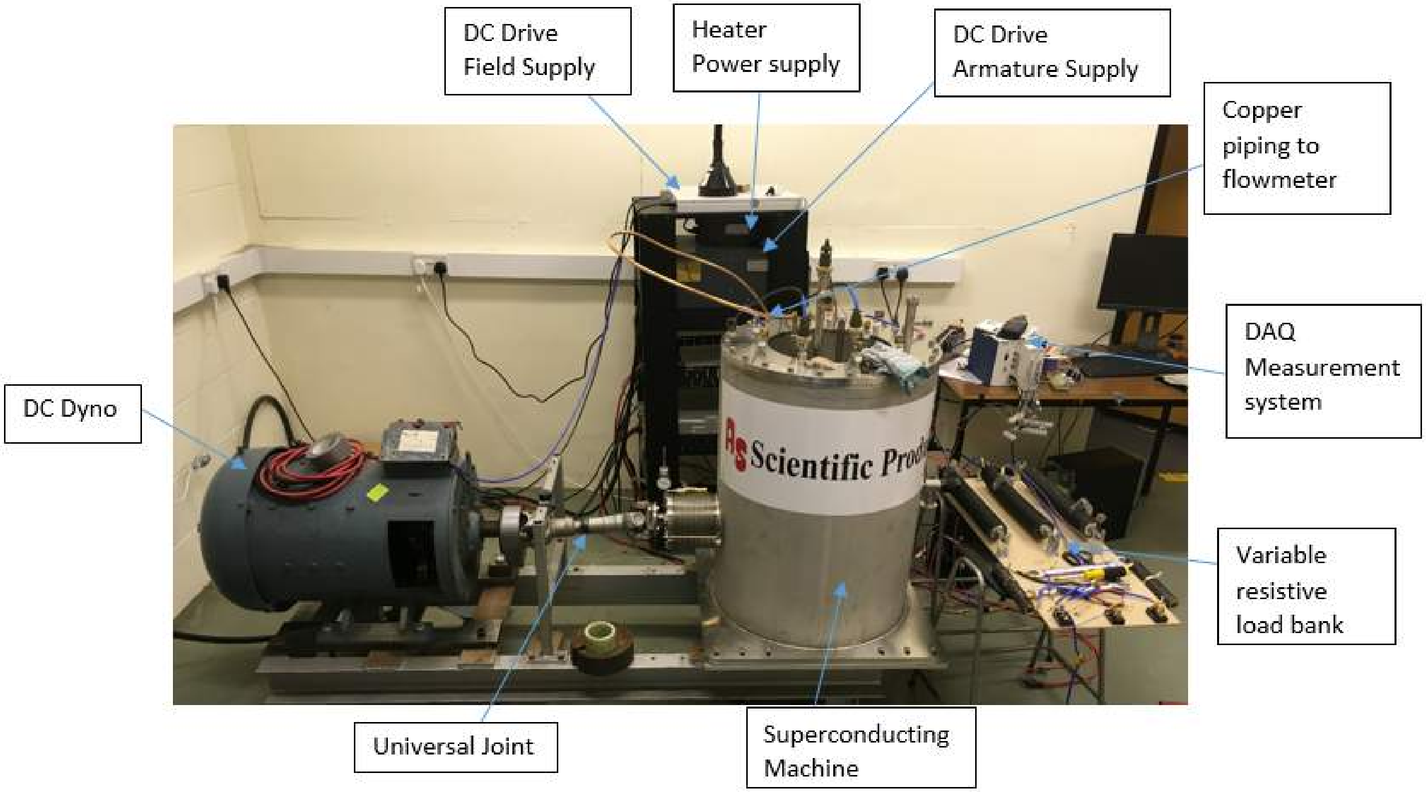

Figure 2.54: Installation of superconducting motor onto the test bed. A Universal joint is used to connect a D.C. drive to the motor. LabVIEW software is used with DAQ hardware to measure data. A resistive load bank is used to dissipate the power produced by the superconducting windings.

Chapter 3

Calorimetric Calibration & Motor Commissioning

The final machine was manufactured in early 2018 and delivered in March 2018. The machine had passed the test plan incorporating the sealing and bearing tests along with thermal tests to ensure the shaft would not freeze. Helium leak testing was completed to ensure the loss measurement chamber environment was leak-tight. The vacuum was drawn to 10^{-3} and was secured with a vacuum valve. Before being able to use the measurement platform it was necessary to test the calorimetric system and ensure it can be successfully calibrated and provide repeatable results. Additionally, characteristics of the machine such as OCV needed to be identified in order to safely test the HTS and the external circuitry connecting the high voltage system to the low voltage signal connections. Chapter 3 therefore serves as the stepping stone between the design and final results by providing important system information and verification of the design. The following items are discussed in more detail:

1. Generator setup on test rig
2. Thermal cool down and warming
3. Flowmeter calibration & background flow effects
4. Speed measurement
5. Rotor field measurement
6. Open circuit characteristic of isolated coil

3.1 Generator Setup

The manufactured cryostat was coupled with a D.C. drive and for commissioning the HTS machine was used to generate electricity and avoid programming an inverter and dealing with imbalance issues. The first step was to confirm the cool-down times and volume of liquid nitrogen required to operate the machine along with the amount of operating time this would provide. Four PT100's were used as level sensors in a 4-wire configuration for level sensing.

3.2 Cool Down & Warm up Procedure

The cool down and warm up procedure for the machine is important to maintain its reliability and longevity. The machine is designed for operation at cryogenic temperatures at which point the bearings are in optimum environmental conditions and the shaft aligns with the seals concentrically. Additionally, the method of filling the cryostat is also important. The ambient air in the cryostat has the potential to freeze within the cryostat, if this occurs within a crevice at a weld point the expansion of the moisture can cause cracking over time. Therefore, to avoid this issue a gland was inserted through the fill point at the beginning of filling to allow the nitrogen gas to push the air out. After the gland is removed and the LN_2 hosing is connected to the cryostat. The prevention of ice build up at the bottom of the cryostat allows experiments to be repeated faster as warming up does not take as long. Due to the heat sensitivity of the magnets no significant external heat was applied during the warm up process other than occasional warm air to encourage the melting of icing within the vacuum vessel.

Figure 3.1 displays the readings from the PT100 level sensors and demonstrates that the total time to cool down the cryostat is approximately two hours. The inner low and high level sensor are situated within the loss measurement chamber while the two outer low and high sensors are in the external chamber. The locations are shown in figure 2.10. The lower level sensors are the most important as they indicate the level at which the measurement chamber becomes exposed to temperatures higher than 77K.

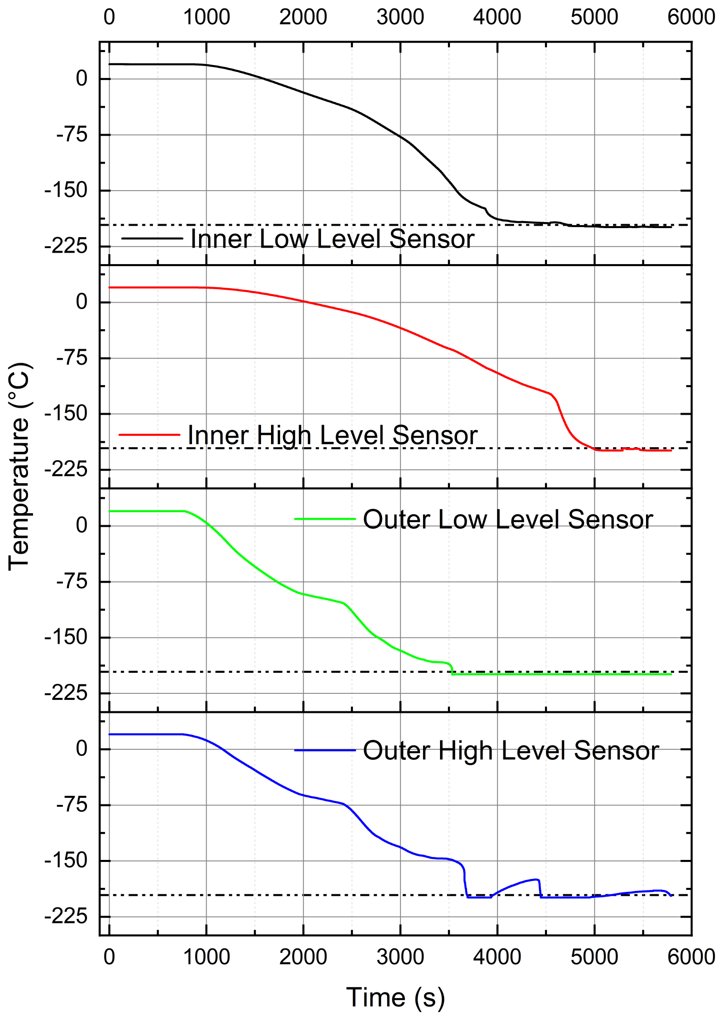

Figure 3.1: Cool-down time to operate the machine. The dashed line shows the temperature of liquid nitrogen.

3.3 Flowmeter Calibration

An Omega FMA 2710 liquid nitrogen flow meter had been designed to be used to measure the flow rate of the gas boil off within the loss measurement chamber. Liquid nitrogen expands to approximately 680 times its liquid state volume when transitioning to a gas and therefore the measurement system is extremely sensitive to local pressure variations, temperature gradients and even vibration or movement of the piping. Initially a nylon push fit with a PVC hose end was designed for use as this would have allowed flexible piping into the flow meter and a warm water bath to bring the temperature up to 20 degrees Celsius i.e. the value for which the flow meter is calibrated. However, on the first cool down it was found the the thermal conduction from the metal gland froze the plastic part rendering it impossible to get a tight fit. A rigid copper piping with compression fittings was then decided to be used with a 1/2" diameter piping reduced to 1/4" just before the flow-meter to prevent pressure build up. Instead of using a heat exchanger the copper pipe was made longer to ensure the gas would warm up as copper is an excellent thermal conductor. The icing on the pipe seemed to indicate the gas flow at the flow meter was at a suitable temperature as there was no icing that was seen when the gas flow was high. Compared with previous calorimetric setups this design is more complex due to the rotor and stator placement directly beside the loss measurement chamber [43] [123] [113]. The stator coils may produce heat which will cause bubbles to impinge on the tufnol vessel resulting in heat transfer as discussed in the design stage, section 2.5. Additionally, the spinning of the shaft will cause the rotor discs to create a continual flow of liquid nitrogen around the vessel; this was not considered at the design phase and realised as an issue during the manufacture. In order to isolate these individual contributions towards a possible unstable flow rate and assess the stability of each disturbance the calibration was initially completed separately for the rotor, stator and heater, which replicated the HTS heating.

3.3.1 Heater Power Calibration

In theory for the measurement to work the vessel must be adiabatic and have zero background flow. However, due to several unavoidable heat leaks i.e. copper terminals, radiation and conduction there is always some amount of residual thermal penetration that will result in a non-zero background flowrate at the meter as expected. During the first few experiments it was noticed the flange was a big heat leak into the measurement chamber and once both the outer chambers and the external tank were filled up a background flow of 3.5 SLPM was observed. Over several hours this continually dropped at a slow rate and was still dropping below 1.3 SLPM by the time the 355L liquid nitrogen capacity had been depleted as shown in figure 3.6. The heat load calculations from section 2.6.5, figure 2.42, estimated a heat load 4.06W implying a minimum back ground flow of 1.05 SLPM indicating the measurement chamber was close to its steady state. Figure 3.2 shows the effect the flange has on the measurement chamber. The unfrozen half of the flange proves there is a heat leak that is too great to be intercepted by the liquid nitrogen within a few hours. The first calibration was completed whilst the background flow was still dropping as liquid nitrogen stores were not sufficient. The gradient of background flow with time is taken into account during the calibration. The background flow immediately after turning the heater off is used in comparison with the flow rate immediately before turning the heater power off.

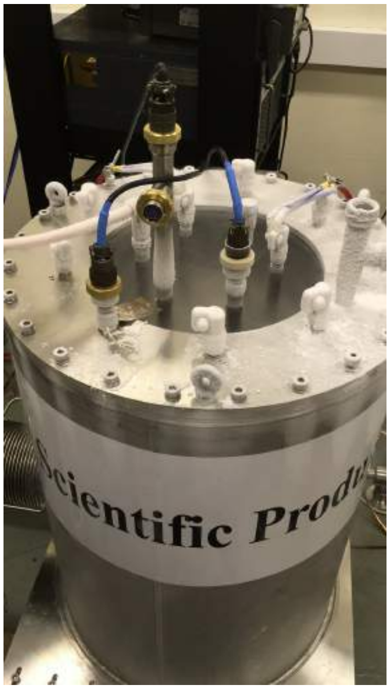

Figure 3.2: The thick flange made of stainless steel required a long time to cool down to thermal equilibrium.

The first part of the calibration to be completed was the heater power vs. flow rate. As the gas flows through the copper piping it may be subject to friction which would lower the reading at the meter, additionally; flow meter uncertainties and temperature calibrations may lead to offset errors. Applying a known value of power in the form of heat inside the chamber will allow the loss measurement flow rate to be calibrated to the flow meter and remove the potential errors described. An A1 kanthal resistance wire of 5.4 ohms was used as a heater and connected to a DC power supply. Kanthal was chosen as it has a relatively flat resistance coefficient of temperature as opposed to the more widely available tungsten filaments. The stability of Kanthal is shown in figure 3.3. The kanthal sample was cycled up to 35 Watts at room temperature to verify the stability of the heater. Due to the drop in voltage that occurs in the leads of the heater supply a pair of voltage taps were applied directly across the heater to accurately measure the heat load being deposited in the loss measurement chamber. To ensure a gas tight connection and therefore no leaks in the measurement chamber, it was necessary to compare the flow meter reading vs. various powers to the latent heat vaporisation of liquid nitrogen, which is 0.257 *W/SPLM*. Figure 3.4 shows the flow being recorded over a period of 2.5 hours. Several stages of heat power was applied via the gas-tight Detronics feedthrough and the difference in flow was recorded and plotted against the corresponding power as shown by figure 3.5. The graph proves there was no leak in the system and the loss can be accurately measured as the difference between the theoretical and measured latent heat flow is within 7%. The difference is likely caused by the length of the piping and flowmeter offsets.

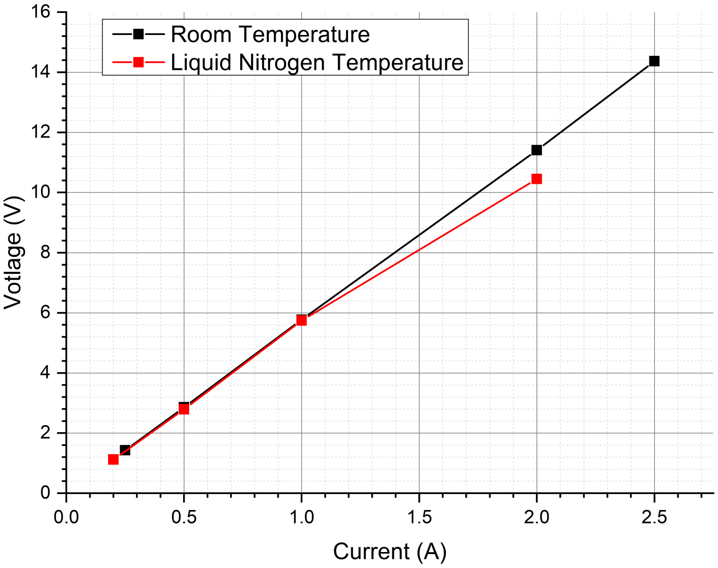

Figure 3.3: Stability of kanthal resistance. It was important to ensure flow meter measurements occurs at steady state heater powers rather than having to settle according to a time constant.

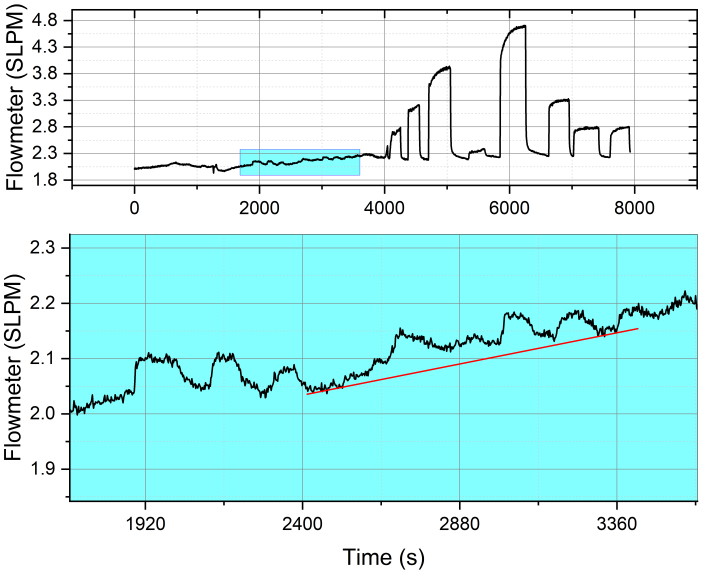

Figure 3.4: Flowrate of liquid nitrogen boil-off during the heater calibration process.

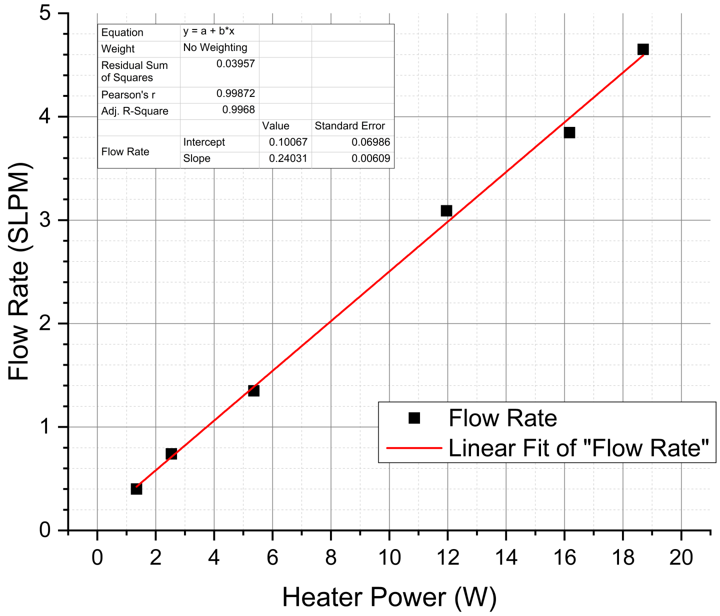

Figure 3.5: Plot of the flow rate induced by various heating powers applied to the Kanthal wire. The gradient of 0.2401 $^{SLPM}/_{W}$ is within 7% of the latent heat flow of liquid nitrogen.

3.3.2 Rotor Speed Calibration

An aspect not covered in the design phase was the affect the rotor would have on the heat load of the measurement chamber. The faces of the rotor discs are less than 3.5mm away from the isolation vessel and the resulting fluid flow caused a significant heat load. Figure 3.6 shows running the motor at 300RPM can induce a flow of 3.2 SLPM. The effect of this could be mitigated with the use of a double wall isolation vessel which has openings for LN2 to flow in from the top, although machining this is not a trivial task. Due to the abrasiveness and dangerous particulates of machining G-10 or tufnol it could not be produced in the University workshop. It has been shown that the effect of the rotor speed on the resulting flow is not a predictable event and thus it cannot be calibrated out as it depends on the nitrogen level in the outer tank which is continually changing. Ideally the rotor would be run with the measurement chamber empty to determine the induced flow allowing both magnetisation and self-field losses to be measured separately and together. Due to the need to calibrate the induced flow to the speed before all measurements, the magnetisation loss would be calibrated out and thus without a new isolation vessel it was only possible to measure the transport A.C. losses.

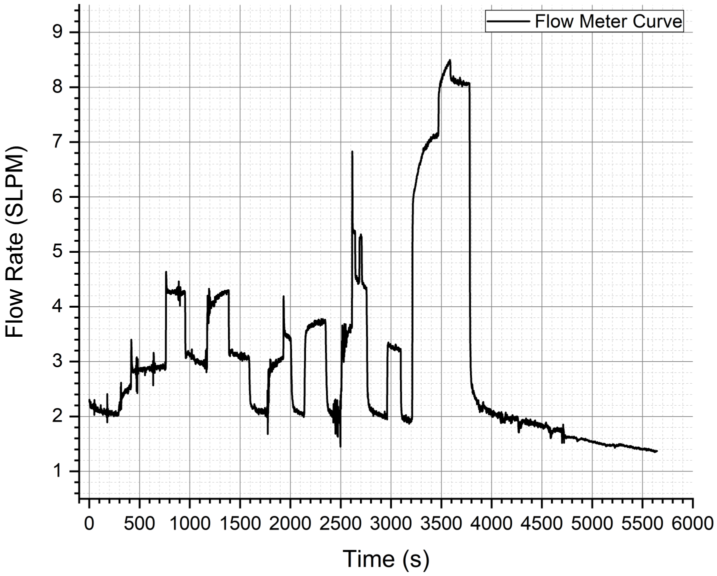

Figure 3.6: Flowrate of liquid nitrogen boil-off during the rotor calibration process. There was an uncertainty of approximately ± 0.13 SLPM.

It can also be noted from figure 3.6 that after the initial cool-down it takes more than a further 1.5 hours to get the background flow to reach its designed background flow level. The estimated heat load induced was approximated in the design phase as 4.06W which corresponds to a flow rate of 1.04 SLPM.

3.3.3 Stator Calibration

Figure 2.19 showed the tight constraints on the space available to be able to isolate the HTS coil. The closeness of the copper coils to the measurement chamber mean it is possible when rated current flows through the stator windings; heat could impact the flow rate. In section 2.5 it was shown the design of the stator had taken this aspect into consideration and care was taken to minimise its impact. Nonetheless, the stator calibration step is necessary to ascertain any effects it may have on the accuracy of the results. Before carrying out the tests in the cryostat a PT100 was attached outside to the surface of the copper coil as shown in figure 3.7a and a current was applied to determine any obvious issues. Figure 3.8 shows there was no noticeable increase in the temperature on the surface, a more detailed look into the curve displayed a small temperature increase of 0.5K. When current is applied there is a small duration of time before it settles, this is due to the resistance of the coil changing due to the heat generation and for the thermal equilibrium to be reached.

Figure 3.9a shows several stator current levels were applied to determine the flow caused. For the rated current of 20A, figure 3.9b shows there there is a flow of 0.06 SLPM caused inside the measurement chamber which equated to a +0.2W standard error which will take into account all other levels of current. At maximum flow the percentage error is +0.5%. This error can be removed once the copper coils are substituted with HTS coils as there will be an increased clearance.

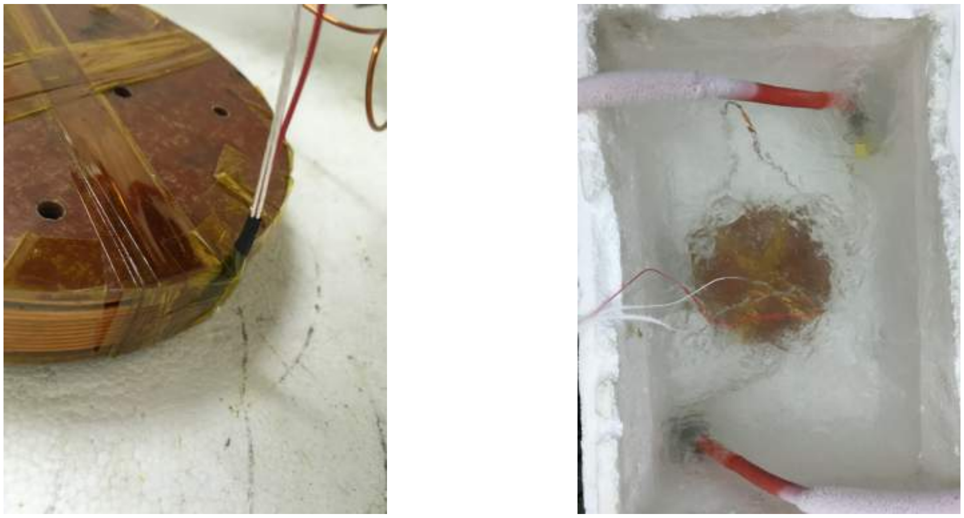

(a) PT100 attached to surface of copper coil.

(b) Bubbles of N_2 gas when current is applied.

Figure 3.7: A copper coil was tested outside of the machine before detailed testing to identify any obvious potential issue.

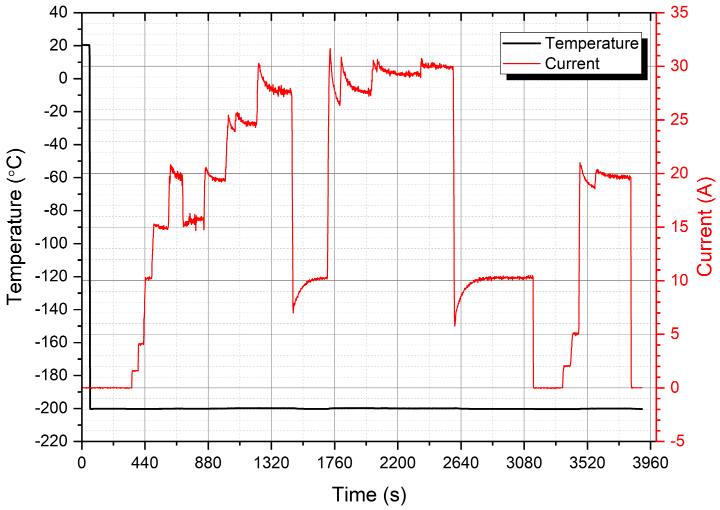

Figure 3.8: Coil surface temperature data.

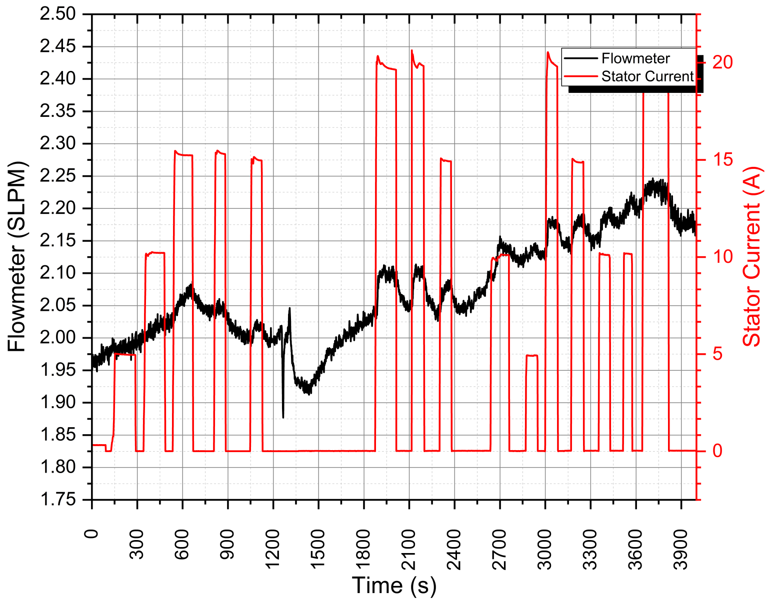

(a)

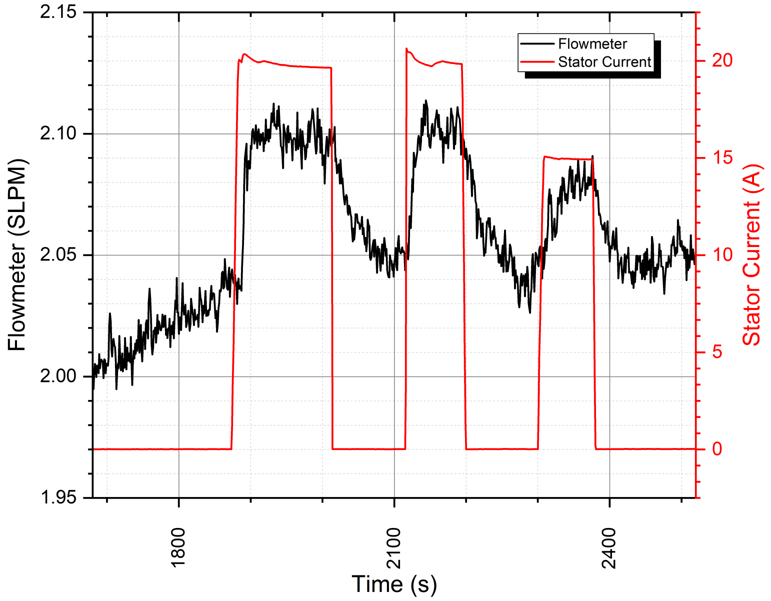

(b)

Figure 3.9: (a) Stator calibration results. Various currents were applied to the two coils adjacent to the measurement chamber (b) Close up of (a) between 1800s and 2400s.

3.3.4 Copper Terminal Calibration

The rated current of the stator windings was designed at 20A RMS and thus in a balanced operation the HTS would be expected to carry the current. Another source of heat load into the measurement chamber are the two copper current terminals. The impact of the heat source was determined by shorting the two current terminals inside the measurement chamber with a short piece of HTS and applying a D.C. current following cool down. Figure 3.10 shows the effect the terminals have on the flow rate. It may be seen that a large current of 100A creates a large flow of liquid nitrogen, the right figure displays the corresponding power. For the different current levels applied the contact resistance was calculated to ensure the measurements were logical. The figure on the right can be used to find a consistent contact resistance of approximately 0.00033 Ohms. The contact resistance varied depending on the type of coil used as the soldering technique was different. For the DPC, contact resistance was found to be negligible. In the measurements the flow rate is calibrated to take the terminal power load into account.

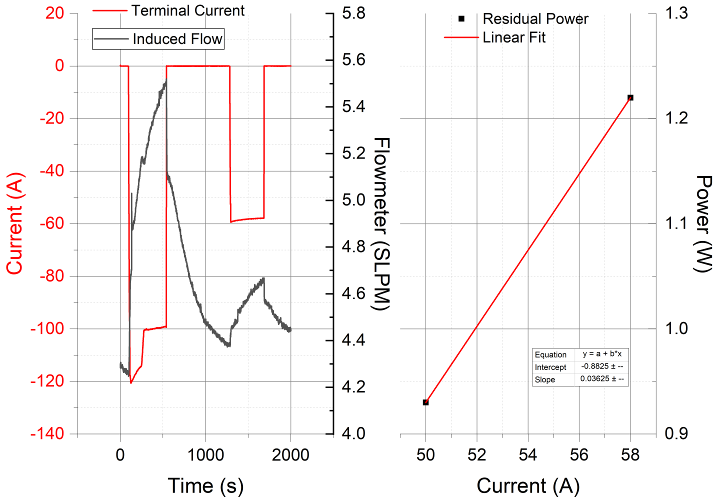

Figure 3.10: Current terminal induced background flow calibration. A consistent boil-off corresponding to a contact resistance of 0.00033 Ohms was found.

3.4 Speed Measurement

The HTS machine is coupled to the D.C. drive with a double cardan or universal joint. There was more misalignment than usually permitted for rigid coupling or semi-flexible coupling and this could not be adjusted adequately enough before testing. The double cardan joint was a component freely available and the design of the machine was therefore based on this coupling. It permits the cancellation of sinusoidal speed variations that is the case with normal Hooke joints [3].

In order to measure the speed, a small rectangular N52 NdFeB magnet was placed on the input shaft whilst a TSH 481 hall effect sensor was placed on the stand in close proximity to the magnet. The peaks in the output voltage from the hall sensor were acquired with the NI cDAQ system. A program was written to sample data at 300Hz, well above Shannon's minimum sampling rate theorem. A threshold detector set at 4.195V was used to count the number of peaks and this was translated into an RPM value. The program was verified with the manual processing of the signal shown in fig 3.11 and with the use of a non contact laser tachometer.

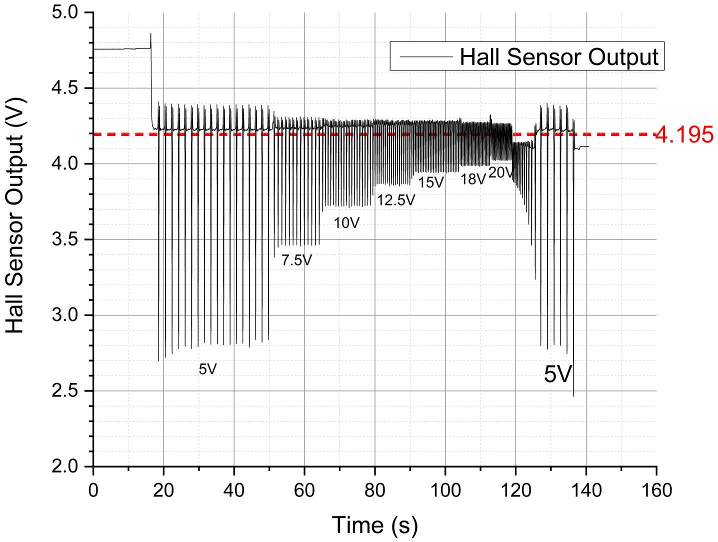

Figure 3.11: Tachometer voltage output.

The no-load speed of the D.C. machine was chosen to test the tachometer. It was uncoupled to prevent untimely wear and tear of the machine as it was not cooled down. The speed of the D.C. machine is directly proportional to the armature voltage. At several stages of the test the armature voltage was varied between 5V and 20V, each voltage change is indicated by the change in amplitude and frequency of the measured signal and are marked on figure 3.11. The maximum measurable speed is limited by the hall effect sensor's maximum switching frequency and rise time. As the speed is increased the voltage peaks drop away.

Table 3.1: Speed table generated from the speed measurement method and tested accurate with a laser gun.

Armature Voltage (V)	Peak Voltage Change	Measured RPM
5	1.53	30.45
7.5	0.82	55.2
10	0.62	80.6
12.5	0.42	100.5
15	0.32	126.5
17.5	0.27	150
20	0.245	177

Table 3.1 shows the detectable voltage change which sets the NI program threshold value and the associated RPM. The no load speed characteristic of the D.C. drive is shown in figure 3.12, the speed gradient is 9.6 RPM/V. The intercept shows there is clearly an error in this method of measuring the speed of $\pm$ 20 RPM which is a 4% error at rated speed. The laser tachometer was also used to verify these results.

To maximise the operating speed of the rotor it was balanced to a G3 specification with the use of additional washer weights on the periphery which may be seen in figure 2.53b. Despite this the rotor could not be sped to above 500 RPM as the flooding of the outer chamber with liquid nitrogen resulted in a high drag and rotor induced flow in the loss measurement chamber. Thus, the speed commissioning of the motor resulted in a rated speed of 500 RPM, 1000 less than the design speed.

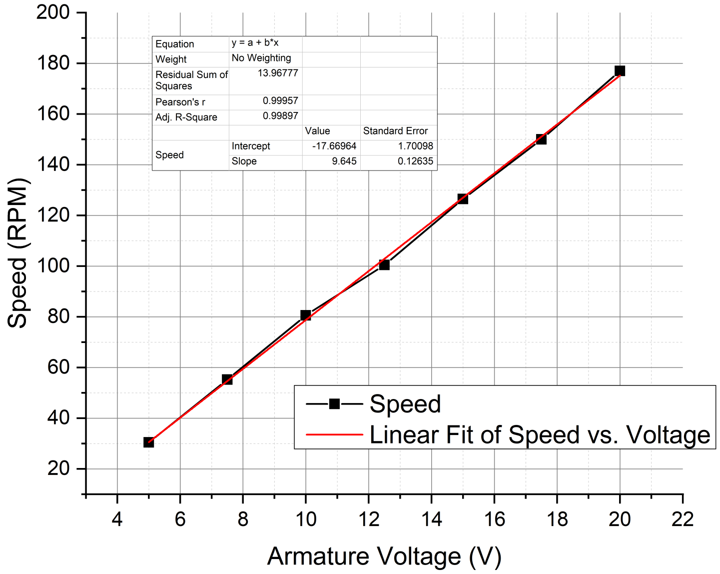

Figure 3.12: Tachometer Voltage Output

3.5 Rotor Field Measurement

During the manufacturing of the rotor, described in section 2.7, there was some heating around the magnets to remove some epoxy resin, which may have partially demagnetised them. Additionally, during the first installation tests, external heaters were directed into the cryostat to speed the process and it was later found the surface temperature of the rotor discs had reached 50°C which is a sixth of their Curie temperatures. For these reasons and to compare the manufactured rotor field to the simulated equivalent, the fields were measured as a function of the rotor radii. An Arepoc HHP-NP hall sensor capable of being used at cryogenic temperatures with a sensitivity of 83.1$^{mV}/_{T}$ and error of less than 1.2% was employed for this purpose. The hall sensor was placed along different radii along the rotor field. The inner, mid and outer radii measurements are shown in figure 3.13.

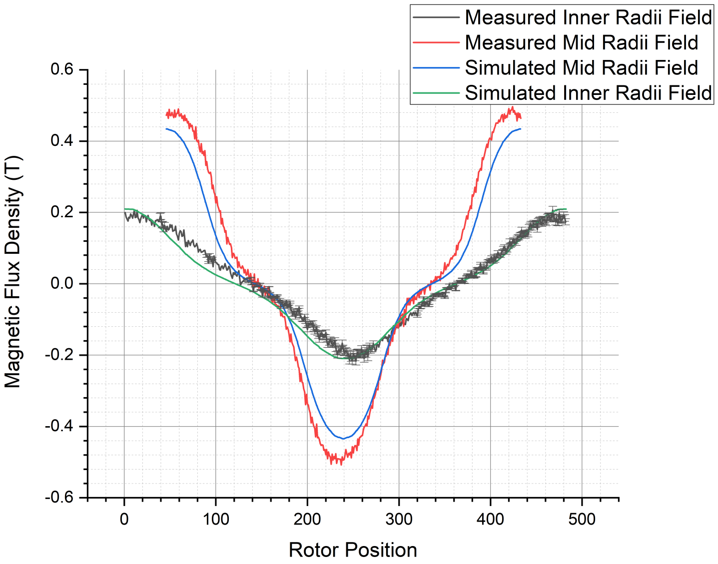

Figure 3.13: Measured rotor field using a hall sensor agrees generally well with the designed rotor. An improved peak strength is noted in the built rotor which is attributed to the slightly higher magnetisation of the magnets compared with the simulation according to the manufacturer B-H curve.

3.6 Open Circuit Characteristic

Since the HTS is ceramic it is very easily damaged mechanically. Preparing the samples takes several days and it was important to avoid over powering the samples. A step in achieving this was to determine the open circuit characteristic of the HTS coil within the machine. The first time this experiment was run a copper coil substitute was placed in the loss measurement chamber. Both the HTS coil and the copper coil were wound to as similar parameters as possible such as inductance and total overall size although it was unavoidable to have a larger equivalent copper coil as seen in figure 3.14. The thicker copper coil was exposed to a greater magnetic field than the HTS coils would be and so its generated voltage would be greater. However, this serves as an overestimate for the voltage that will be generated in the HTS coil and therefore allows a safer operation of the superconducting machine. The D.C. field winding was energised with full excitation at 340V and 0.6A. The armature voltage was varied between 5 and 92.5V which correspond to a speed between 0 and 300RPM.

Only one coil was connected to the DAQ system so the generated voltage will be approximately double of the measured value. Both coils were not connected as the DAQ system could only measure between -10V and +10V. Figure 3.15 shows the voltage waveform induced within the copper coil for three different speeds. Clearly there are harmonics in the waveform affecting the peak quality, this is due to the rotor field having a momentary decrease in its B-field resulting in less flux linkage.

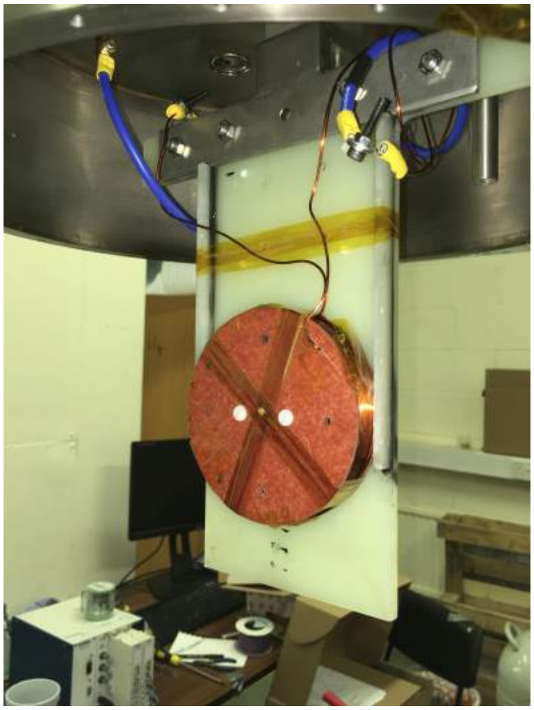

Figure 3.14: Copper coil substitute to determine open circuit characteristic of generator. Nylon bolts weres used to prevent magnetic shorting.

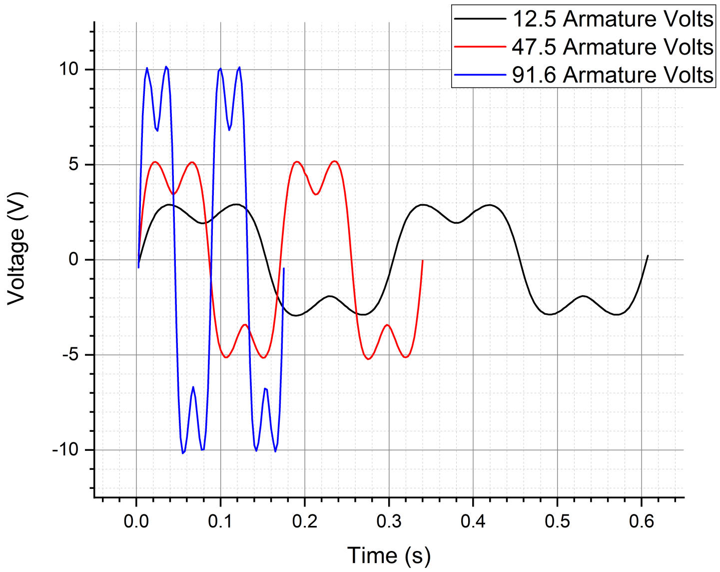

Figure 3.15: Generated voltage waveform at different speeds. Double peak is due to harmonics existing within the rotor field. The maximum measurable voltage with the DAQ system was ±10V, for higher generated volage the OCC curve shown in figure 3.16 was used.

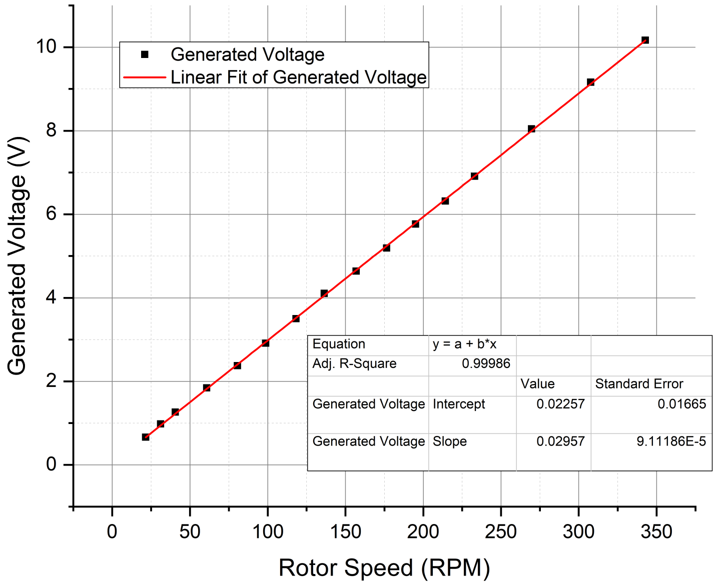

Figure 3.16: OCC curve showing a speed constant of 0.02957. It is expected to be slightly lower in the case of a HTS coil.

Chapter 4

Measuring A.C. Losses of 2G HTS Coils

Following the successful calibration of the measurement chamber and commissioning of the test platform, it was possible to consider measuring the A.C. loss of superconducting coils within a motor environment. The purpose of building the loss measurement platform was to enable the testing of various superconducting technologies and to characterise their performance in a machine environment. Whilst there are several techniques that can be explored there are two that have been shown in self-field and external fields to reduce A.C. losses by between 10% and 30%, namely striated CCs (Coated Conductors) and Roebel cables. In this chapter the loss of both is explored and compared with a standard way of manufacturing a HTS coil. An electrical method is used to measure the losses for the striated coil as the machine had not been manufactured whilst the Roebel cable coil is tested inside the motor loss measurement platform. The results of the loss measurement are capped by the maximum LN_2 capacity of 355L. 265L were used to cool down the cryostat to become operational and thus only 90L remained to run the experiments. Due to the rotor running in liquid nitrogen the outer tank required frequent filling along with the outer flange which was directly exposed to the ambient temperature. However, this chapter serves to show the novel results that can be gained from the loss measurement platform developed and that it is operationally sound along with new results for the superconducting community to consider.

4.1 Preparation of 2G HTS Coil

20m of 2G HTS Superpower tape with a minimum I_c of 118A was prepared for testing. The critical current was first measured using an 8V, 180A TDK Lambda DC current supply with data acquisition completed using the National Instrument platform. The tape was supplied naked i.e. no insulation and therefore needed some electrical isolation to prevent turn to turn current sharing. Additionally, the insulation protects the HTS from oxidation caused by oils and dirt in the environment. Normally manufacturers can supply coils with kapton tape wrap insulation but this is not ideal as, were the coils to be epoxy resined, it has been shown the gaps caused by the method of insulation allows resin to bind to the HTS and exert mechanical stress, thereby causing a critical current degradation [123]. Instead, a special heat shrink tube with an extremely thin wall thickness of 0.0127mm was used to provide overlapping insulation. Each meter of the tape was individually insulated with a temperature below 200 degrees Celsius and took one week to complete.

First a 15cm sample of the tape was tested but it failed and burnt out due to incorrect setup with the DAQ cards, thus a lower voltage was being displayed than occuring. A second 15cm was loaded onto the test plate with voltage taps placed apart by 9cm as shown in figure 4.1. The accepted critical criterion within the research community of $1\mu V/cm$ was used to determine the critical current. Three tests were run to ensure repeatability but also to prevent a burnout each test was run to a progressively higher voltage. The resulting I_c was measured at 128A as shown in figure 4.2. Once wound as a coil the I_c will deteriorate due to the self-field but also the bending radii which increases the stress.

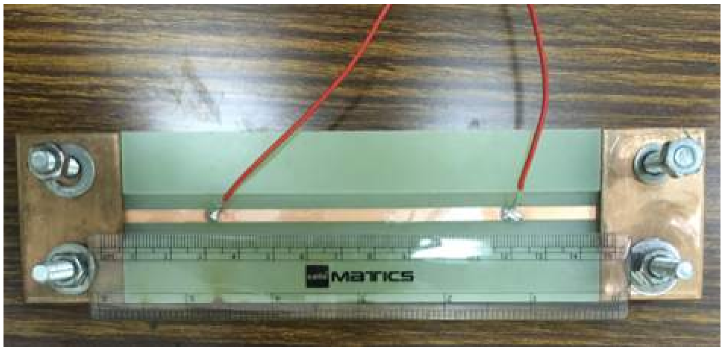

Figure 4.1: Sample holder for I_c test. Voltage taps are spaced 9.5cm apart.

It is well known that HTS, being a ceramic material, is very fragile and prone to damage with either too much heat or mechanical stress. Therefore, whilst soldering the temperature should be kept below 200 °C and care must be taken not to bend the tape beyond a radii of 20mm. A double pancake coil requires a HTS sample to be split onto two spools and the winding to commence from the middle of the length. The double pancake can be made either by traversing the inner most turn to span across two layers or halving the tape and making an electrical connection with the use of a 12mm strip of HTS on the inner radii. The latter introduces a solder resistance which may affect the tape and the loss measurements and thus was not selected [54]. The complicated winding compounded with the fragility of the tape required the design and manufacture of a winding apparatus that would be able to support both spools and accommodate winding without risking any stresses. The design and subsequently manufactured apparatus is shown in figure 4.3a and 4.3b, which allows two spools to be suspended with one moving relative to the other in a controlled manner. The purpose of this work was to gain experience in handling the HTS material and winding a coil. The first coil manufactured did have considerable damage but the process was improved, such as soldering technique, and the subsequent coils performed well.

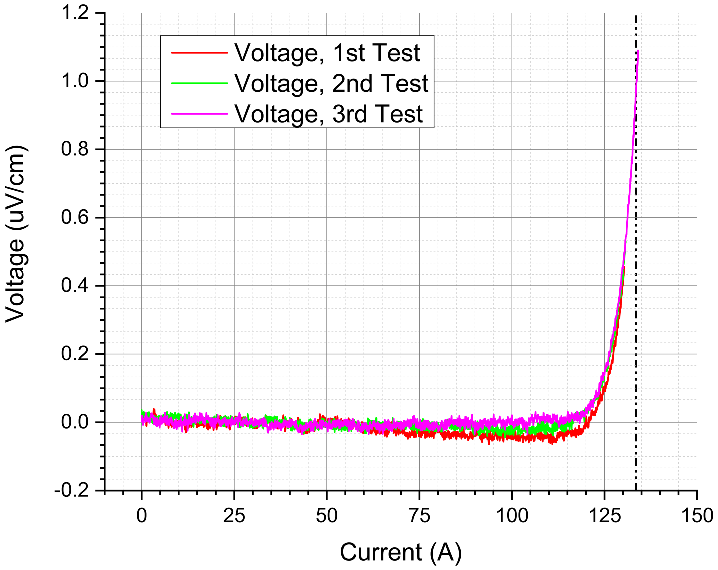

Figure 4.2: I_c curve of Superpower sample shown in figure 4.1 showing a critical current of 128A.

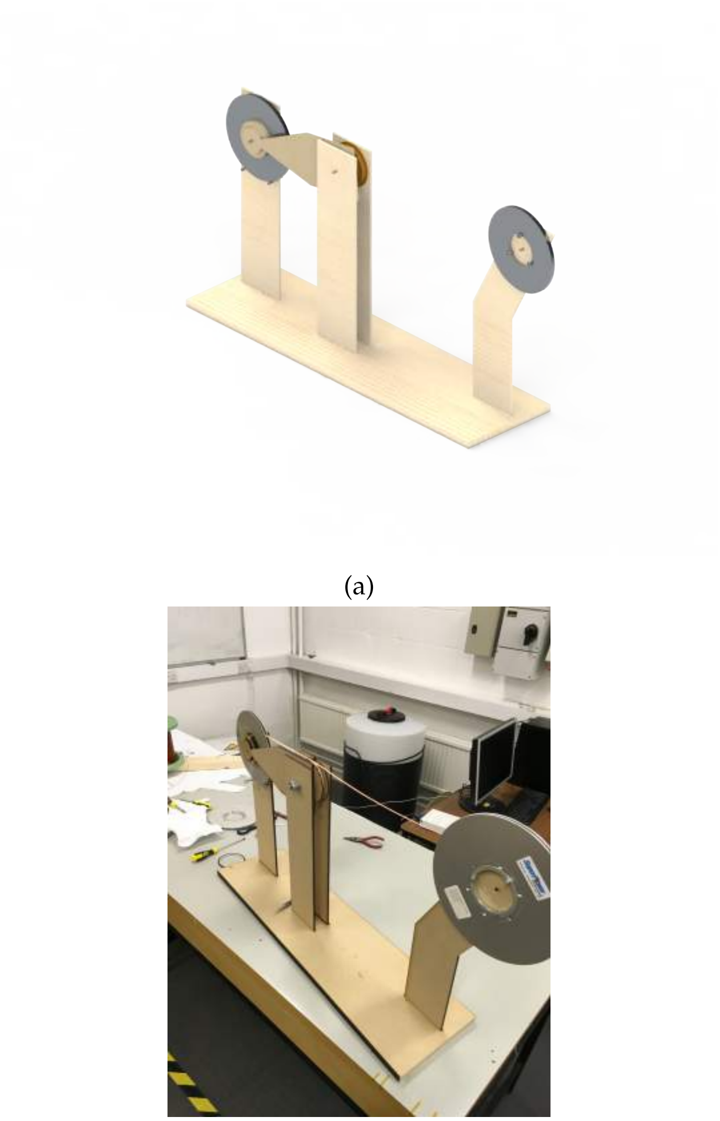

(a)

(b)

Figure 4.3: (a) CAD Model of the winding apparatus (b) The apparatus was manufactured using plywood laser cut into several sections and then glued together with araldite. A slotted pin was used to provide constrained rotation of one spool.

4.2 Striated Superconductor Loss Measurement

It has been shown in section 1.2 that the A.C. loss is proportional to the width of the superconducting tape. A method of lowering the A.C. loss is to reduce the width of the tape 4.2.

The electric method described in section 1.3.3 was used to measure the total A.C. loss of a novel striated 2.65m sample of Superpower tape which was compared with a standard manufacture Superpower tape for various frequencies. The details and pictures of the coil are shown below in figure 4.5 whilst the two I_c curves for the coils are displyed in figure 4.4.

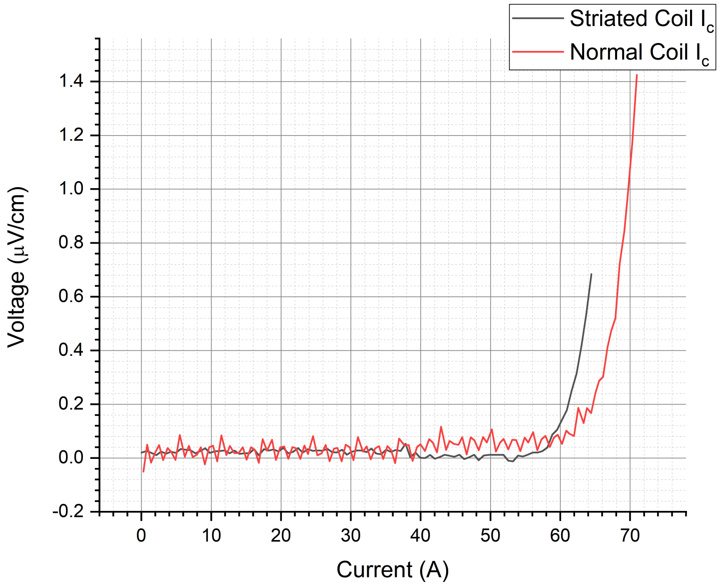

Figure 4.4: I_c curve comparison of striated coil sample and standard Superpower tape. A reduction of 8.5% is apparent due to the scribing of superconducting material.

The reduction of I_c is the trade-off in this manner of reducing the A.C. losses due to less superconducting material remaining after the etching process, therefore; the application is important in justifying the lower A.C. loss. Generally, due to the thermodynamic penalty of cooling, the reductions in I_c of most A.C. loss reduction techniques is acceptable. The two coils had their total self-field A.C. losses measured at frequencies of 70, 120, 170, 220 & 300Hz to identify accuracy in the measurement set-up. Figure 4.6a displays that for currents above 25A peak, the results agree within

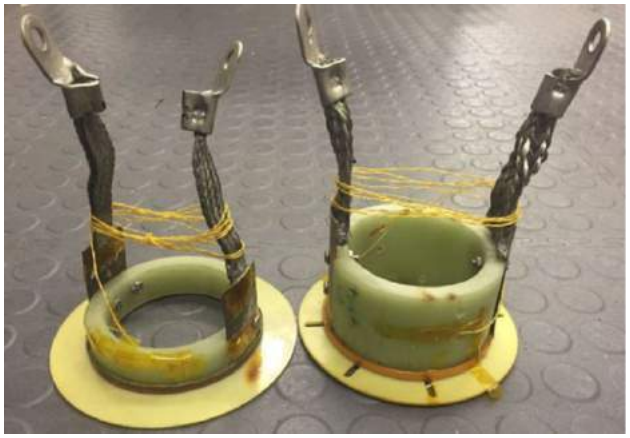

Figure 4.5: Two coils manufactured with striated coil on the left and standard reference coil on the right.

7%, generally it was noted that the errors were larger (above 10%) for lower currents and these were not used in the analysis. It is expected the source of error is due the larger percentage noise would make up of the signal. In terms of total A.C. losses the multi-filament wire actually had a higher loss; which was not expected. Superpower used a new chemical etching process to achieve striation which may have increased the amount of coupling and 'superconducting bridges' that would nullify the major benefits of isolating the superconducting material. However, when taking into account the normalised current, due to the difference in I_c, figure 4.6b reflects there is an overall reduction in A.C. loss for the multi-filament tape. The average percentage difference as shown by the error bar is around 20%. It must however be remembered this difference must be offset against the need to incorporate a larger turn number for the windings to account for the 8.5% drop in I_c which would result in an increase in the length of wire needed reducing the net benefit of A.C. loss reduction in terms of equivalent amp-turns to around 11%.

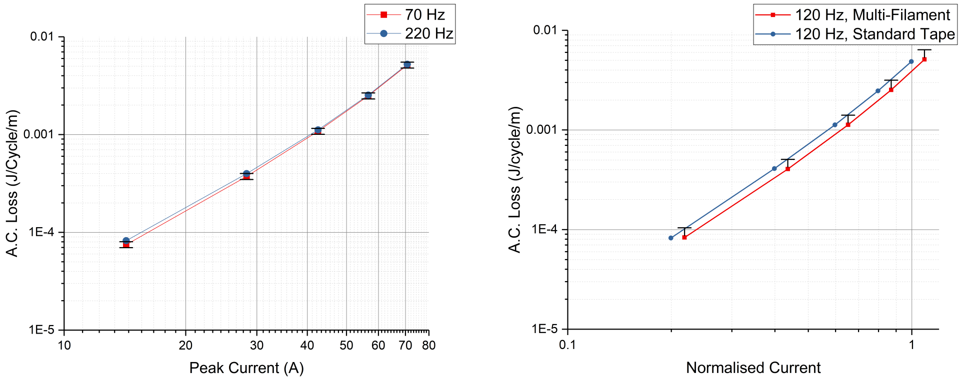

(a) Log plot of loss vs. peak current

(b) Log plot of loss vs. normalised current

Figure 4.6: Error bars of 7% on plot (a) show the accuracy of the measured data across a wide frequency range. Higher frequencies could not be measured due to the high inductive component and limitations of the power supply. The graph on the right has plus error bars of 20% to illustrate the difference.

4.3 Calorimetric Measurements

4.3.1 DPC Measurement

The first loss measurement attempt with the newly developed test rig was undertaken with a standard DPC with a transposed inner turn to avoid a resistive contact. The details of the coil are listen in table 4.1 with figure 4.8 showing the setup of the coil in the isolation chamber. A kanthal resistive wire was place in the centre of the coil to mimic the boil-off from the coil as close as possible. Two voltage taps were placed 1cm away from the copper terminals to measure the critical current. Figure 4.7 shows the I_c curves of the coil in both self-field condition outside the rotor environment and inside the machine. The self-field I_c of 76A and subsequent degradation to 55A show that the actual maximum current achievable will be similar to that used in the analytical design. Attempts were made to measure the critical current at several rotor positions but this could not be completed due to a drawback on the machine setup. The lack of a mechanism to brake the shaft results in a Lorentz force causing a movement of the shaft, thus the rotor misaligns itself and the voltage measured spikes above the $1\,^{\mu V}/_{cm}$ criterion (seen by the purple curve). The shaft was manually held steady with the use of a crowbar against a support which improved the result but the most minute movement terminated the measurements. Thus, the safest current to run the coil was found to be 30A peak but this would likely not be the maximum the coil can handle.

Table 4.1: Description of manufactured DPC coil

Coil Parameter	Value
Straight Sample I_c	140A
Self-field AT	1900
Coil ID & OD	95mm & 99.77mm
Coil Length	25m
Turns	38
HTS Type	Superpower SCS4050-AP
Insulation	Heat Shrink

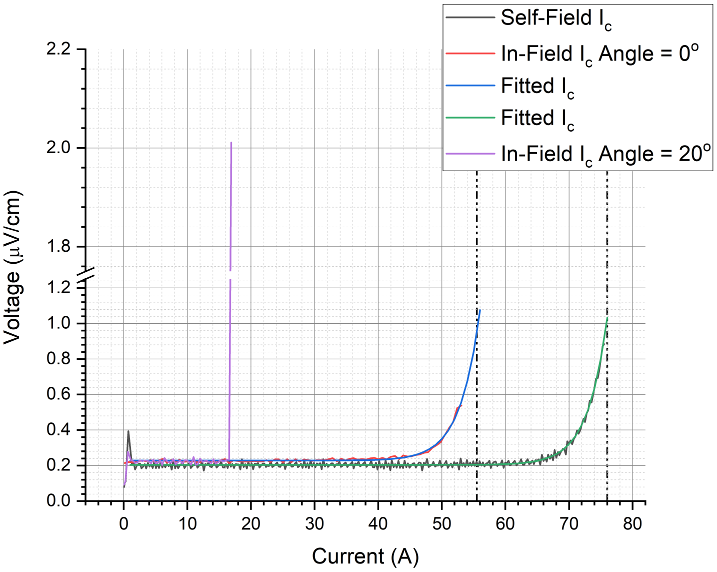

Figure 4.7: Various I_c of the 25m DPC. Self-Field I_c is 76A whilst the 0deg in-field I_c is degraded by 27% to 55.5A. It was not possible to measure the weakest in-field I_c.

It can be seen from figure 4.9 a calibration process was undertaken before measuring the loss results. This was the case for every loss measurement undertaken with the platform. There is clearly a drift in the back-

Figure 4.8: Setup of coil inside the measurement chamber before closing the cryostat. The heater location and voltage taps along with current leads can be seen.

ground flow, over a period of 4500s the background flow increased from 2.1 to 2.8 signaling a drift of $0.0093^{SLPM}/_{minute}$ which was taken into account. After the calibration the rotor was driven to the speed relating to the required electrical frequency, in this case 300 RPM resulting in a 10Hz signal. As mentioned previously, due to the unpredictable flow rate induced by the movement of the rotor around the isolation vessel it was not possible to isolate both the transport and magnetisation losses. The impact of the fluid dynamics around the isolation vessel due to the mixed state of nitrogen caused by rotation was not taken into account during the design stage. Thus, the magnetisation loss was calibrated out by running the motor up to speed and recording the flow rate to which points A and B in figure 4.9 refer. Subsequently the terminals are connected across the load bank and current is drawn, the subsequent difference in flow rate is recorded as corresponding to the transport loss (the difference between points A and B). The background flow caused due to the rotor was undertaken three times (point A,B and C) both before and after the measurement to ensure repeatability and accuracy within the limits defined in section 3.3.2.

The current was drawn at levels of 10, 15 & 30 Amps as shown in figure 4.10. The loss measurement follows the expected trend of a linear loss (on a log-log plot). A loss of $0.01\ ^{J/cycle}/_{m}$ was found for the 30A current draw

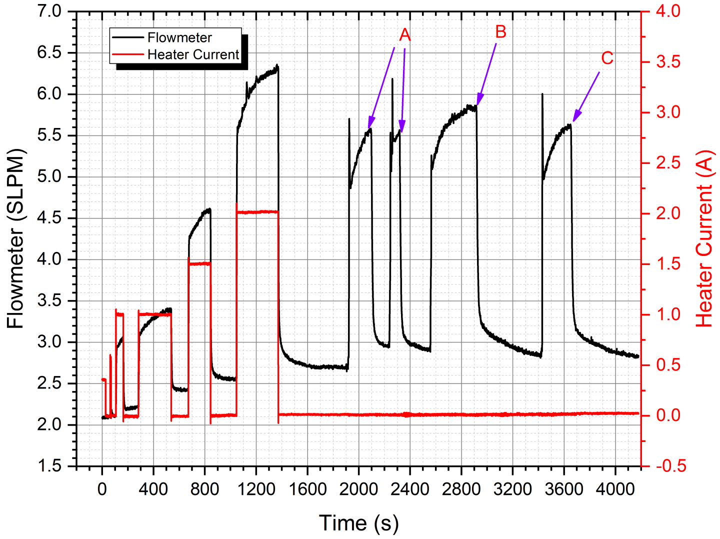

Figure 4.9: First loss measurement of a HTS coil within the machine.

which indicated a total power loss of 2.4W for a 1140AT coil. An equivalent copper coil of the same amp-turns would produce a loss of 34.2W with a packing factor worse by a 5 fold magnitude. A Comsol modelling of the double pancake was completed using a 2D axi-symmetric model and the *H*-formulation described in section 1.3. The higher current levels match very well with the simulated results, however; for lower currents there is a significant discrepancy on the orders of magnitude. An investigation into the possible causes revealed two potential causes, firstly; the current terminal background flow was re-measured to take into account the soldering of the HTS. The impact of this was not great and did not improve the results as the low currents and resistance resulted in extremely low Joule losses. However, the rotor flow uncertainty discussed in section 3.3.2 explains the discrepancy. The uncertainty of this type is not dependant on the loss measured as a percentage but rather a fixed value. During experiments, whilst it was taken care to minimise the differences in rotor speed induced flow, a variation of 0.5W, equivalent to a flow rate of 0.1285 SLPM, occurs and is unavoidable without a complete redesign and manufacture of the isolation chamber. In terms of the impact on the results, error bars in figure 4.10 reflect a minus error bar for a fixed 0.5W uncertainty and minus 0.58W accounting for the manufacturer specifications of the flow-meter. These show that the results are significantly affected at low current measurements below 25A and negligible at higher levels. Thus, the platform is verified and validated for A.C. loss measurements at high currents where the uncertainties do not make a significant percentage error. It has been shown by minimising the error, low current loss measurements can be made. For the machine application it is required the HTS carries a high current (near its critical value) so the experimental rig is still useful and has been used to measure the loss of a new type of coil at high currents in the next section.

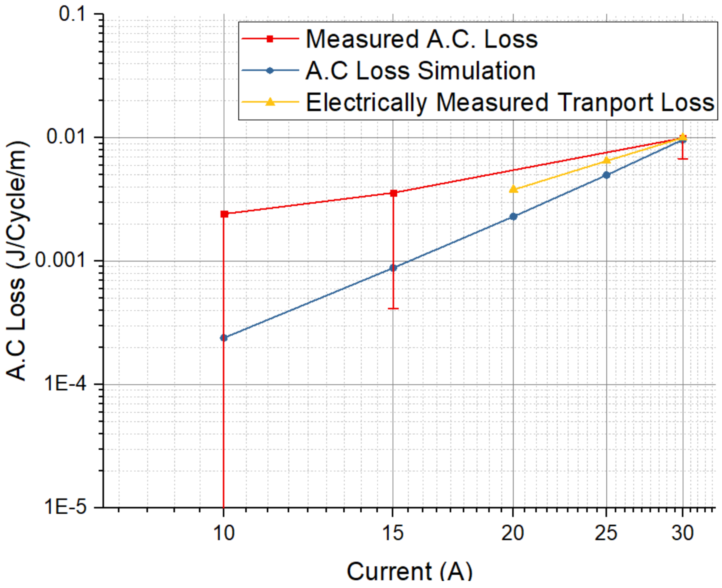

Figure 4.10: Translation of Figure 4.9 into A.C. loss data with error bars reflecting the uncertainty of rotor induced background flow.

4.3.2 Roebel Cable Coil Measurement

During the early 1900s when power applications of generators were scaling up in size the A.C. losses of conductors became a major cause of concern. Besides using Litz wire, Ludwig Roebel discovered a cabling technique on the same principles to transpose multiple conductors to form a cable which inhibits the formation of skin and proximity effects [40]. Amongst the cabling techniques proposed in the literature including CORC, Rutherford and stacks; Roebel cables are more weight efficient due to the lack of a copper core and lower losses compared with stacks owing to the better sharing of current. Additionally, the rectangular cross section of the wire and mechanical performance of the cable results in more versatile coils and increase the packing factor in machines. Using various cable geometries and ratios, past work has shown that the AC losses can be reduced by up to 30% depending on the reference comparison i.e. compared with stacks or the Norris model [51].

Jiang measured the total A.C. loss using the electrical method and found at transport to critical current ratios of greater than 0.4 the A.C. losses were up to 1.5 times lower than those of equivalent stacks [49]. Subsequently it was shown that in terms of magnetisation loss, with reference to equivalent stacks, the magnetisation loss was found to be up to 2 times lower in cases where the external field is higher than the penetration field [125]. The total A.C. loss in a Roebel cable has been touched upon in the literature showing a dominance of the transport loss for any amplitude of parallel external field whilst a small perpendicular field results in the same dominance. For useful engineering transport current ratios the transport and magnetisation loss contributions are equally comparable and impact the total A.C. loss [50]. The reduced losses in a standard Roebel cable have been shown to be even further reduced when each strand is striated similar to section 4.2 by a factor equal to the number of filaments under certain field conditions [118].

Despite the promising background literature that led to the rise of Roebel cable HTS application, until now there has been no work done on attempting to measure the A.C. losses of a Roebel coil operating inside a machine; the environment for which they were originally designed. In order to demonstrate the novelty of the machine and provide important preliminary results, a Roebel cable coil was manufactured and tested inside the loss measurement platform and compared with a standard DPC coil in this section. The coil description is given below in table 4.2.

Table 4.2: Description of manufactured Roebel cable coil

Coil Parameter	Value
Strand Configuration	5/2
Coil ID & OD	95mm & 99.325mm
Coil Length	1.8m
Turns	4.5
HTS Type	Superpower SCS12050-AP

The punching method was used to stamp a 12mm width tape into three 2mm transposed strands shown in figures 4.11a and 4.11b. A 12 tonne press was used with high precision and sharpened blades to achieve a cut that would not place stress on the superconductor, the punching machine was designed by the Robinson Research Institute [9]. Despite these provisions, figure 4.11c shows how some de-lamination can occur on the strands, most are not as visible and thus every single strand was placed onto a measurement platform and the I_c was investigated. Voltage taps were used to isolate local points of degradation and these were cut out. The final step to produce the cable was to wind each strand around one another to produce a 5mm wide fully transposed Roebel cable shown in figure 4.11d. The complexity of manufacturing these cables is a reason they have not been widely researched or developed, hand winding cable of lengths greater than a few meters is labour intensive and can take weeks. The 2 metre cable produced for this experiment took two days. The measured strand $I_c^\prime s$ are shown in figure 4.12.

The benefits of a Roebel cable coil are only realised when uniform current distribution is achieved within each strand. A common problem in the construction of a Roebel cable is to avoid the unequal contact resistances when transitioning from copper to superconductor. Figure 4.13 shows the finished coil with nomex turn to turn insulation with the red arrows on the copper terminal displaying the possible paths the current may take to reach the various strands of the cable. Several techniques have been used in the literature to over come this problem including an overflow of solder inside copper terminal blocks, soldering equal length copper strips and the use of silver foil to reduce the resistance to tolerable levels [51]. A new method was proposed for the Roebel coil tested inside the machine. As space was a limiting factor it was not possible to use the aforementioned techniques, instead; to bring the current to the same potential across the transposition length a 1G HTS foil was presoldered to a copper foil and the strands of the cable were then soldered to the 1G HTS as shown in figure 4.14.

Measuring the I_c value of the Roebel cable coil resulted in the same issues as for the double pancake coil of section 4.3.1 in that the shaft would move once a certain current was reached and therefore the $1{\mu V}/{cm}$ criterion could not be measured as the changing magnetic field resulted in the disorientation of the rotor field. Instead, for the case of the Roebel coil the curve had reached the exponential portion and could be extrapolated to estimate an I_c of 164A as shown by figure 4.15. The effectiveness of the 1G termination method is better seen when observing the log-log plot of the coil, which proved no significant uneven distribution. Whilst the degradation of the I_c was expected due to the rotor field increasing the flux penetration into the superconductor, the 10.1% drop in storage was not expected as the coil was kept moisture free using some dessicant; the coil was stored for 8 months. Upon further inspection it was found that during the manufacture of the coil some of the superconductor became exposed to the atmosphere and during drying after the post-manufacture testing the oxidation may have impacted the I_c.

Figure 4.16 displays the loss measurement compared with DPC. It may be seen, depending on the metric of comparison that an approximate 20% reduction in the loss is achievable per volume. The amp-turn metric is not as good but this was due to the inability to drive the coil to its full I_c which is where the cable would perform better. Nevertheless, it has been shown that Roebel cable coils could provide a useful loss mitigation technique if long lengths can be manufactured reliably and with uniform properties and it has also been demonstrated there is significant potential for these coils to be used as machine windings to reduce A.C. losses.

(a) 12mm tape punching machine with 20 tonne of force.

(b) The punched tapes were then separated onto three reels.

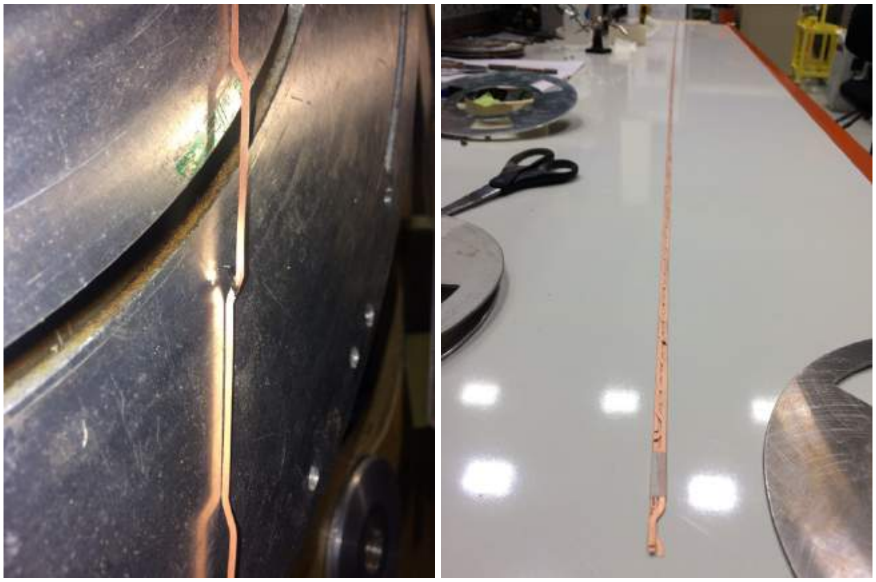

(c) Each strand was tested for its I_c along its entire length. Obvious defects were noted due to an imperfect manufacturing process.

(d) 5/2 roebel cable was hand wound with a 90mm transposition. Total cable length was 2m wound into 4.5 turns.

Figure 4.11: Various stages of manufacturing the roebel cable.

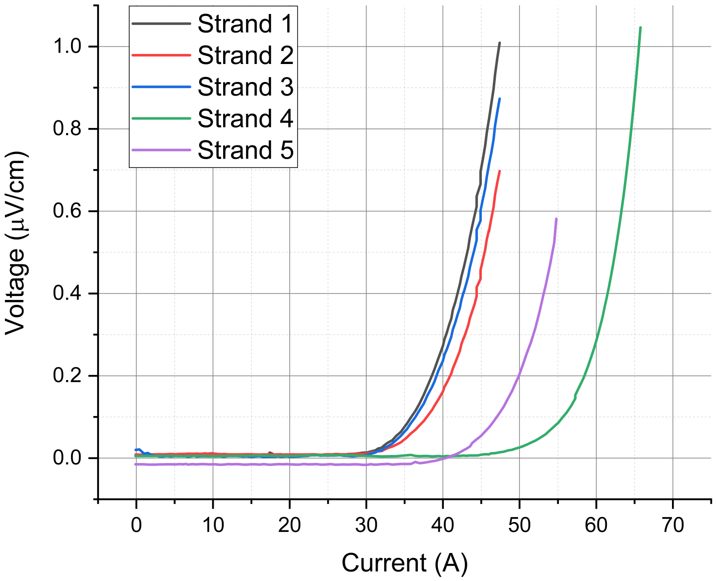

Figure 4.12: Individual strand I_c values. The large variation of two of the strands was an unexpected result. It could be attributed to the I_c dependence on the width position for a 12mm superconductor and a degradation of the other strands [65].

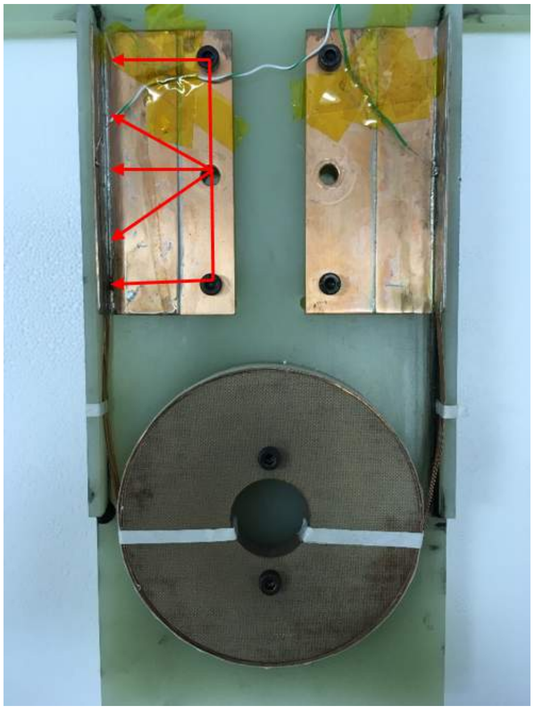

Figure 4.13: Double pancake coil consisting of 5/2 strand 2G HTS with 4.5 turns. The red arrows show the various paths the current has to travel to the Roebel cable.

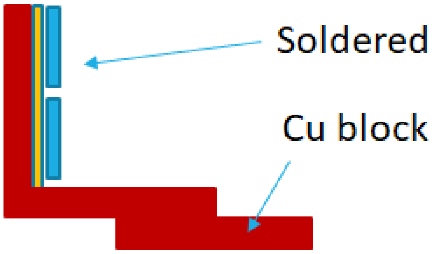

Figure 4.14: End termination method used to provide an equal contact resistance.

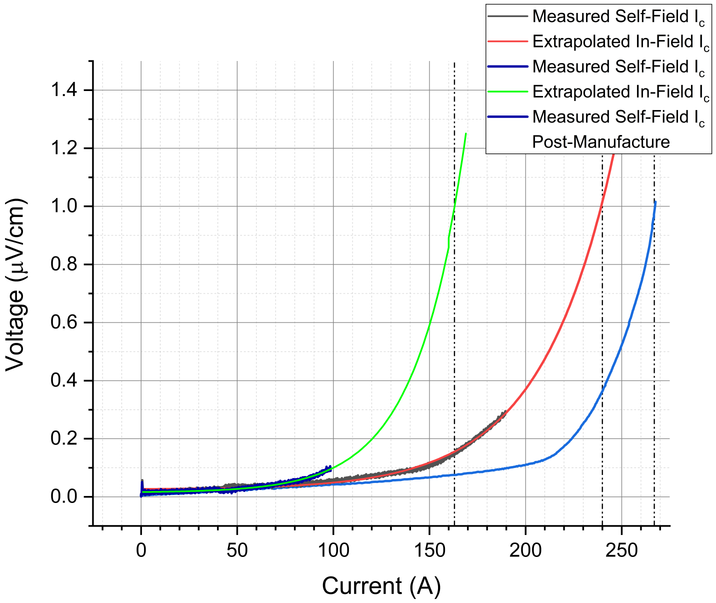

Figure 4.15: I_c measurements of the Roebel cable coil. Immediately after manufacture the I_c was 267A but during the storage period of 10 months there was a degradation of 10.1%. The measured in-field I_c was estimated to degrade by 31.67% to 164A. The full I_c could not be measured as the slightest movement in the shaft due to current injection spiked the voltage monitor and stopped any measurement, thus results were extrapolated.

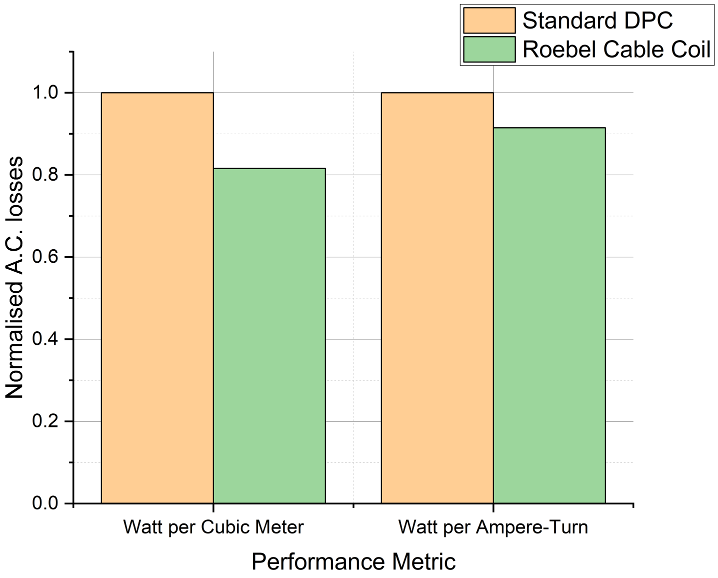

Figure 4.16: A.C. loss comparison between the standard DPC winding and the Roebel coil winding showing improvements at low current loading levels.

Chapter 5

Aircraft Baseline Target for A.C. losses in Superconducting Motors

During 2017 several important stakeholders within the aviation industry expressed genuine interest and intent on developing electrical aircraft, including NASA, Boeing, GE, Wright Electric and EasyJet. The announcement by EasyJet to develop a fully electric battery powered aircraft in partnership with Wright Electric for flights that cover most of their operations under two hours poses an opportunity for superconductors.

The real issues and interests of industry leads to the question of a baseline target that would enable superconducting technologies to be considered technically feasible compared with other design options. Whilst several studies have looked into possible future configurations, power densities and loss estimates; there is less information on the nearer term aims of the aviation industry (shown in section 5.1) and whether or not HTS can fulfil these, particularly in terms of maximum allowable A.C. losses [18] [20] [21] [19]. Whilst there are several fuelling techniques that are available for electrical aircraft including nuclear, bio-fuel and hydrogen; safety and operational constraints make hybrid or battery aircraft a more nearer term reality [39]. Whilst NASA have studied future next generation aircraft harnessing technologies such as TiAl materials, CMC HPT vanes and others; their phase 1 SUGAR study explicitly states a need to study hybrid electric propulsion for other aircraft configurations where the aerodynamic efficiency is not as ambitious to determine whether the technology can bring reasonable benefits sooner [18] [14].

Whilst the previous chapters of the thesis considered YBCO in the loss measurements, their losses within external fields compared to other options precludes them from use in stators where the majority of the loss occurs. In this chapter an A.C. loss model for BSCCO is used as it has been shown to have a lower loss than YBCO due to its wire form and is more suitable in terms of engineering practicalities (mechanical characteristics, manufacturability etc.) in stator windings [57].

Thus, Chapter 6 aims to develop a core baseline target that superconductors need to achieve before becoming technically feasible for aircraft applications using statistical procedures to attain a preliminary design with a traditional tube and wing configuration incorporating modern technology of today. The following items are developed in more detail:

1. Real-life scenario mission specification according to the collaboration between Wright Electric & EasyJet [87]
2. Preliminary aircraft sizing for nearer term aviation needs within certification scope
3. Estimation of the minimum power required according to FAR certification constraints
4. The performance required of superconductors from a loss point of view to become a superior option compared to the alternatives

5.1 Mission Specification

Short haul flights under two hours are generally undertaken by aircraft such as the A319 or A320 series. The following mission specifications have been formulated to guide the design process using real operational data of airports and ambitions of the aviation industry:

1. Range of 335 miles
2. Loiter capacity of 30 minutes
3. 120 seat capacity
4. Flight time under 120 minutes
5. Capable of operation from a 2200m runway
6. FAR 25 Certification

5.2 Initial Sizing

One of the important differences in the design process of the fully electric aircraft is the constant "fuel" weight which does not drop during various flight stages. Normally the gross take off weight, W_0, is defined as

$$W_0 = W_{crew} + W_{payload} + W_{fuel} + W_{empty}$$

where $\frac{W_e}{W_0} = AW_0^c$ is a statistical regression line for aircraft and W_e is the empty weight [47]. The Breguet range equation is used to determine the fuel usage at different flight stages and to account for the lower lift requirements during flight which is not the case for a fully electric aircraft. Nonetheless, previous aircraft designs can be used to guide the preliminary design and estimate the fuel weight which is effectively then the maximum battery weight [108]. A database of historic aircraft, such as Jane's, reveal statistical trends that are used to provide benchmarks for design parameters [47]. Table 5.1 lists similar mission specification turboprop aircraft, most are transport aircraft used for the military as most passenger aircraft are jet based.

Table 5.1: List of comparable propeller based historical aircraft revealing a trend between MTOW and several design parameters. Weights are in kg.

Turboprop	**Takeoff Weight,** W_{TO}	**Empty Weight,** W_E	**Maximum Landing Weight**	**Max. Fuel Weight,** W_F
DB Atlantic 2	43,990	25,352	36,075	18538.63
Transall C-160	51,107	28,059	47,098	17,491
Aeritalia G222	28,059	15,432	26,554	9421
Fokker F27 Maritime ,	20,455	12,545	18,636	7273
Lockheed C130E	70,455	34,241	59,091	28,820
Lockheed P3C	61,264	27,950	47,218	27,390
Grumman C2A	24,923	14,160	21,533	5430
Shorts Belfast	104,545	59,091	97,727	37,455
Antonov AN26	23,048	15,051	23,048	5511

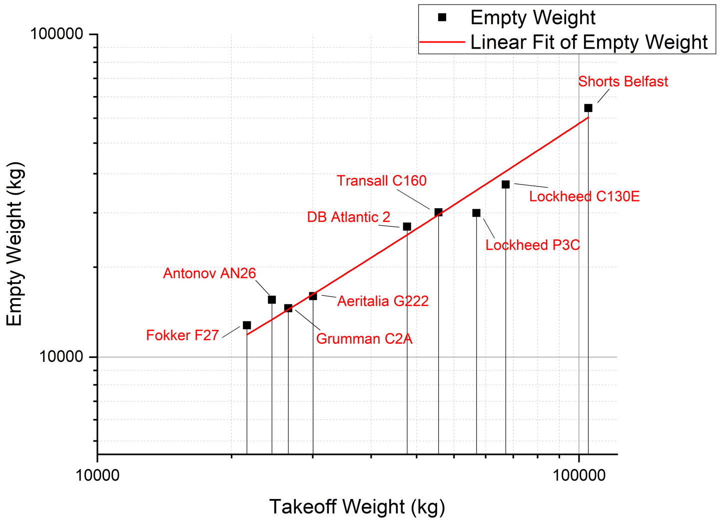

Figure 5.1: Log-Log plot of take-off weights vs. empty weight reveals a linear regression fit across several brands and models of turboprop aircraft.

From the mission specification a payload weight for a fully electric aircraft for short haul trips can be estimated for average body weights and baggage allowances as [111]

$$80kg \times 120pax = 9,600kg$$
$$15kg \times 120pax = 1,800kg$$

resulting in total maximum payload of 11,400kg. The baggage estimate is based on Easyjet's 15kg free baggage policy and assuming all passengers carry the maximum hand luggage and no checked in luggage. Similar to the relationship shown by figure 5.1, the MTOW is related to the payload weight with a regression line based on previously flown similar aircraft. A payload weight of 11,400kg corresponds to an approximate MTOW of 38,800kg.

For a transport aircraft there are several flight stages which determine the amount of fuel needed including startup and warm up(1), taxiing(2), take-off(3), climb and accelerate(4), cruise(5), loiter(6), descent(7) and shutdown (8). For all flight stages apart from cruise and loiter, standard ratios for the aircraft class are used for the initial design and are shown in table 5.2.

Table 5.2: Fuel fraction data for historical planes [86]

Flight Stage	Fuel Fraction
1	0.99
2	0.99
3	0.996
4	0.985
7	0.99
8	0.99

The cruise and loiter aspect are more mission dependant and are calculated independently by re-arranging the Breguet range and endurance equations shown below [15].

$$Range = 375 \left[\frac{\eta_p}{c_p}\right] \left[\frac{L}{D}\right] \ln \left[\frac{W_i}{W_i + 1}\right] \tag{5.1}$$

$$Endurance = 375 \left[\frac{1}{v_{ltr}}\right] \left[\frac{\eta_p}{c_p}\right] \left[\frac{L}{D}\right] \ln \left[\frac{W_i}{W_i + 1}\right] \tag{5.2}$$

Raymer has shown for several class of aircraft there are statistical regression lines which can predict the L/D of aircraft provided the approximate wetted area of the aircraft is known [84]. In terms of size, a Dash 8 has a similar passenger capacity and other similar aircraft are used to determine a range of L/D between 12 and 17. A parameterised study is computed with Matlab to determine the various fuel fractions as a result of changing aircraft parameters. The result is used to either revise the estimated MTOW or select the range/aircraft parameters to match the MTOW and attain a feasible preliminary design by matching the empty weight with the regression found using equation 5.3. The endurance fuel fraction is calculated by using a loiter speed of $92 m/s$ and is found by a regression method described further below.

$$M_{ff} = \frac{W_1}{W_{TO}} \left[\frac{W_2}{W_1} \frac{W_3}{W_2} \frac{W_4}{W_3} \frac{W_5}{W_4} \frac{W_6}{W_5} \frac{W_7}{W_6} \frac{W_8}{W_7}\right] \tag{5.3}$$

$$M_{ff} = \frac{W_8}{W_{TO}} \tag{5.4}$$

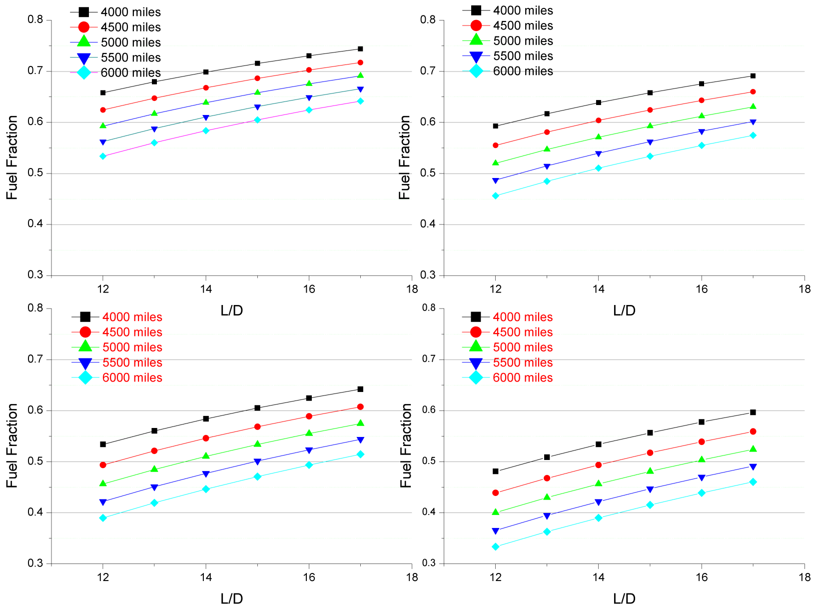

Figure 5.2: Various fuel fraction ratios resulting from a parametric sweep of design parameters used to select realistic and appropriate values for the corresponding MTOW.

The loiter speed is an important parameter which can heavily influence the final fuel requirements. It is determined by comparing similar turboprop aircraft's wing loadings, which are generally between 350$^{kg}/_{m^2}$ to 500$^{kg}/_{m^2}$. As the parasitic drag and the induced drag of an aircraft are hyperbolic there is an optimum loiter speed which needs to be estimated, this required an estimation of the drag polar of the aircraft shown by equation 5.6 [6]. The drag is proportional to the wetted area of the aircraft and is related to the MTOW. Using a regression method the total wetted surface area is estimated at $503m^2$ [86]. Along with the regression model a major fuselage breakdown revealed consistent figures. Using Easyjet's standard 29" seat pitch and 18" width and a 1 aisle 6 seat configuration the diameter was estimated at 3.52m taking into account the fuselage thickness. The cockpit is modelled as a half hemisphere while the wing surface area is estimated using the wing loadings of modern turboprop aircraft. The calculation shown below reveals a similar value to the regression indicating a reliable value.

$$S_{wet} = 4 \times \frac{38,800}{450} + \pi(3.527)(14.73) + 2\pi(1.76^2) = 527m^2$$

The drag polar's parasitic component, C_{D0}, is found to a good approximation by considering the relationship between the frontal aircraft area and the wing area. Thereby using an equivalent parasitic area, C_{D0} is

$$C_{D0} = \frac{f}{S} = \frac{23.605ft^2}{928ft^2} = 0.0254$$

reflecting a moderately aerodynamic design [86]. f is an equivalent frontal area to normalise and compare the aerodynamics of various aircraft to the wing area, S. The induced drag caused by lift generation is more complicated and depends on the lift distribution across the wing surface along with aspect ratio and sweep effects. Wings do not achieve the ideal induced drag due to mechanical considerations preventing an ideal lift distribution. An efficiency factor, e_o, is applied to take into account the non ideal lift distribution whilst many empirical and theoretical equations exists to estimate the factor and is displayed by equation 5.5 [73] [92].

$$e_o = \frac{e_{o\Lambda}}{\pi(AR)k + {}^{1}/_{us}} \tag{5.5}$$

where $e_{o\Lambda}$ is a function taking into account the variable effects of a sweep and u and s take into effect the non-ideal surroundings of the wing i.e. fuselage and $k = f(C_{D0})$. The resultant distribution in the factor is displayed by figure 5.3. Based on this distribution and the estimation of the parasitic drag an e_o value of 0.75 is selected based on modern wings with their composite structures being able to achieve an aspect ratio of 11+. Thus the drag polar is:

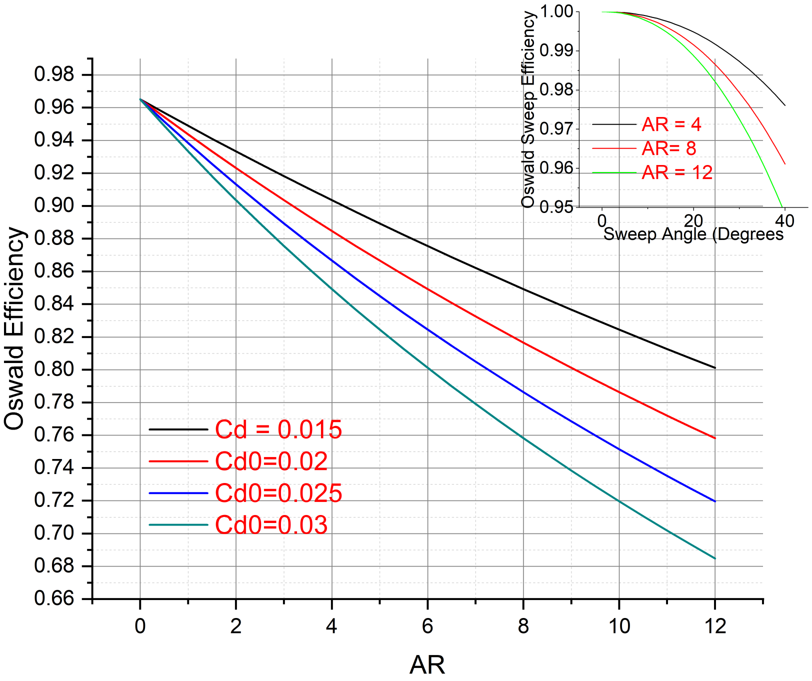

Figure 5.3: The variation of the span efficiency with various design parameters. Several sources agree with a value between 0.75 and 0.9 showing the calculated values match [86]

.

$$C_D = C_{D0} + \frac{C_L^2}{\pi A R e_o} \tag{5.6}$$

$$= 0.0254 + 0.0386 C_l^2 \tag{5.7}$$

which is normalised by $\frac{\rho S v^2}{2}$ where ρ is the air density at the flight altitude.

Now that the drag polar is estimated the optimum loiter speed can be found. Range and endurance of an aircraft require different optimisations. The maximum range occurs when ${}^{dW_f}/_{dS}$ is minimised while the maximum endurance occurs when ${}^{dW_f}/_{dt}$ minimised where dS is the change in distance and dt the change in time. Power in steady level flight is:

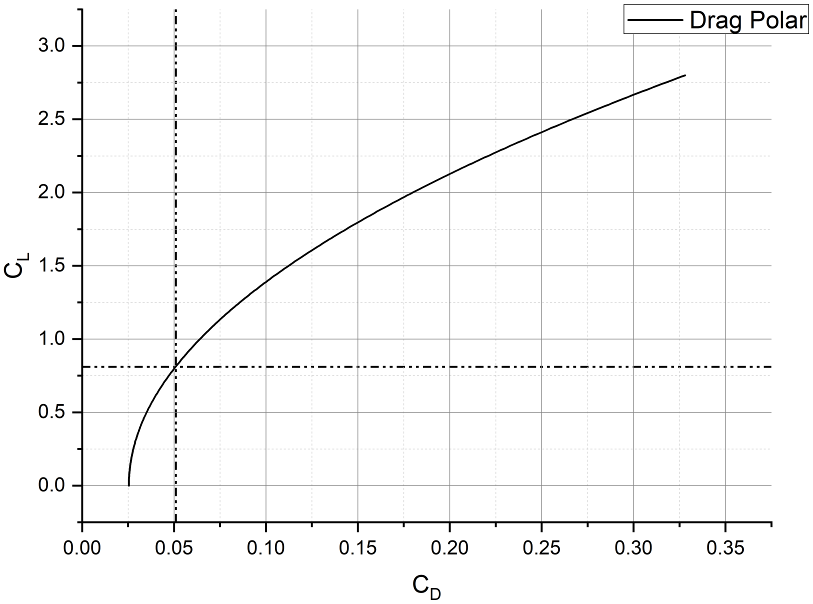

Figure 5.4: Polar drag graph plotted using equation 5.7 revealing a maximum L/D within the expected range from figure 5.2 of 15.97.

$$P = W\frac{C_D}{C_L}v$$

while v is equal to $\sqrt{\frac{W}{0.5\rho S C_L}}$, thus the power becomes

$$P = \sqrt{\frac{W^3}{0.5\rho S}}\frac{C_D}{C_L^{1.5}} \tag{5.8}$$

which implies to achieve the maximum endurance time $C_L^{1.5}/C_D$ should be maximum as opposed to the range which equation 5.1 seeks to maximise C_L/C_D for the best operation. Figure 5.5 shows an optimum speed of loiter at 92m/s vs. an optimum cruise speed of 121 m/s. The fuel fraction needed during the loiter period is therefore

$$\frac{W_7}{W_6} = (e^{\frac{(0.5)(203.6)(0.7)}{(375)(0.85)(16)}})^{-1} = 0.986$$

using imperial units. Substituting the fractions from table 5.2 and the result

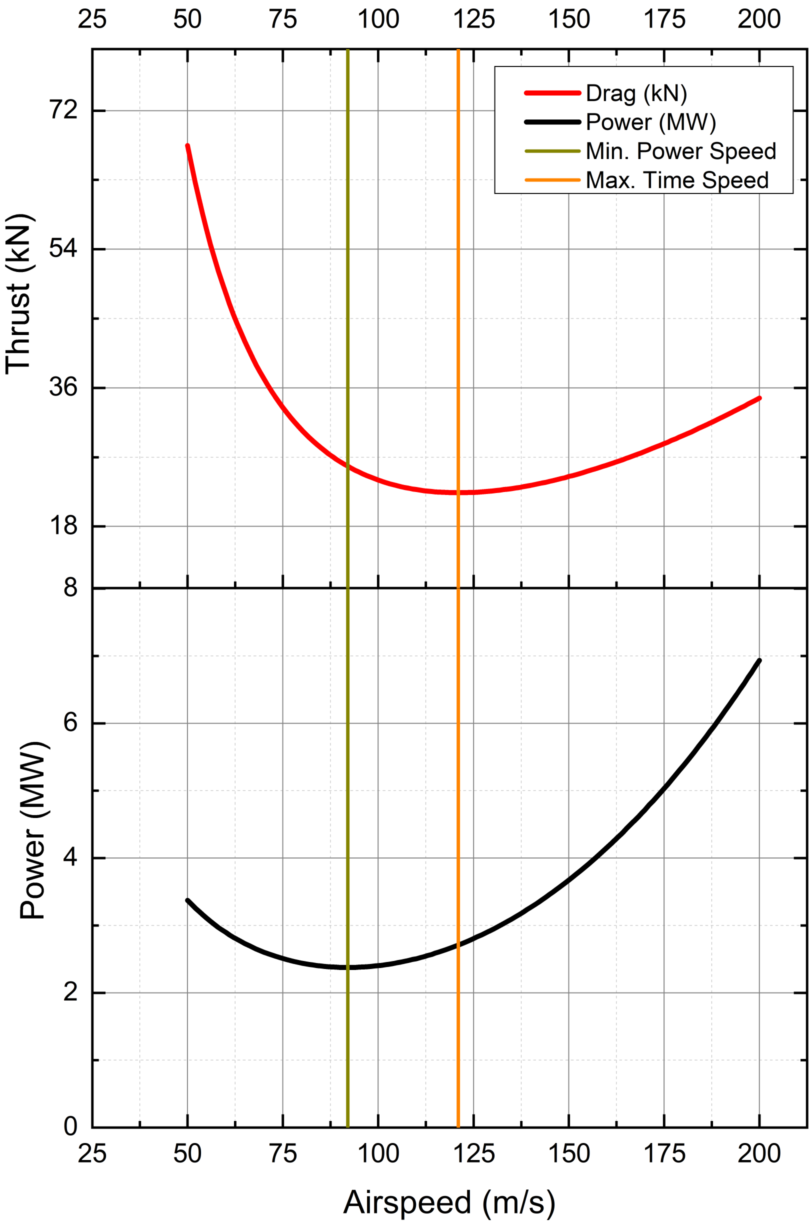

Figure 5.5: Power and thrust requirements vs. flight speed for an 18,000 ft altitude. The optimum speeds for cruise and loiter are found to guide the estimation of the fuel fractions needed to complete the mission specification.

of the loiter fuel fraction into equation 5.3 finds

$$0.929\frac{W_6}{W_5} = 0.856$$

where 0.856 essentially sets the fuel fraction required to achieve a minimum allowable operating empty weight of the aircraft according to regression data [86]. $\frac{W_6}{W_5}$ is equal to 0.921 which when substituted into equation 5.1 yields a range of approximately 923km.

Thus the preliminary design of a propeller based, kerosene powered aircraft capable of carrying out the mission specification has been developed and reveals a fuel weight of 5573kg to fly a range of approximately 1000km with a payload of 11400kg. The performance of this aircraft matches with turboprop aircraft of the past. Considering solely an energy basis, at 42.8MJ/kg of specific energy for kerosene, the total energy needed to complete the mission is 238.5GJ. Batteries since the 1900s have improved linearly with each specific chemistry and exponentially in newly discovered chemistries [103]. Whilst theoretically a battery can achieve mass specific energy densities nearing kerosene, limits in the physiochemical design such as the current collectors or membranes restrict these to more sober values [91]. Interest in battery technology has led to recent improvements in the energy densities of up to 400$^{Wh}/_{kg}$ whilst NASA use a 750$^{Wh}/_{kg}$ value in their next generation studies. Assuming the best case scenario whereby the aircraft was taxied to the runway with no fuel penalty the amount of energy used for take off and climb is 31.4GJ, i.e. the aircraft would not be able to take off without a battery energy density of at least 1565$^{Wh}/_{kg}$ after which the capacity will have been exhausted. The designed aircraft does have a longer range than required for commercial interest by 384km which would reduce the take-off weight and amount of fuel required to 3,332kg and a MTOW of 36,559kg. Even so, with the reduced weight and range a take off energy of 29.6GJ would still be required. Clearly it is not feasible in the near term for battery powered aircraft to fly even with huge increases in their capacities as has been suggested by some firms and airlines, even for reduced ranges.

5.3 Hybrid Propulsion

It has been shown that a battery powered aircraft would need momentous increases in specific power and energy to allow an aircraft to just take-off and no amount of A.C. loss reduction could overcome the battery penalty, however; there is scope to use a hybrid solution whereby a gas turbine is used to power the aircraft during high energy flight conditions and a partial or complete switch is made to batteries during less demanding stages [29]. During the first four stages of flight and until the aircraft has reached its cruising altitude more than 26.7% of the fuel has been burned according to table 5.2 and the calculations using the range and endurance equations from section 5.2. Several studies have shown there is great potential for a hybrid propulsion system to dramatically reduce emissions by using a GT for heavy duty flight stages and switching to an electrical propulsion for others [30] [17]. A "hfan" propulsion system as proposed by Bradley et. al. is assumed to be used in this analysis in much the same installation as GTs on a tube and wing aircraft [19]. The process to ascertain whether a hybrid propulsion system can meet the mission specification is to first identify the changes in the aircraft empty operating weight due to a jet based design vs. the propeller based design of the previous section as well as changes due to a new drive system including batteries, power inverters, cryocoolers and GT modifications. First the GT alone is sized to complete the mission specification without considering a hybrid propulsion system and is the reference baseline design, the impacts of hybridisation are subsequently analysed on the aircraft's performance. For the hybrid propulsion system a new design iteration is needed which takes into account a jet-based aircraft which modifies the breguet range equations to take into account the TSFC and different drag polar. The key output of the new design iteration are outlined below in table 5.3 and followed a similar design procedure as demonstrated earlier:

Table 5.3: Jet aircraft design parameters

Design Parameter	Value
W_{TO}	40,499kg
Drag Polar	$0.0174+0.0376C_l^2$
Max $^L/_D$	21
P_{cruise}	2.49 MW
m_{PL}	11,400kg
$TSFC$	0.7 $^{lbs}/_{lbf/s}$

5.3.1 Sizing Constraint Diagram

Firstly, to determine the thrust rating required of the GT and the subsequent weight changes expected for the aircraft due to hybridisation, it is required to determine realistic figures for the thrust to weight (T/W) ratio taking into account the realities of flight performance according to regulations. The key flight stages considered are take off, climb, cruising, manoeuvring and landing in relation to the following regulations:

1. FAR 25.113 - Clearance of 35ft from ground roll to end of take-off length
2. FAR 25.111 - OEI Climb gradient of 1.2% in initial climb segment
3. FAR 25.121 - OEI climb gradient of 2.4% in second segment climb, 2.1% for balked landing
4. FAR 25.337 - Appropriate sizing for a maximum 2.5g manoeuvre

Whilst the aircraft is being powered by the GT the design criteria is based on the thrust to weight ratio while the electric motor is sized according to the most taxing cruise conditions and the formulae are modified to reflect a power to weight ratio. By minimising the motor power required through the minimisation of the flight power to weight ratio required, the mission specification is more likely to be completed.

The specific excess power equation is used to calculate the sizing of the engines. Equation 5.9 shows the power needed on the left hand side equalled with the potential energy change plus the kinetic energy of the aircraft. Replacing the drag with its dimensionless form, equation 5.9 is rewritten to isolate the thrust to weight ratio and produces figure 5.6 which shows a minimum thrust to weight ratio of 0.43.

$$\left(\frac{T}{W} - \frac{D}{W}\right)V = \frac{1}{V}\frac{dh}{dt} + \frac{1}{g}\frac{dV}{dt} \tag{5.9}$$

$$\frac{T_{SL}}{W_{TO}} = \frac{q}{\alpha}\left[\frac{C_{D0}}{W/S} + k_1\left(\frac{n\beta}{q}\right)^2 (W/S)\right] + \frac{\beta}{\alpha}\frac{1}{V}\frac{dh}{dt} + \frac{1}{g}\frac{dV}{dt} \tag{5.10}$$

where T_{SL} is thrust at sea level, g is the gravitational constant, α is the lapse rate, β is the flight stage weight fraction, k_1 is the induced drag co-efficient, h is the altitude and V the airspeed.

The take-off requirement is based on historical performance data of several aircraft which derives a performance parameter proportional to the wing loading shown by equation 5.11 [86]. The lift coefficient is a design variable and is parameterised between a range of realistic values depending on the wing extensions used.

$$s_{tofl} = \frac{37.5 {}^{W}/{}_{S_{TO}}}{\sigma C_{L_{MAXTO}}} = 37.5 TOP_{25} \tag{5.11}$$

where TOP_{25} is a performance parameter, $C_{L_{MAXTO}}$ refers to the lift coefficient of the wings with flap settings according to the take-off procedure.

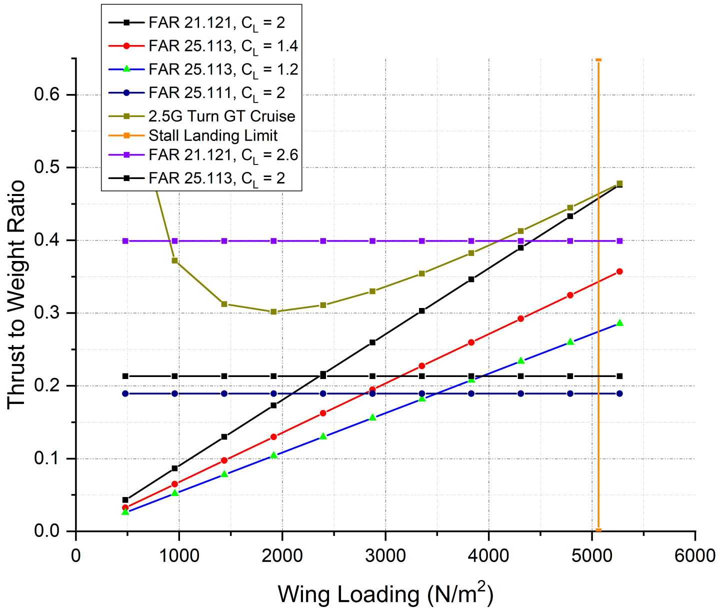

Figure 5.6: Constraint diagram for the sizing of a GT showing a minimum thrust to weight ratio of 0.44 equating to a 83.7kN rating.

Following the collation of several GT from different manufacturers including GE, CFM, Rolls-Royce and Pratt & Whitney a linear relationship between the thrust required and the engine mass was found according to $T = 59.05M_{GT} - 26056$ resulting in an approximate engine weight of 1858kg.

Engine modification would be required to embed a motor to the LP spool. The first stage LP fan would be driven as a propeller and the bypass air would create the thrust. An assumption is made here that the fan is optimally designed for both turbo operation and propeller use although in reality it would need multi objective optimisation. The motor is rated in terms of power as the thrust produced is a derivative of the propeller setup. Figure 5.7 displays the minimum constraints set by the cruise and turn capabilities of 8 ${}^{W}/{}_{N}$ resulting in a 1.52MW requirement for a 40,499kg plane.

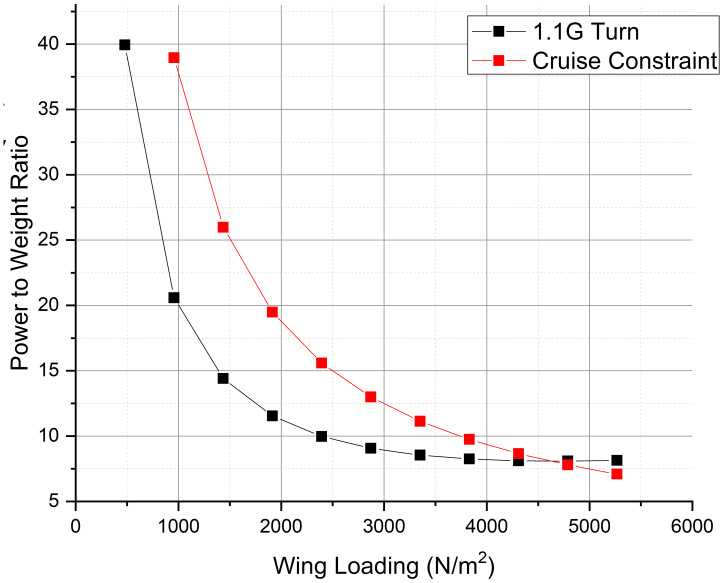

Figure 5.7: Constraint diagram for sizing of the required motor power showing a minimum weight ratio of 8 at the selected wing loading equating to a motor rating of circa 1.52MW per engine.

Using the method above to calculate the thrust and power to weight ratios allows a minimum sizing for each drive system to be completed. To increase the accuracy of the baseline A.C. loss target the weight modifications, which can be significant, need to be taken into account.

Whilst a power density of $5^{kW}/_{kg}$ was achieved by Siemens in 2015 for a conventional AFPM machine, NASA estimate power densities could reach above $15^{kW}/_{kg}$ excluding the cooling systems, see figure 1.6. Descriptions and results of theory and practical work have demonstrated partially superconducting motors are more power dense than jet engines and can reach 17 $^{kW}/_{kg}$ [66]. Whilst manufactured partially superconducting machines show power densities of up to 10 $^{kW}/_{kg}$; their theoretical counterparts with advanced shielding and air core designs could reach up to $25^{kW}/_{kg}$ and their fully superconducting counterparts even more so [45] [44]. Partially superconducting motors are considered here as they have been the most developed with HTS field windings and are viable.

5.3.2 Weight Modifications

Estimating the additional weight of a hybrid gas turbine is difficult as the design knowledge base is much more limited. NASA's Sugar study approximates an additional mass for the hybrid propulsion GT integration of 3,379 lbm to integrate a 5,500 HP motor along with the gearbox to drive the LP spool [19]. The mass does not include the cooling system which would not be situated inside the engine. Whilst the study does not mention a power density used it may be estimated by subtracting the mass of the gearbox. Lolis & Teeuwen provide an analytical means to calculate the mass of modern geared turbofan gearboxes using a correction factor to reflect modern advances shown in equation 5.12 [64] [105]. Using the graphs in these works the gearbox mass with accessories is estimated at 270kg resulting in a power density of $3.5^{kW}/_{kg}$ at the motor, which is better than current conventional motors.

$$m_{gb} = 0.0801Q^{0.84} \tag{5.12}$$

where Q is the engine torque.

The introduction of the hybrid system results in a minimum power density the additional weight must provide to prevent a recursive increase in total mass i.e. an increase in the mass of the propulsion system results in an increase in the power requirements, which in turn increases the propulsion system mass. Using the most stringent constraint condition from figure 5.6 of FAR 21.121 a minimum thrust to weight ratio of 0.3912 and power to weight ratio of 8.15 are required. The weight modification rules are summarised in table 5.4. NASA's Sugar study is used to approximate an additional mass for the hybrid system including gearbox and of the battery integration mass to include structures and cables with a linear model used to reflect the smaller passenger aircraft of this study [19]. The final mass value is modified to incorporate Berg's assessment of superconducting machine density based on theory and past machine demonstrations [14]. The cryocooler mass is estimated using the models of several cryocooler surveys of both air-forces, spacecraft and ground systems [55] [14]. The inverter mass is estimated according to Felder's approximation of power densities for next generation power electronics [21].

The cryocooler mass is also modified with a correction factor, 0.6, to reflect a cryocooler survey of air force and space equipment which have been designed for aerospace applications [55]. The cryocooler power input is determined by mechanical and thermal efficiencies according to equation

Table 5.4: Weight modification rules

Major Component	Mass
Battery Integration	$\frac{6000}{5500}P_{motor}$
GT Modifications & Gearbox	$\frac{3379}{5500}P_{motor}K$
Cryocoolers	$(0.6)(0.0711)P_{in}^{0.905}$
Power Inverter	$\frac{1}{15}\frac{P_{in}}{(745.7)(2.2)}$

5.13 where a typical value of η_c is 0.3 [14]. Q_c represents the heat load from the machine.

$$P_{in} = (\frac{Q_c}{\eta_c}\frac{T_h - T_c}{T_h}) \tag{5.13}$$

Thus, assuming a -25°C ambient temperature at 20,000 feet and an operating temperature of 50K, the carnot efficiency is equal to 0.259, it is assumed that 10% of the ideal carnot efficiency can be achieved on the basis of previous models [55]. For a range of heat loads the anticipated mass of the cryocooler components and others are shown in figure 5.8. The initial take-off mass for the baseline plane is 40,499 kg, the first iteration results in a large increase of approximately 2000kg for a fixed battery mass, further iterations result in smaller power to weight ratio increases due to slightly varying drag polars and thus there are more modest increases in the additional mass as cryocooler heat load is increased. The iterations were carried out until the masses reached within 1% of each other. The "F" column indicated the weight changes where battery mass is kept constant while "V" represents a floating battery mass that is able to complete the mission specification and thus have more significant mass changes.

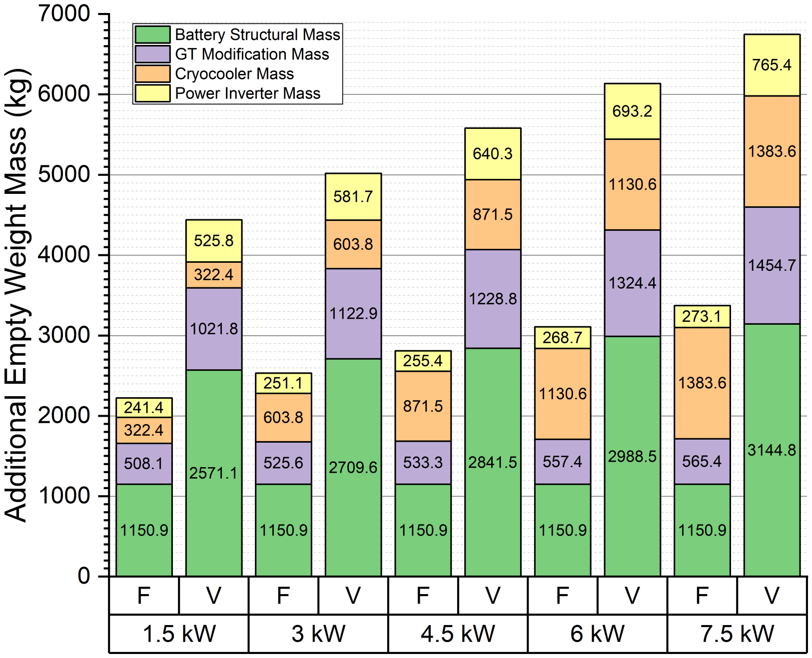

Figure 5.8: Extra take-off mass required to fly with varying levels of cryocooler heat load powers. With increasing cryocooler load the power to weight ratio sensitivity meant there are small increases to the other masses. The "F" column corresponds to weight changes where the battery mass is kept constant to replace simply the fuel weight from the baseline design. When the batter mass is allowed to float to meet the required range more drastic increases in total weight change are evident.

5.4 Motor Driven Aircraft

The established breguet range/endurance equations cannot be applied in battery powered aircraft calculations as they take into account a mass change during flight and thus the dependence of flight speed on the lift required. Instead the endurance and range equations are calculated according to equation 5.14 which instead takes into account the optimum drag polar considering a constant weight [109] [8].

$$R_{max} = 3.6Rt^{1-n}\left[\frac{VC}{{}^{1}/{\sqrt{\rho S}C_{Do}^{0.25}(2W\sqrt{k})^{3/2}}}\right]^{n}\sqrt{\frac{2W}{\rho S}\sqrt{\frac{k}{C_{DO}}}} \tag{5.14}$$

where k is the induced drag coefficient, Rt is the battery hour rating, and VC the battery capacity.

In this study, due to the assessment of electrical propulsion for traditional tube and wing design it is assumed that the drag polar cannot be optimised for electrically propelled aircraft without big changes to the aircraft configuration and thus a non-optimum aerodynamic efficiency is used. In the case of electrical aircraft the parasitic drag needs to be minimised and the induced drag coefficient maximised. The ranges calculated are shown by figure 5.9. For a zero cryocooler heat load (i.e. a conventional electrical aircraft) the range for the aircraft of table 5.3 can fly 1759km, an introduction of the hybrid propulsion system drastically reduces the range. The requirement cannot be met for battery capacities less than 1250 ${}^{Wh}/_{kg}$. For a 1250 ${}^{Wh}/_{kg}$ battery the maximum allowable total load on the cryocooler is 3kW. Whilst the mission specification range is 594km, the design empty weight of an aircraft has been shown to change during the manufacturing stage and a 5% growth factor was applied resulting in a range requirement of 636km indicated by the red dotted line [108].

Equally important to the viability of hybrid electrical aircraft is the emission impact of the electrical system. While the in-flight fuel use is reduced to zero, the increase in MTOW due to the battery mass and associated structural mass results in an increased fuel requirement to get the aircraft to cruising altitude. Thus, introducing electrical flight is not inherently a design choice that can lead to lower emissions. The effect of this is shown by figure 5.10, for lower battery capacities the emissions are actually higher than current aircraft by circa 10% with an almost doubled battery capacity compared to what is commercially available today. Significant emissions savings are achieved with battery capacities approaching 1500${}^{Wh}/_{kg}$ where, depending on the cryocooler power, a 25% reduction in emissions may be

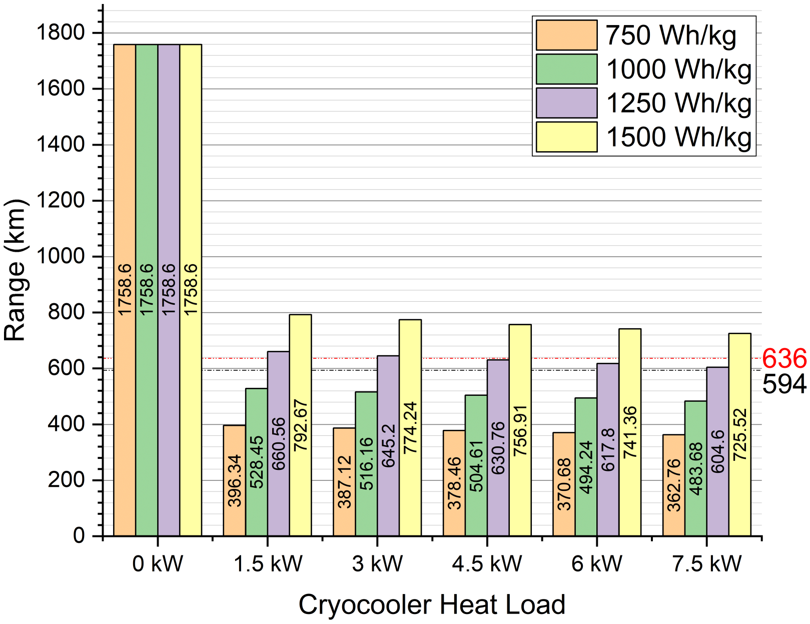

Figure 5.9: The range variation of the aircraft with varying amounts of input cooling power to the cryocooler. 0kW signifies a traditional aircraft with jet-fuel for the entire mission whilst the rest are of a hybrid configuration. An increase of 6kW heat load removal reduces the aircraft range by 56km for a battery capacity of 1250 $^{kW}/_{kg}$.

achievable. It is also important to realise the impact factor of releasing the emissions at altitude means in most measurements the emissions saving would be equivalent to a 50% reduction. Finally, it is important to note the analysis presented does not assume any improvement in the aerodynamic efficiency beyond modern age current jet aircraft. Proposals to more than double the L/D ratio would drastically change these figures such as the NASA SUGAR HIGH concept.

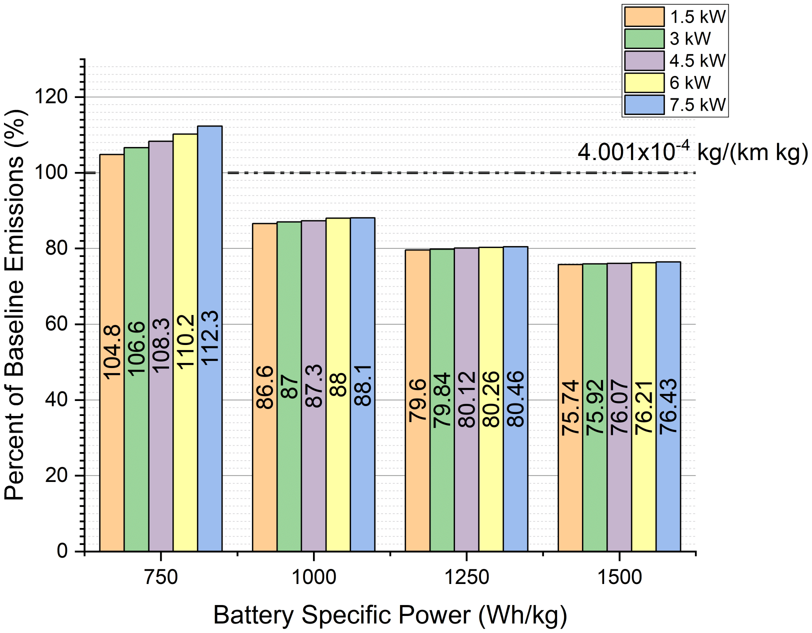

Figure 5.10: Even with great improvements of battery technology to $750^{Wh}/_{kg}$ it is unlikely any benefits from an emissions viewpoint can be gained. This is due to the extra mass involved to hybridise an aircraft. Reduction of up to 25% can be met with battery densities of $1500^{Wh}/_{kg}$. The legend shows the cryocooler heat loading.

5.5 Superconductor A.C. Loss Performance Target

Low temperature cryostat design has evolved to attain excellent performances in terms of heat leak into the refrigerated space. Using vacuum, MLI and active shielding along with suitable material choices a carefully designed cryostat will have negligible heat leak losses due to the cryostat itself [27] [114]. In practice a trade-off between cost, manufacturing and heat load will likely result in an elevated heat load.

A 1 MVA transformer built for a commercial grid application in New Zealand showed cryostat heat loads of approximately 50:50 ratio compared to the A.C. loss itself [38] [37]. Besides the cryostat heat load and A.C. losses the current leads are a significant thermal load. Shaft feed-throughs are another direct link with the ambient but the literature has shown that with careful design using appropriate materials, the loss can be reduced to a negligible amount in the 10's of watts [126]. Whilst for a partially superconducting motor with HTS field windings a significant heat load would be generated by the rotor; it has been shown in literature the loss is dwarfed by the potential losses in the stator of a fully HTS machine and is therefore considered the sole source of superconducting heat load in the analysis of this work [63]. A suitable machine design found in the literature consists of a PM rotor with superconducting racetrack coils with a rated speed of 1500RPM and power rating of 1MW, which is suitable to consider given the sizing output of the previous sections; the motor parameters are reproduced in table 5.5 [124] [121].

Table 5.5: Machine design parameters for a 1MW aircraft propulsion motor derived by Zhang et. al. [121]. Reproduced under Section 29(1) of the Copyright, Designs and Patents Act 1988.

Parameter	Quantity
Machine Power	1MW
Length	0.63m
Magnetic Loading	0.67T
Electrical Loading	$72^{kA}/_{m}$
Air Gap Radius	0.215m
Total Turns	78
No. of Coils	6
Tape Length per coil	254m

Whilst Zhang's investigation shows it is better to increase the current loading especially for HTS stators, and keep the rotor magnetic field to a minimum, the maximum investigated rotor field of 1.5T does not reflect the realistic flux densities of 3-4T that would be needed to meet beneficial power densities [60]. Incorporating this aspect requires an A.C. loss model, NASA's previous work is utilised for this purpose which has been further developed to incorporate coupling and eddy current losses for multi-filamentary conductors [20]. In this approach the engineering current density is modelled by an exponential function shown in equation 5.15.

$$J_{eng}(T,B) = J_{eng}(20,B) \times (1.4235 - 0.022467T + 0.000058307T^2) \quad (5.15)$$

for $T < 50K$ and $B < 3.5T$ while,

$$\begin{aligned} J_{eng}(20,B) = J_{eng}(77,0) \times (5.22 - \\ 1.5166B + 0.353B^2 - 0.037625B^3 + 0.0014773B^4) \end{aligned} \quad (5.16)$$

for $B < 10T$. The stator A.C. losses can then be calculated accordingly

$$P_h = \frac{8}{3\pi} J_c B d_s f V_{filaments} \quad (5.17)$$

$$P_e = \frac{\pi^2}{4\rho_n} (B d_w f)^2 V_{matrix} \quad (5.18)$$

$$P_c = \frac{1}{4\rho_n} (B L_t f)^2 V_{matrix} \quad (5.19)$$

so the total A.C. loss, P_{ac}, is equal to $P_h + P_e + P_c$; the sum of the hysteresis, eddy current and coupling losses respectively. Equations 5.17 to 5.19 take into account the magnetisation losses of the superconductor only. It has been shown in past work that the transport loss at high ratios of current vs. the critical current remains constant whilst in high external fields, as studied here, the magnetisation loss increases by orders of magnitude [83]. Therefore, the loss model takes into account the dominant losses. V is the volume of the specified components in the associated subscripts. d_w is the wire diameter while d_s is the strand diameter.

Current leads for HTS applications have been re-designed to incorporate HTS transitioning to reduce the heat load by recovering cold gas in the case of wet cooling or using a second stage cryocooler to remove losses into the cryostat [11]. An analytical model was designed for the heat load caused by HTS current leads by Chang et. al. considering a thermal energy formulation [24]. It was found that at a critical current of 10,000 $^{A}/_{cm^2}$ the total heat load on the cryocooler for a 20cm lead is 0.0907$^{W}/_{A}$ operating at a temperature of 80K. Adapting condition 3 from Zhang's work, for the electrical loading at 108$^{kA}/_{m}$ to take into account the increase in the field density to 3.5T, the estimated current required is

$$\pi \times 0.43m = 1.351m$$

$$1.351 \times \frac{108kA}{5.22} = 27.95kA$$

resulting in a heat load of

$$\frac{27,950A}{(6)(78)} \times 12 \times 0.0907 = 65W$$

to be dissipated by the cooling mechanism.

Recent advances have been made in the manufacture of BSCCO wires with a higher packing factor of filaments within the same volume of matrix along with enhanced decoupling between them by heat treating the wires with pressure; the cross-section of such a wire is shown in detail by figure 5.11. Instead of using a reference J_{eng} of $150 A/mm^2$ as Felder did, the improvements since means it can be increased to $200 A/mm^2$ [57].

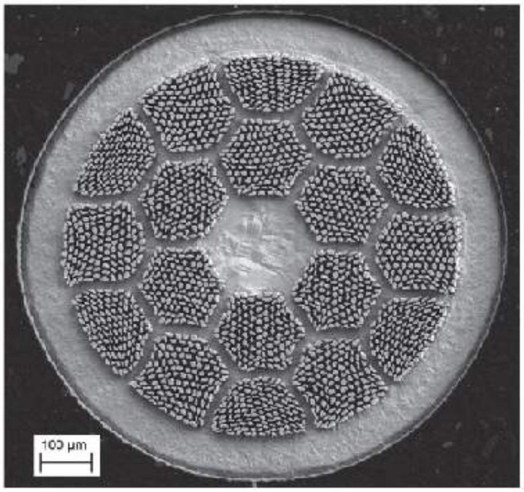

Figure 5.11: SEM image of a 121 × 18 BSCCO wire made using the PIT process [48]. Reproduced under Section 29(1) of the Copyright, Designs and Patents Act 1988.

$V_{filaments}$ is calculated by using a filament diameter of $9.1\mu m$ and assuming a circular cross section. Thus for $1m$ of wire the total volume of filaments is

$$\begin{aligned} V_{filaments} &= 216\pi(\frac{9.1}{2 \times 10^6})^2 \times 1 \\ &= 1.4 \times 10^{-8} m^3 \end{aligned}$$

and the diameter of the wire as a whole is selected as $1mm$. The in-field current density of the BSCCO is estimated at $190.3 A/mm^2$ based on the information shown in figure 5.12 and derived from equation 5.15. Due to the lower lift factor used between this work and Zhang's work owing to the different working field magnitude, a modification must be made to the total length of conductor to achieve the same power rating. The original machine amp-turn rating is $23{,}400 AT$ according to table 5.5 which was achieved with a turn number of 78 and I_c of 300A. The new length of wire required is calculated from the updated I_c which is

$$(190.3)(0.785) = 149.44A$$

where 0.785 is the conversion from current density to current and is used to find the number of turns as 30:

$$\frac{23,400}{5.22} \div (190.3)(0.785) \approx 30 turns$$

Thus using an average turn length the total volume of filament for the entire machine is estimated to be

$$(1.4 \times 10^{-8})(30)(6)(\frac{254}{78}) = 0.0000082 m^3$$

and the matrix volume per meter, V_{matrix}, is

$$\begin{aligned} &\pi(\frac{0.5}{1000})^2 - (216)(\pi(\frac{9.1}{2 \times 10^6})^2) m^3 \\ &= 77 \times 10^{-8} m^3 \end{aligned}$$

A summary table identifying the key variables is thus identified in table 5.6:

Finally, the total A.C. loss can be found as the sum of the copper terminal heat load and the total A.C. losses as

$$65W + 13,648W = 13,713W$$

from which it can be deduced that superconducting technology still has significant improvements of around 89.5% to be made in terms of A.C loss

Table 5.6: Full list of values assigned to the parameters to determine the A.C. loss.

Parameter	Quantity
J_{eng}	200 $^{A}/_{mm^2}$
B	3.5T
d_s	$9.1\mu m$
f	$60Hz$
$V_{filaments}$	$82 \times 10^{-7} m^3$
V_{matrix}	$4.52 \times 10^{-4} m^3$
d_w	0.001m
ρ_n	$1.59\times10^{-8}\Omega m$
L_t	0.005m

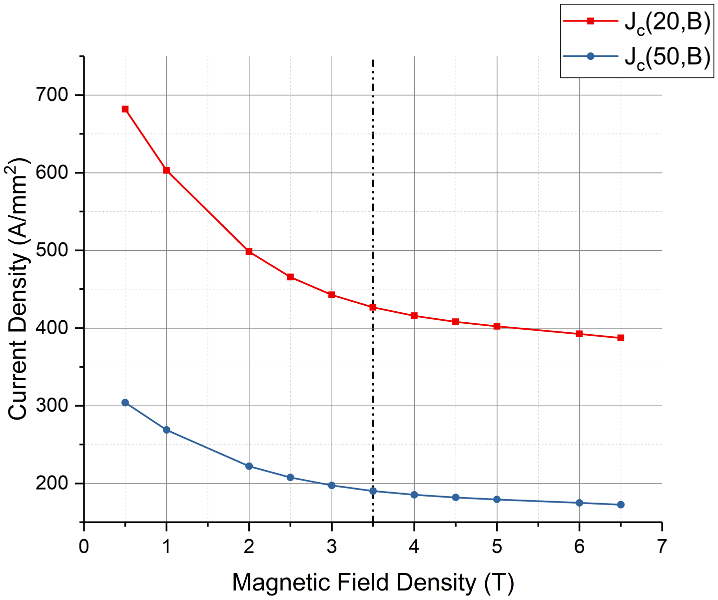

Figure 5.12: The lift factors of the BSCCO wire for varying temperatures of 20K and 50K at various flux densities. 3.5T is chosen as the design point for this work based on evidence of it providing suitable power densities.

when compared with figure 5.9 in order to meet the range requirements that would be commercially of interest. Chapter 4 found using the most advanced techniques of lowering the A.C. loss, at low to medium currents, only a fraction of the loss reduction required can be achieved. Importantly, further machine losses such as iron or shielding losses have not been considered although these do not strictly need to be linked to the cooling power and would therefore not significantly impact the final results. Figure 5.10 demonstrates it is more important in terms of emissions to improve battery capacity as the cooling power required is dwarfed by the consumption of the motors. The cooling power, and thus A.C. loss, makes the emissions variation more sensitive with lower battery capacities as it drives up the total aircraft weight. A key assumption made in the analysis is of several technologies meeting their specified target of power density and efficiency i.e. cryocoolers, power inverters, superconducting motors and the hybridisation of aircraft. The roadmap set out for these indicate they are achievable but, for aircraft at least; the key to cleaner aviation still lies with battery technology, not superconducting technology. However, by actively researching loss reduction techniques the time frame of feasibility will be brought forward and ease the target increase of battery capacities. Figure 5.13 shows the progress that has been made since 2011 in terms of manufacturing more suitable superconductors that have lowered A.C. losses by improving the fill factor of BSCCO wires. The 2011 manufacture is a baseline loss value which is assigned a 100% value for the matrix volume. The percentage decrease in the matrix volume lowers the A.C. losses. A 50% lower matrix volume results in a 60% decrease in the loss compared with the 2011 benchmark but is still considerable higher than the target required.

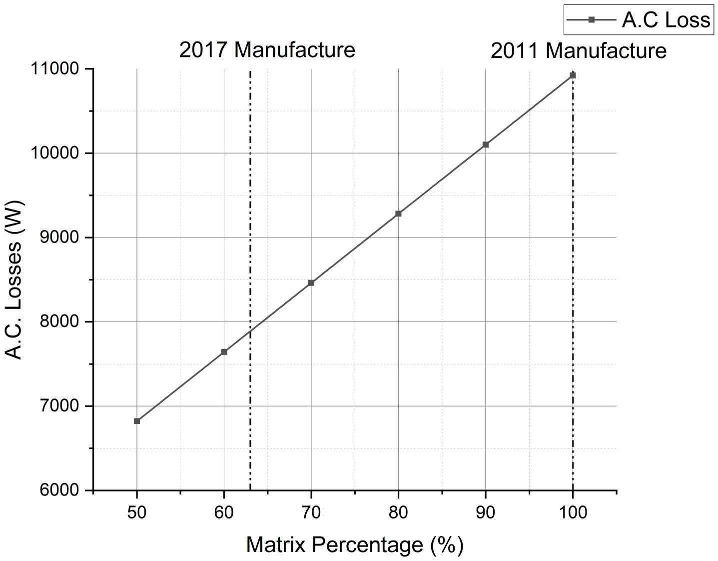

Figure 5.13: The development of manufacturing BSCCO to improve the fill factor of wires between 2011 and 2017. Long lengths are still not available for filaments lower than $10\mu m$. For comparison to the requirements of electrical aircraft, the 2011 technology is used.

Chapter 6

Conclusions

6.1 Thesis Summary

This thesis presented the design, build and test of a novel A.C. loss measurement platform inspired by the need to characterise superconducting technology in a complicated motor environment to further commercial interest as demonstrated in chapter 1. A.C. losses together with cost are two key issues of the technology and impact on numerous applications including energy storage, grid and machines so it is important to reduce both before large scale applications are feasible. Key outputs of this thesis are summarised below:

- Chapter 2 presented the design objectives and thorough mechanical, electrical and thermal design of the loss measurement platform to ensure a successful outcome. The manufacturing processes were discussed which included the use of novel materials such as graphalloy and PTFE-graphite seals.
- Chapter 3 presented a comprehensive commissioning of the newly built loss measurement platform to verify and validate the design. Aspects of the commissioning covered the nitrogen flow rate calibration dependant on the stator, copper terminals, rotor and the dissipation of the HTS coil along with the open circuit characterisation. Furthermore, the design stage was verified in terms of the expected heat load and rotor field performance.
- The measurement platform was used to measure the losses of two types of coils in Chapter 4. A standard DPC coil using heat shrink insulated tape of 25m length was characterised. The loss measurement

taken at 10Hz was used as a benchmark to ascertain the performance of a Roebel cable coil - the first testing conducted of the cabling technique inside a machine. It was found the total loss reduction achievable is up to 19%. It was found the loss measurements are accurate for current levels above 25A according to the simulations but suffer low accuracy due to rotor induced background flow at low currents. Additionally, the electrical method was used to determine the reduction in A.C. losses that can be achieved by using a striated superconductor. It was found that the total losses would be higher but for normalised comparisons the striated tape would have a lower loss by 20%, which is reduced to around half when taking into account equivalent performance requirements i.e. ampere-turns or ampere-meters. The combination of multi-filamentary wire and cabling techniques can enhance the benefits of each and lower the losses even more combined.

- The importance of knowing the goal is equally as important as achieving it. In chapter 5 an initial sizing and design of an aircraft was conducted based on the construction of past aircraft to determine the performance that HTS need to achieve. It was found that electrical flight is more sensitive to battery capacity than the cooling power required although limiting the heat load to 3 kW would make electrical aircraft using superconductors a serious option to consider. Advantageous levels of magnetic flux density to reach the required power densities result in an A.C. loss of 13.6kW - 453% the amount required to enable viable hybrid electric aircraft with a specification of interest to industry. It was also found that the battery capacity is far more important in terms of achieving hybrid electric aircraft capable of flying 330 miles with 120 passengers; the sensitivity of the A.C. loss impact on range and emissions is less when operating with higher power density batteries. It has been shown some techniques to reduce the A.C. loss can achieve up to a 30% reduction but further improvements are needed, in particular to manufacturing processes, to achieve bigger loss reductions.

6.2 Further Work

The loss measurement platform built in the course of producing this thesis is a long term piece of equipment with many uses into the future. Therefore, several recommendations are made to further improve on the operational capacity of the motor and to enable a wider range of output results to be measured. The following list provides a review of the most important further work to be carried out in order to improve the project:

1. Replace the isolation vessel with a double walled chamber with ports to allow the liquid nitrogen in the outer chamber to fill the gap. This will significantly lower the effect of rotor induced flow registered at the flow-meter allowing separate measurements of magnetisation and transport losses.

2. Re-design the Roebel cable to attain more turns and draw current near its rated value. This will improve the ampere turn performance metric against the benchmark.

3. Replace the copper coils with HTS coils which will allow the turn number to increase and boost the power rating of the machine and improve the accuracy.

4. A second rotor could be manufactured to increase the flux density and quality of the waveform. It is expected an operating flux density in a superconducting machine would be at least 3.5T compared with 0.5T achieved during this project.

5. The D.C. dyno can be replaced with a propeller to investigate the A.C. losses as a function of a simulated flight stage providing information on the maximum cryocooler capacity and also proving the reliability of superconducting machines by operating it for a long period of time.

References

[1] Magnet expert ltd ™. Accessed: 2018-04-07.

[2] Rectangular magnets. `https://tinyurl.com/8m28xqj`. Accessed: 2018-04-07.

[3] Universal joints (automobile). `https://tinyurl.com/8m28xqj`. Accessed: 2018-04-07.

[4] Mark D Ainslie, Weijia Yuan, and Tim J Flack. Numerical analysis of ac loss reduction in hts superconducting coils using magnetic materials to divert flux. *IEEE Transactions on Applied Superconductivity*, 23(3):4700104–4700104, 2013.

[5] Mark Douglas Ainslie, Di Hu, J Kvitkovic, J Kim, C Kim, S Pamidi, Difan Zhou, J Rush, and John Hay Durrell. Transport a.c. loss measurements of a triangular, epoxy-impregnated high temperature superconducting (hts) coil. Institute of Electrical and Electronics Engineers, 2017.

[6] John David Anderson Jr. *Fundamentals of aerodynamics*. Tata McGraw-Hill Education, 2010.

[7] SP Ashworth and M Suenaga. Measurement of ac losses in superconductors due to ac transport currents in applied ac magnetic fields. *Physica C: Superconductivity*, 313(3-4):175–187, 1999.

[8] Giulio Avanzini and Fabrizio Giulietti. Maximum range for -powered aircraft. *Journal of Aircraft*, 50(1):304–307, 2012.

[9] Rodney Alan Badcock, Nicholas J Long, Marc Mulholland, Sebastian Hellmann, Alan Wright, and Kent A Hamilton. Progress in the manufacture of long length ybco roebel cables. *IEEE Transactions on Applied Superconductivity*, 19(3):3244–3247, 2009.

[10] Bertrand Baudouy. Heat transfer and cooling techniques at low temperature. *arXiv preprint arXiv:1501.07153*, 2015.

[11] P Bauer, Y Bi, A Cheng, Y Cheng, A Devred, K Ding, X Huang, C Liu, X Lin, N Mitchell, et al. Test results of 52/68 ka trial hts current leads for iter. *IEEE Transactions on Applied Superconductivity*, 20(3):1718–1721, 2010.

[12] Charles P Bean. Magnetization of high-field superconductors. *Reviews of modern physics*, 36(1):31, 1964.

[13] Peter Philip Benham, Roy J Crawford, and Cecil G Armstrong. *Mechanics of engineering materials*. Longman Harlow, 1996.

[14] Frederick Berg, Joseph Palmer, Paul Miller, Mark Husband, and Graham Dodds. Hts electrical system for a distributed propulsion aircraft. *IEEE Transactions on Applied Superconductivity*, 25(3):1–5, 2015.

[15] Charles W Bert. Range and endurance of turboprop, turbofan, or piston–propeller aircraft having wings with or without camber. *Aircraft Design*, 2(4):183–190, 1999.

[16] Nicholas K Borer, Craig L Nickol, Frank Jones, Richard Yasky, Kurt Woodham, Jared Fell, Bradon Litherland, Patricia Loyselle, Andrew Provenza, Lee Kohlman, et al. Overcoming the adoption barrier to electric flight. *54th AIAA Aerospace Sciences Meeting*, page 1022, 2016.

[17] Cheryl L Bowman. Visions of the future: Hybrid electric aircraft propulsion. 2016.

[18] Marty K Bradley and Christopher K Droney. Subsonic ultra green aircraft research. 2011.

[19] Marty K Bradley and Christopher K Droney. Subsonic ultra green aircraft research: Phase 2. volume 2; hybrid electric design exploration. 2015.

[20] Gerald Brown. Weights and efficiencies of electric components of a turboelectric aircraft propulsion system. In *49th AIAA aerospace sciences meeting including the new horizons forum and aerospace exposition*, page 225, 2011.

[21] Gerald V Brown. Efficient flight-weight electric systems. 2012.

[22] Chris W Bumby, Rodney A Badcock, Hae-Jin Sung, Kwang-Min Kim, Zhenan Jiang, Andres E Pantoja, Patrick Bernardo, Minwon Park, and Robert G Buckley. Development of a brushless hts exc for a 10 kw hts synchronous generator. *Superconductor Science and Technology*, 29(2):024008, 2016.

[23] Eduardo Carrasco and Ulrich Schroeder. Rotor assembly with permanent magnets and method of manufacture, April 11 2017. US Patent 9,621,000.

[24] Ho-Myung Chang and Steven W Van Sciver. Thermodynamic optimization of conduction-cooled hts current leads. *Cryogenics*, 38(7):729–736, 1998.

[25] Bascom S Deaver Jr and William M Fairbank. Experimental evidence for quantized flux in superconducting cylinders. *Physical Review Letters*, 7(2):43, 1961.

[26] Ruben DelRosario. A future with hybrid electric propulsion systems: A nasa perspective. 2014.

[27] Jack Ekin. *Experimental techniques for low-temperature measurements: cryostat design, material properties and superconductor critical-current testing*. Oxford university press, 2006.

[28] M Feddersen, KS Haran, and F Berg. Ac loss analysis of mgb2-based fully superconducting machines. In *IOP Conference Series: Materials Science and Engineering*, volume 279, page 012026. IOP Publishing, 2017.

[29] James Felder, Hyun Kim, and Gerald Brown. Turboelectric distributed propulsion engine cycle analysis for hybrid-wing-body aircraft. In *47th AIAA aerospace sciences meeting including the new horizons forum and aerospace exposition*, page 1132, 2009.

[30] Steven Fletcher, Marie-Claire Flynn, Catherine E Jones, and Patrick J Norman. Hybrid electric aircraft: State of the art and key electrical system challenges. *The Transportation Electrification eNewsletter*, 2016(Sept), 2016.

[31] Kristian Fossheim and Asle Sudbø. *Superconductivity: physics and applications*. John Wiley & Sons, 2005.

[32] Jörg Franke, Benjamin Hofmann, Jan Tremel, and Alexander Meyer. Innovative methods for automated assembly and fixation of permanent magnets in electrical machines. *Procedia CIRP*, 26:724–728, 2015.

[33] Rene Fuger, Arkadiy Matsekh, John Kells, DBT Sercombe, and Ante Guina. A superconducting homopolar motor and generator—new approaches. *Superconductor Science and Technology*, 29(3):034001, 2016.

[34] Satoshi Fukui, Shogo Tsukamoto, Kazuki Nohara, Jun Ogawa, Takao Sato, and Taketsune Nakamura. Study on a.c. loss reduction in hts coil for armature winding of a.c. rotating machines. *IEEE Transactions on Applied Superconductivity*, 26(4):1–5, 2016.

[35] Bruce Gamble, Greg Snitchler, and Tim MacDonald. Full power test of a 36.5 MW hts propulsion motor. *IEEE Transactions on Applied Superconductivity*, 21(3):1083–1088, 2011.

[36] Jacek F Gieras, Rong-Jie Wang, and Maarten J Kamper. *Axial flux permanent magnet brushless machines*. Springer Science & Business Media, 2008.

[37] Neil Glasson, Michael Staines, Nathan Allpress, Mohinder Pannu, Julien Tanchon, Enric Pardo, Rodney Badcock, and Robert Buckley. Test results and conclusions from a 1 MVA superconducting transformer featuring 2g hts roebel cable. *IEEE Trans. Appl. Supercond*, 27(4), 2017.

[38] Neil D Glasson, Mike P Staines, Zhenan Jiang, and Nathan S Allpress. Verification testing for a 1 MVA 3-phase demonstration transformer using 2g-hts roebel cable. *IEEE Transactions on Applied Superconductivity*, 23(3):5500206–5500206, 2013.

[39] Amir S Gohardani, Georgios Doulgeris, and Riti Singh. Challenges of future aircraft propulsion: A review of distributed propulsion technology and its potential application for the all electric commercial aircraft. *Progress in Aerospace Sciences*, 47(5):369–391, 2011.

[40] Wilfried Goldacker, Francesco Grilli, Enric Pardo, Anna Kario, Sonja I Schlachter, and Michal Vojenčiak. Roebel cables from rebco coated conductors: A one-century-old concept for the superconductivity of the future. *Superconductor Science and Technology*, 27(9):093001, 2014.

[41] Francesco Grilli. Numerical modeling of hts applications. *IEEE Transactions on Applied Superconductivity*, 26(3):1–8, 2016.

[42] Francesco Grilli, Enric Pardo, Antti Stenvall, Doan N Nguyen, Weijia Yuan, and Fedor Gömöry. Computation of losses in hts under the action of varying magnetic fields and currents. *IEEE Transactions on Applied Superconductivity*, 24(1):78–110, 2014.

[43] Francesco Grilli, Michal Vojenčiak, Anna Kario, and Victor Zermeño. Hts roebel cables: Self-field critical current and ac losses under simultaneous application of transport current and magnetic field. *IEEE Transactions on Applied Superconductivity*, 26(4):1–5, 2016.

[44] Kiruba S Haran, Swarn Kalsi, Tabea Arndt, Haran Karmaker, Rod Badcock, Bob Buckley, Timothy Haugan, Mitsuru Izumi, David Loder, James W Bray, et al. High power density superconducting rotating machines—development status and technology roadmap. *Superconductor Science and Technology*, 30(12):123002, 2017.

[45] Kiruba S Haran, David Loder, Timothy O Deppen, and Lijun Zheng. Actively shielded high-field air-core superconducting machines. *IEEE Transactions on Applied Superconductivity*, 26(2):98–105, 2016.

[46] Di Hu, Mark D Ainslie, Jozef Kvitkovic, Jingeun Kim, Chul Kim, Sastry Pamidi, Difan Zhou, Jordan P Rush, and John H Durrell. Transport ac loss measurements of a triangular epoxy-impregnated high-temperature superconducting coil. *IEEE Transactions on Applied Superconductivity*, 27(4):1–6, 2017.

[47] Paul A Jackson, Kenneth Munson, and Lindsay Peacock. *Jane's All the World's Aircraft 2011-2012*. Jane's, 2011.

[48] Jianyi Jiang, Ashleigh Francis, Ryan Alicea, Maxime Matras, Fumitake Kametani, Ulf P Trociewitz, Eric E Hellstrom, and David C Larbalestier. Effects of filament size on critical current density in overpressure processed bi-2212 round wire. *IEEE Transactions on Applied Superconductivity*, 27(4):1–4, 2017.

[49] Z Jiang, KP Thakur, NJ Long, RA Badcock, and M Staines. Comparison of transport ac losses in an eight-strand ybco roebel cable and a four-tape ybco stack. *Physica C: Superconductivity and its applications*, 471(21-22):999–1002, 2011.

[50] Zhenan Jiang, Takashi Komeda, Naoyuki Amemiya, NJ Long, Mike Staines, RA Badcock, C Bumby, and RG Buckley. Total ac loss measurements in a six strand roebel cable carrying an ac current in an ac magnetic field. *Superconductor Science and Technology*, 26(3):035014, 2013.

[51] Zhenan Jiang, Mike Staines, Rod A Badcock, NJ Long, and Naoyuki Amemiya. Transport ac loss measurement of a five strand ybco roebel cable. *Superconductor Science and Technology*, 22(9):095002, 2009.

[52] Zou Jibin and Lu Yongping. Numerical calculations for ferrofluid seals. *IEEE transactions on magnetics*, 28(6):3367–3371, 1992.

[53] Tao Jin, Jian-ping Hong, Hao Zheng, Ke Tang, and Zhi-hua Gan. Measurement of boiling heat transfer coefficient in liquid nitrogen bath by inverse heat conduction method. *Journal of Zhejiang University-SCIENCE A*, 10(5):691–696, 2009.

[54] SW Kim, MH Sohn, SK Baik, YS Jo, MG Seo, EY Lee, RK Ko, and YK Kwon. Soldered double pancake winding of high temperature superconducting tape. *IEEE transactions on applied superconductivity*, 13(2):1784–1787, 2003.

[55] P Kittel. Cryocooler performance estimator. *Cryocoolers*, 14:777–780, 2007.

[56] Martin Knudsen. The kinetic theory of gases: some modern aspects. 1950.

[57] Shin-ichi Kobayashi. Development and manufacture of bi-2223 wires. In *Research, Fabrication and Applications of Bi-2223 HTS Wires*, pages 137–150. World Scientific, 2016.

[58] LK Kovalev, KV Ilushin, VT Penkin, KL Kovalev, S MA Koneev, VN Poltavets, AE Larionoff, KA Modestov, SA Larionoff, W Gawalek, et al. Hysteresis and reluctance electric machines with bulk hts elements. recent results and future development. *Superconductor Science and Technology*, 13(5):498, 2000.

[59] Karl Jerome Lamb. Permanent magnet coupling and transmission, September 16 1997. US Patent 5,668,424.

[60] David Larbalestier, Alex Gurevich, D Matthew Feldmann, and Anatoly Polyanskii. High-t c superconducting materials for electric power applications. *Nature*, 414(6861):368, 2001.

[61] David Larbalestier, Alex Gurevich, D Matthew Feldmann, and Anatoly Polyanskii. High-tc superconducting materials for electric power applications. In *Materials For Sustainable Energy: A Collection of Peer-Reviewed Research and Review Articles from Nature Publishing Group*, pages 311–320. World Scientific, 2011.

[62] JK Lee, SH Park, Y Kim, S Lee, HG Joo, WS Kim, K Choi, and SY Hahn. Test results of a 5 kw fully superconducting homopolar motor. *Progress in Superconductivity and Cryogenics*, 15(1):35–39, 2013.

[63] Dong Liu, Henk Polinder, Niklas Magnusson, Joost Schellevis, and Asger B Abrahamsen. Ripple field ac losses in 10-MW wind turbine generators with a mgb 2 superconducting field winding. *IEEE Transactions on Applied Superconductivity*, 26(3):1–5, 2016.

[64] Periklis Lolis. Development of a preliminary weight estimation method for advanced turbofan engines. 2014.

[65] NJ Long, RA Badcock, K Hamilton, A Wright, Z Jiang, and LS Lakshmi. Development of ybco roebel cables for high current transport and low ac loss applications. In *Journal of Physics: Conference Series*, volume 234, page 022021. IOP Publishing, 2010.

[66] Cesar A Luongo, Philippe J Masson, Taewoo Nam, Dimitri Mavris, Hyun D Kim, Gerald V Brown, Mark Waters, and David Hall. Next generation more-electric aircraft: a potential application for hts superconductors. *IEEE Transactions on Applied Superconductivity*, 19(3):1055–1068, 2009.

[67] Nateri Madavan, J Heidmann, C Bowman, P Kascak, A Jankovsky, and R Jansen. A nasa perspective on electric propulsion technologies for commercial aviation. *Proceedings of the Workshop on Technology Roadmap for Large Electric Machines, Urbana-Champaign, IL, USA*, pages 5–6, 2016.

[68] Brian G Marchionini, Yutaka Yamada, Luciano Martini, and Hiroyuki Ohsaki. High-temperature superconductivity: A roadmap for electric power sector applications, 2015–2030. *IEEE Transactions on Applied Superconductivity*, 27(4):1–7, 2017.

[69] M Miki, S Tokura, H Hayakawa, H Inami, M Kitano, H Matsuzaki, Y Kimura, I Ohtani, E Morita, H Ogata, et al. Development of a synchronous motor with gd–ba–cu–o bulk superconductors as pole-field magnets for propulsion system. *Superconductor Science and Technology*, 19(7):S494, 2006.

[70] T Nakamura, Y Yamada, H Nishio, K Kajikawa, M Sugano, N Amemiya, T Wakuda, M Takahashi, and M Okada. Development and fundamental study on a superconducting induction/synchronous motor incorporated with mgb2 cage windings. *Superconductor Science and Technology*, 25(1):014004, 2011.

[71] Denis Netter, Jean Lévêque, Bruno Douine, Philippe J Masson, Abderrezak Rezzoug, et al. Design and testing of a superconducting rotating machine. *IEEE transactions on applied superconductivity*, 17(1):27–33, 2007.

[72] W Nick, G Nerowski, H-W Neumüller, M Frank, P Van Hasselt, J Frauenhofer, and F Steinmeyer. 380 kw synchronous machine with hts rotor windings—-development at siemens and first test results. *Physica C: Superconductivity*, 372:1506–1512, 2002.

[73] Mihaela Niţă and Dieter Scholz. *Estimating the oswald factor from basic aircraft geometrical parameters*. Deutsche Gesellschaft für Luft-und Raumfahrt-Lilienthal-Oberth eV, 2012.

[74] WT Norris. Calculation of hysteresis losses in hard superconductors carrying ac: isolated conductors and edges of thin sheets. *Journal of Physics D: Applied Physics*, 3(4):489, 1970.

[75] M. P. Oomen. *A.C. loss in superconducting tapes and cables*. PhD thesis, UNIVERSITEIT TWENTE (THE NETHERLANDS, 2000.

[76] Neiss Oskar. Permanent magnetic couplings, October 23 1956. US Patent 2,768,316.

[77] B Oswald, KJ Best, M Setzer, M Söll, W Gawalek, A Gutt, L Kovalev, G Krabbes, L Fisher, and HC Freyhardt. Reluctance motors with bulk hts material. *Superconductor Science and Technology*, 18(2):S24, 2004.

[78] Asko Parviainen et al. Design of axial-flux permanent-magnet low-speed machines and performance comparison between radial-flux and axial-flux machines. *Acta Universitatis Lappeenrantaensis*, 2005.

[79] Charles P Poole and Horacio A Farach. *Superconductivity*. Wiley Online Library, 2007.

[80] Margaret P Proctor, James F Walker, H Douglas Perkins, Joan F Hoopes, and G Scott Williamson. Brush seals for cryogenic applications: performance, stage effects, and preliminary wear results in ln2 and lh2. 1996.

[81] Timing Qu, Yufan Li, Peng Song, Changhong Hao, Qihong Wu, Chen Gu, Jiamin Zhu, and Zhenghe Han. Design study of a 10-kw fully superconducting synchronous generator. *IEEE Transactions on Applied Superconductivity*, 28(4):1–5, 2018.

[82] Loïc Quéval, Víctor MR Zermeño, and Francesco Grilli. Numerical models for ac loss calculation in large-scale applications of hts coated conductors. *Superconductor Science and Technology*, 29(2):024007, 2016.

[83] JJ Rabbers, DC Van der Laan, Bernard ten Haken, and Herman HJ ten Kate. Magnetisation and transport current loss of a bscco/ag tape in an external ac magnetic field carrying an ac transport current. *IEEE transactions on applied superconductivity*, 9(2):1185–1188, 1999.

[84] Daniel P Raymer. Aircraft design: A conceptual approach (aiaa education). 2006.

[85] J Reinert, A Brockmeyer, and RW De Doncker. Calculation of losses in ferro-and ferrimagnetic materials based on the modified steinmetz equation. In *Industry Applications Conference, 1999. Thirty-Fourth IAS Annual Meeting. Conference Record of the 1999 IEEE*, volume 3, pages 2087–2092. IEEE, 1999.

[86] Jan Roskam. *Airplane Design: Preliminary sizing of airplanes*. DARcorporation, 1985.

[87] Naomi Rovnick. Easyjet to help develop a battery powered plane, Sep 2017.

[88] J Schellevis. Ac loss modeling of superconducting field windings for a 10MW wind turbine generator-an analytical and numerical analysis. 2014.

[89] Venkat Selvamanickam. Strategies to reach 2g hts wire price of 50/ka-m without high volume production. In *Proc. Int. Workshop Coated Conductors Appl.*, 2008.

[90] Carmine Senatore, Christian Barth, Marco Bonura, Miloslav Kulich, and Giorgio Mondonico. Field and temperature scaling of the critical current density in commercial rebco coated conductors. *Superconductor Science and Technology*, 29(1):014002, 2015.

[91] Xin Shen, He Liu, Xin-Bing Cheng, Chong Yan, and Jia-Qi Huang. Beyond lithium ion batteries: Higher energy density battery systems based on lithium metal anodes. *Energy Storage Materials*, 2017.

[92] Richard S Shevell. Fundamentals of flight, 1989. *Pretince-Hall Inc., Englewood Cliffs, NJ*, 7632.

[93] Jungwook Sim, Myungjin Park, Hyoungwoo Lim, Gueesoo Cha, Junkeun Ji, and Jikwang Lee. Test of an induction motor with hts wire at end ring and bars. *IEEE transactions on applied superconductivity*, 13(2):2231–2234, 2003.

[94] Marco M Sisto, Sonia M García-Blanco, Loic Le Noc, Bruno Tremblay, Yan Desroches, Jean-Sol Caron, Francis Provencal, and Francis Picard. Pressure sensing in vacuum hermetic micropackaging for moems-mems. *Journal of Micro/Nanolithography, MEMS, and MOEMS*, 9(4):041109, 2010.

[95] JL Smith, JL Kirtley, Sankar Sunder, and Steve Umans. Performance of MIT 10MVA superconducting generator rotor. *IEEE Transactions on Applied Superconductivity*, 5(2):445–448, 1995.

[96] MH Sohn, SK Baik, YS Jo, EY Lee, WS Kwon, YK Kwon, TS Moon, YC Kim, CH Cho, and I Muta. Performance of high temperature superconducting field coils for a 100 hp motor. *IEEE Transactions on applied superconductivity*, 14(2):912–915, 2004.

[97] MP Staines, Z Jiang, N Glasson, RG Buckley, and M Pannu. High-temperature superconducting (hts) transformers for power grid applications. In *Superconductors in the Power Grid*, pages 367–397. Elsevier, 2015.

[98] Hidehiko Sugimoto, Teppei Tsuda, Takaya Morishita, Yoshinori Hondou, Toshio Takeda, Hiroyuki Togawa, Tomoya Oota, Kazuya Ohmatsu, and Shigeru Yoshida. Development of an axial flux type pm synchronous motor with the liquid nitrogen cooled hts armature windings. *IEEE Transactions on Applied Superconductivity*, 17(2):1637–1640, 2007.

[99] Hai Sui, Heiko Pohl, Uwe Schomburg, Gerd Upper, and Steffen Heine. Wear and friction of ptfe seals. *Wear*, 224(2):175–182, 1999.

[100] JN Sweet, EP Roth, and M Moss. Thermal conductivity of inconel 718 and 304 stainless steel. *International journal of thermophysics*, 8(5):593–606, 1987.

[101] Marcin Szczech and Wojciech Horak. Tightness testing of rotary ferromagnetic fluid seal working in water environment. *Industrial Lubrication and Tribology*, 67(5):455–459, 2015.

[102] K Tamura, M Iwakuma, T Ueno, K Yun, S Sato, K Yoshida, A Tomioka, M Konno, and T Izumi. Study on the optimum arrangement of the field winding for a 20-kw fully superconducting motor. *IEEE Transactions on Applied Superconductivity*, 26(4):1–5, 2016.

[103] Xingguo Tan, Qingmin Li, and Hui Wang. Advances and trends of energy storage technology in microgrid. *International Journal of Electrical Power & Energy Systems*, 44(1):179–191, 2013.

[104] J Tanchon, N Maurel, T Charignon, T Trollier, A Ravex, Y Allemand, M Hervieu, and R Messing. Development of a vacuum compatible rotary dynamic seal for cryogenic liquids. In *AIP Conference Proceedings*, volume 1573, pages 1467–1474. AIP, 2014.

[105] Yorick Teeuwen. Propeller design for conceptual turboprop aircraft. 2017.

[106] P Tixador, Y Brunet, P Vedrine, Y Laumond, and JL Sabrie. Electrical tests on a fully superconducting synchronous machine. *IEEE Transactions on Magnetics*, 27(2):2256–2259, 1991.

[107] P Tixador, F Simon, H Daffix, and M Deleglise. 150-kw experimental superconducting permanent-magnet motor. *IEEE transactions on applied superconductivity*, 9(2):1205–1208, 1999.

[108] Egbert Torenbeek. *Synthesis of subsonic airplane design: an introduction to the preliminary design of subsonic general aviation and transport aircraft, with emphasis on layout, aerodynamic design, propulsion and performance*. Springer Science & Business Media, 2013.

[109] Lance W Traub. Range and endurance estimates for battery-powered aircraft. *Journal of Aircraft*, 48(2):703–707, 2011.

[110] O Tsukamoto, N Amemiya, K Yamagishi, T Takao, S Akita, S Torii, K Ohishi, and H Shimizu. Development and electrical test of a 30 kva class fully superconducting generator. *IEEE transactions on magnetics*, 30(4):2308–2311, 1994.

[111] Sarah Catherine Walpole, David Prieto-Merino, Phil Edwards, John Cleland, Gretchen Stevens, and Ian Roberts. The weight of nations: an estimation of adult human biomass. *BMC public health*, 12(1):439, 2012.

[112] Donald J Waltman and MJ Superczynski. High-temperature superconducting magnet motor demonstration. *IEEE transactions on applied superconductivity*, 5(4):3532–3535, 1995.

[113] Yinshun Wang, Xiaojin Guan, and Jingshu Dai. Review of ac loss measuring methods for hts tape and unit. *IEEE Transactions on Applied Superconductivity*, 24(5):1–6, 2014.

[114] JG Weisend. Principles of cryostat design. In *Cryostat Design*, pages 1–45. Springer, 2016.

[115] FN Werfel, U Floegel-Delor, R Rothfeld, T Riedel, B Goebel, D Wippich, and P Schirrmeister. Superconductor bearings, flywheels and transportation. *Superconductor Science and Technology*, 25(1):014007, 2011.

[116] SL Wipf. Ac losses in superconductors. *Journal of Applied Physics*, 39(6):2538–2538, 1968.

[117] Kiyoshi Yamaguchi, Miyoshi Takahashi, Ryoichi Shiobara, Tsukasa Taniguchi, Hiroshi Tomeoku, Masaki Sato, Hiroyuki Sato, Yutaka Chida, Masahiro Ogihara, Ryuukichi Takahashi, et al. 70 MW class superconducting generator test. *IEEE transactions on applied superconductivity*, 9(2):1209–1212, 1999.

[118] Yifeng Yang, Jorge Pelegrin, Edward A Young, Rainer Nast, Anna Kario, and Wilfried Goldacker. Ac losses of roebel cables with striated 2g rebco strands. *IEEE Transactions on Applied Superconductivity*, 28(4):1–5, 2018.

[119] Burt Zhang, David Driscoll, and Viatchestav Dombrovski. Construction and testing of a 1000 hp high-temperature superconducting motor. In *Petroleum and Chemical Industry Conference, 2002. Industry Applications Society 49th Annual*, pages 223–228. IEEE, 2002.

[120] Min Zhang, M Chudy, Wei Wang, Yiran Chen, Zhen Huang, Zhaoyang Zhong, Weijia Yuan, J Kvitkovic, SV Pamidi, and TA Coombs. A.c. loss estimation of hts armature windings for electric machines. *IEEE Transactions on Applied Superconductivity*, 23(3):5900604–5900604, 2013.

[121] Min Zhang, Fred Eastham, and Weijia Yuan. Design and modeling of 2g hts armature winding for electric aircraft propulsion applications. *IEEE Transactions on Applied Superconductivity*, 26(3):1–5, 2016.

[122] Min Zhang, Jae-Ho Kim, Sastry Pamidi, Michal Chudy, Weijia Yuan, and TA Coombs. Study of second generation, high-temperature superconducting coils: Determination of critical current. *Journal of Applied Physics*, 111(8):083902, 2012.

[123] Min Zhang, W Wang, Z Huang, M Baghdadi, W Yuan, J Kvitkovic, S Pamidi, and TA Coombs. Ac loss measurements for 2g hts racetrack coils with heat-shrink tube insulation. *IEEE Transactions on Applied Superconductivity*, 24(3):1–4, 2014.

[124] Min Zhang, Weijia Yuan, Jozef Kvitkovic, and Sastry Pamidi. Total a.c. loss study of 2g hts coils for fully hts machine applications. *Superconductor Science and Technology*, 28(11):115011, 2015.

[125] Wei Zhou, Zhenan Jiang, Mike Staines, Wenjuan Song, Chris W Bumby, Rodney A Badcock, Nicholas J Long, and Jin Fang. Magnetization loss in rebco roebel cables with varying strand numbers. *IEEE Transactions on Applied Superconductivity*, 28(3):1–5, 2018.

[126] Yong Zhou, Hao Su, Yijun Dai, Wei Chen, and Feng Xie. Design and research of torque tube used in hts motor. *Wuhan University Journal of Natural Sciences*, 19(4):350–354, 2014.

[127] Jiahui Zhu, Zhenyu Zhang, Huiming Zhang, Min Zhang, Ming Qiu, and Weijia Yuan. Electric measurement of the critical current, ac loss, and current distribution of a prototype hts cable. *IEEE Transactions on Applied Superconductivity*, 24(3):1–4, 2014.